Finite-size and Surface Effects in Iron Platinum Nanograins for Applications in Heat-Assisted Magnetic Recording Media

Binh Thanh Nguyen

Supervisor: Roy W. Chantrell
Richard F. L. Evans

Doctor of Philosophy

University of York
Physics

March 2022

Abstract

Heat-Assisted Magnetic Recording (HAMR) has emerged as a promising next-generation approach for magnetic recording. The functioning of HAMR requires the recording media to be made of magnetic materials with high anisotropy and suitable Curie temperature. Iron Platinum in the $L1_0$-phase ($L1_0$-FePt) has been found to satisfy these two requirements, thus having been attracting extensive attention and investigation. This Thesis presents a coherent and comprehensive computational research on the impacts of finite-size and surface effects in $L1_0$-FePt for potential HAMR applications. Simulations are performed by VAMPIRE an atomistic simulation code developed in the University of York and several key findings have been obtained. First, the existence of a size threshold at 3.5 nm is discovered below which finite-size effects are found to permeate into the centre of the $L1_0$-FePt grains leading to the well-known Curie temperature dispersion of the recording medium. A correlation between the Curie temperature dispersion and surface disorder is formulated which can be extended beyond $L1_0$-FePt to be applicable to different crystal structures. Second, a novel fourth-order anisotropy component is found in a phase-coupled core-shell structured $L1_0/A1$-FePt grain which exhibits strong size and geometry-dependence unseen in previous literature. Additionally, the scaling to magnetisation of this fourth-order anisotropy is found to disobey the classical Callen-Callen power law. These properties can be successfully explained by an analytic model which demonstrates the origin of this novel fourth-order anisotropy to be from the canting of the core and shell magnetisation. The applicability of this analytic model, also, is shown to extend to be valid in a generic soft-hard coupled nanocomposite magnetic system. Finally, the switching efficiency of this phase-coupled core-shell structured $L1_0/A1$-FePt grain is investigated. Available data demonstrate the existence of a non-negligible switching error rate in all tested grain configurations. Reducing the grain size and using shorter write pulses are found to induce higher switching error rate. However, it is shown that these detriments can be mitigated by surface engineering. Overall, the studies presented in this Thesis have addressed and provided many helpful insights into outstanding challenges on the path toward the realisation of $L1_0$-FePt in HAMR recording media.

Table of contents

List of tables ix

List of figures xi

1 Introduction to magnetic recording and heat-assisted magnetic recording 1
- 1.1 Magnetic recording and the trilemma . . . 1
- 1.2 Heat-assisted magnetic recording and the quadrilemma . . . 4
- 1.3 Thesis outline . . . 7

2 Methodology and theories of magnetic modelling 9
- 2.1 Fundamental concepts of an atomistic model . . . 9
  - 2.1.1 The exchange energy . . . 9
  - 2.1.2 The magnetocrystalline anisotropy . . . 13
  - 2.1.3 The energy of an externally applied field . . . 15
  - 2.1.4 The stochastic Landau-Lifshitz-Gilbert equation . . . 15
- 2.2 A review of magnetic modelling frameworks . . . 17
  - 2.2.1 Micromagnetics . . . 18
  - 2.2.2 Ab-initio and atomistic Spin models . . . 21
- 2.3 The VAMPIRE atomistic simulation software package . . . 22
  - 2.3.1 The Monte-Carlo and constrained Monte-Carlo methods . . . 23
  - 2.3.2 The temperature rescaling method . . . 24
  - 2.3.3 The atomistic Spin Hamiltonian . . . 26
- 2.4 The Mean-field theory . . . 28
- 2.5 The 2-ion anisotropy model for Iron Platinum FePt . . . 30
- 2.6 Summary . . . 32

3 The influence of finite-size effects on the Curie temperature of $L1_0$-FePt 33
- 3.1 Motivation . . . 33

3.2 Simulation methods and settings . . . 35
3.2.1 Theoretical background . . . 35
3.2.2 Construction of FePt grains . . . 37
3.2.3 Determining the Curie temperature . . . 38
3.2.4 Simulation parameters of FePt . . . 42
3.3 Results and discussion . . . 43
3.3.1 The Curie temperature variation with grain size . . . 43
3.3.2 The layer-resolved magnetisation profiles . . . 45
3.3.3 The cross-sectional magnetisation profiles . . . 48
3.3.4 The correlation between the magnetisation loss and the atomistic bond loss . . . 52
3.4 Further remarks . . . 54
3.5 Summary . . . 56

4 Higher-order magnetic anisotropy in soft-hard nanocomposite materials 57
4.1 Motivation . . . 57
4.2 Simulation methods and settings . . . 59
4.2.1 Construction of the FePt core-shell grains . . . 59
4.2.2 The truncated exchange interaction . . . 61
4.2.3 The truncated 2-ion anisotropy . . . 64
4.2.4 The Spin Hamiltonian . . . 65
4.2.5 The torque method . . . 65
4.3 Results and discussion . . . 67
4.3.1 Validating the scaling law of the second-order anisotropy . . . 67
4.3.2 The existence and magnitude of the fourth-order anisotropy . . . 69
4.3.3 The scaling law of the fourth-order anisotropy . . . 70
4.3.4 The temperature-dependent magnetisation . . . 71
4.4 An analytic model for the fourth-order anisotropy . . . 75
4.4.1 The derivation without an in-plane anisotropy . . . 75
4.4.2 Approximate introduction of the in-plane single-site anisotropy . . . 78
4.4.3 Analytic calculation of high-symmetry cases . . . 79
4.4.4 General geometry-independent formulation . . . 80
4.5 An analysis of simulation results of the FePt core-shell . . . 82
4.5.1 The canting between the core and the shell magnetisation . . . 82
4.5.2 Representation of the 2-ion anisotropy of FePt and calculation of the second-order anisotropy . . . 83
4.5.3 The fourth-order anisotropy and its behaviours . . . 84

4.6 Summary 87

5 HAMR switching efficiency in core-shell $L1_0$/A1-FePt grain 89
5.1 Motivation 90
5.2 Simulation methods and settings 92
5.2.1 Three configurations of FePt grains 92
5.2.2 Application of a laser pulse and an external magnetic field 93
5.2.3 Temperature rescaling 96
5.2.4 The Spin Hamiltonian 97
5.2.5 Other parameters 99
5.3 Results and discussion 100
5.3.1 Effects of temperature-rescaling on switching behaviour 100
5.3.2 Effects of cooling time on switching behaviour 101
5.3.3 Effects of grain configurations on switching behaviour 105
5.3.4 Effects of grain configurations on the blocking temperature 105
5.4 Further remarks and summary 111

6 Conclusions and further works 113

Appendix A Simulation data tables 117
A.1 The grain size-dependent Curie temperature variation 117
A.2 The correlation between the Curie temperature drop and atomistic bond loss . 118
A.3 The core size-dependent magnitude of the fourth-order anisotropy 118

Appendix B Sampled VAMPIRE simulation files 121
B.1 Chapter 3 - Investigation of finite-size effects 121
B.1.1 Input 121
B.1.2 Material file 122
B.2 Chapter 4 - Investigation of the core-shell structure 124
B.2.1 Input 124
B.2.2 Material file 125
B.3 Chapter 5 - Investigation of the switching efficiency 127

References 129

List of tables

3.1 The nominal and exact grain sizes of simulated FePt grains 38
3.2 VAMPIRE MC parameters 42
3.3 Unit cell parameters for each simulated configuration of FePt. 43
3.4 FSSL fitting parameters for each simulated configuration of FePt. 45
3.5 Correlation fitting parameters for each simulated configuration of FePt. . . . 55

4.1 VAMPIRE parameters for the core-shell simulations. 66
4.2 Values of A/B and $(1-f)^2$ for various high-symmetry geometries. 80

5.1 The Curie temperature T_C of the $L1_0$-phase of each configuration of the simulated FePt grain. 97
5.2 VAMPIRE parameters for the switching efficiency investigation. 100

A.1 The Curie temperatures at each grain size for each simulated lattice structure. 117
A.2 The percentage bond loss and Curie temperature reduction for each simulated lattice. 118
A.3 The percentage magnitude of the fourth-order anisotropy constant in relative to the second-order anisotropy constant, K_2/K_1, for each core size R at $T = 10$ K. 119

List of figures

1.1 A comparison between the operating principle of the Longitudinal Recording Technique and the Perpencicular Rercording Technique . . . 2
1.2 The trilemma of magnetic recording . . . 3
1.3 The quadrilemma of magnetic recording . . . 5
1.4 ASTC/ASRC Technology Roadmap . . . 6
1.5 An illustration of (a) a typical design of HAMR head-media recording image and (b) HAMR operating principle . . . 6

2.1 Shape anisotropy in an elongated particle . . . 14
2.2 The dynamics of (a) undamped precession, (b) deterministic-LLG (strictly $T = 0$), and (c) stochastic-LLG ($T \geq 0$) . . . 17
2.3 Comparison of the finite-difference and finite-element method . . . 19
2.4 Temperature-rescaling of spins . . . 25
2.5 Temperature-dependent magnetisation for the elemental ferromagnets . . . 27

3.1 Crystal structures of FePt . . . 34
3.2 An illustration of the creation of an equivalent modified-sc pseudo-cell from the original fct primitive cell of $L1_0$-FePt. . . . 37
3.3 Sampled cross-sectional views of the 3 simulated lattice structures. . . . 38
3.4 A sample of the temperature-dependent distribution of the magnetisation and longitudinal susceptibility. . . . 40
3.5 The Monte-Carlo steps . . . 41
3.6 Determination of the exchange energy constant for simulated FePt grains with different lattice structures. . . . 43
3.7 The dependence of Curie temperature on grain size. . . . 45
3.8 The layer-resolved magnetisation profile of fcc lattice grain at 550 K. . . . 46
3.9 The layer-resolved magnetisation profile of modified-sc lattice grain at 550 K. 47
3.10 The layer-resolved magnetisation profile of bcc lattice grain at 550 K. . . . 47

3.11 Comparison between atomistic and semi-analytic mean field calculation of layer-resolved magnetisation at 550 K . . . 48
3.12 Evolution of the cross-sectional magnetisation profile for fcc lattice grains at 550 K . . . 49
3.13 Evolution of the cross-sectional magnetisation profile for modified-sc lattice grains at 550 K . . . 50
3.14 Evolution of the cross-sectional magnetisation profile for bcc lattice grains at 550 K . . . 51
3.15 Correlation between the Curie temperature drop and atomistic bond loss . . . 54
3.16 A sample of voronoi-structured grains. . . . 55

4.1 Pt surface segregation in experimental $L1_0$-FePt grains . . . 59
4.2 Visualisations of the FePt grains . . . 60
4.3 Cross-sectional view of the core-shell grains . . . 61
4.4 Visualisation of the Fe neighbours in $L1_0$-FePt up to the third-level of nearest-neighbour. . . . 62
4.5 Visualisation of the bulk $L1_0$ grain with a cubic shape of size 8nm. . . . 68
4.6 The scaling of second-order anisotropy constant K_1 against M in a bulk $L1_0$-system. . . . 68
4.7 Fitting to the torque τ for sampled core sizes (a) $R = 0.40$, (b) $R = 0.50$, and (c) R=0.70. . . . 69
4.8 The anisotropy K_2/K_1 ratio dependence on core size R. . . . 71
4.9 Sampled scaling of the fourth-order anisotropy constant K_2 to the magnetisation for core size $R = 0.70$ yields a scaling exponent $\beta \approx 2.1$. . . . 72
4.10 Variation of the scaling exponent β of the fourth-order anisotropy constant K_2 as a function of the core size R. . . . 72
4.11 The temperature-dependent magnetisation $M(T)$ for different core sizes R of (a) the entire grain, and (b) the $L1_0$-core only. . . . 73
4.12 The temperature-dependent magnetisation $M(T)$ of the entire core-shell grain and of each phase for core size (a) $R = 0.40$, (b) $R = 0.60$, and (c) $R = 0.80$. . 74
4.13 The canting of the core and shell magnetisation with both geometry-dependent and geometry-independent analytic fits shown. . . . 82
4.14 The variation of the second-order anisotropy constant K_1 per atom with the core size R. . . . 84
4.15 The variation of the fourth-order anisotropy constant K_2 per atom with the core size R. . . . 85
4.16 The variation of the K_2/K_1 ratio with the core size R. . . . 86

5.1 An illustration of the energy barrier. 90
5.2 The cross-sectional sketch of the three simulated configurations of FePt grain. 93
5.3 The Magnetisation $M(T)$ of each FePt-grain configuration. 94
5.4 A sampled temperature profile of a laser pulse of 1.0 ns cooling time and $T_{max} = 700$ K with Gaussian fit. 94
5.5 Examples of switching and non-switching after the application of a laser pulse of 0.5 ns cooling time. 96
5.6 The effect of temperature rescaling on the magnetisation curve of the three simulated configurations. 98
5.7 Switching probabilities of three FePt-grain configurations when the laser pulse is applied with cooling time $\tau = 0.2$ ns. 102
5.8 Switching probabilities of three FePt-grain configurations when the laser pulse is applied with cooling time $\tau = 0.5$ ns. 103
5.9 Switching probabilities of three FePt-grain configurations when the laser pulse is applied with cooling time $\tau = 1.0$ ns. 104
5.10 The impact of varying cooling time of the applied laser pulse in the $L1_0/A1-45/05$ grain configuration. 106
5.11 The impact of varying cooling time of the applied laser pulse in the $L1_0-45$ grain configuration. 107
5.12 The impact of varying cooling time of the applied laser pulse in the $L1_0-50$ grain configuration. 108
5.13 The effect of grain configurations on the switching probability for varying cooling time with temperature-rescaling. 109
5.14 The effect of grain configurations on the switching probability for varying cooling time without temperature-rescaling. 110

To my most loving parents and cheerful little sister at home, and to my second family in Wakefield, I dedicate this work.
To my dearest Kim Ngân, may this forever mark an unforgettable milestone in our journey together. A journey that shall last for a lifetime.

Acknowledgements

I would like to take this opportunity to express my gratitude and appreciation to my supervisors Roy Chantrell and Richard Evans without whose guidance and mentorship - both scientific and mental - as well as unwavering trust and support and encouragement this work would not have been possible. Thank you Roy for providing me with this studentship so that I can have a chance to pursue my childhood dream of becoming a physicist. I am ever grateful for your patience and kindness, for your wisdom and counsel be it about academic or financial matters. Thank you Richard for many incredible insights and timely advice which in so many occasions have shown me the way forward. The VAMPIRE code you have developed and cared for is simply amazing. Roy and Richard, beyond this PhD you are my model of not only a scientist but also a great teacher.

I am most thankful to Sergiu Ruta and his wife Mara Strungaru. I have lost count of how many times you two have helped me with my struggles and listened to my rants, have shared with me both joy and sorrow, have offered me inspiration and consolation, comfort and compassion, and so much more. You two are what always reminds me that I, despite being a thousand leagues away from home, have never been alone here.

A special thank I would like to extend to Sarah Jenkins and Ondrej Hovorka for the productive collaboration we have had - and may it continue to flourish for many years to come. Another special thank I would like to reserve for Andrew Higginbotham and Vlado Lazarov who acting as my TAP members have given me many helpful advice and suggestions.

I am also grateful to everyone else in the Computational Magnetism group at York whom I have had the privilege to meet and get acquainted of: Ewan, Sarah, Daniel, Andrew, Andrea, Razvan, Roberto, Sam, Luke, Jane, and so many more. You are all parts of my four-year PhD journey which, thank to you, has been so enjoyable and memorable.

Last but not least, I would like to acknowledge the provision of computer time on the VIKING high-performance research computing cluster at the University of York. The interests and feedback that I have received from the ASRC (Advanced Storage Research Consortium) meetings are also fully appreciated and acknowledged.

Declaration

I hereby declare that except where specific reference is made to the work of others, the contents of this Thesis are original and I am the sole author. This work has not been submitted in whole or in part for consideration for any other degree or qualification in this, or any other university. Atomistic spin dynamics simulations have been carried out by the VAMPIRE atomistic simulation software package developed by the Computational Magnetism group at the University of York via the VIKING high-performance research computing cluster of the University of York. The majority of this Thesis has been presented at various conferences by the author, some chapters being based on the following publications:

- Nguyen Thanh Binh, Sergiu Ruta, Ondrej Hovorka, Richard Evans, Roy Chantrell. "The Influence of Finite-size Effects on the Curie Temperature of $L1_0$-FePt", manuscript submitted to Physical Review B, under review (2022).
- Nguyen Thanh Binh, Sarah Jenkins, Sergiu Ruta, Richard Evans, Roy Chantrell. "Higher-order Magnetic Anisotropy in Soft-Hard Nanocomposite materials", manuscript in final revision, planned submission to Physical Review Letters.

1

Introduction to magnetic recording and heat-assisted magnetic recording

1.1 Magnetic recording and the trilemma

Magnetic recording refers to the process of writing and storing data on a magnetised medium made from the grains of magnetisable materials [1]. Durable storage of information requires the writing media to be made of suitable magnetic materials which exhibit at least two thermally well-defined states corresponding to the two binary "0" and "1" states of the information bit. A very ambitious target for the future is set that a bit of information will be stored on a single grain, but today several grains are required [2]. A qualified magnetic storage is expected to meet the three following standards. First, it ought to exhibit a large saturation magnetisation necessary for the production of clear signals in the read-head. Second, it ought to exhibit a suitable coercivity field which enables the writing of information via switching magnetic moments from one binary state to another. Finally, it ought to exhibit a high level of thermal stability which is required for a long-lasting preservation and extraction of the information stored on it for a duration of several years.

Historically, one of the first techniques of magnetic recording in Hard Disk Drive (HDD) was the Longitudinal Recording Technology (LRT) in which the writing media are magnetised horizontally to the write head and in parallel to the surface of the disk [1]. This recording technique confers many desirable qualities, such as satisfactory areal density, good signal-to-noise ratio (SNR) if high anisotropy is retained in the recording layers, and low thickness [3], but on the downside suffers from severe thermal instabilities found in the longitudinal writing media [4]. After many attempts at further improving the areal density, LRT was rendered obsolete by a new technique coined Perpendicular Recording Technology (PRT). The most notable difference between LRT and PRT, a comparison of which is shown in Fig. 1.1, is that

in PRT the written data bits on the writing medium are polarised perpendicular to the disk surface. This perpendicular alignment of the bits, in either parallel or anti-parallel orientation corresponding to the binary state "1" or "0" respectively, helps to minimise demagnetisation effects and stray fields thus allowing the achievement of higher areal density [5, 6]. The typical structure of a PRT recording medium consists of four layers: a soft-magnetic under-layer, a seed or intermediary layer, the recording layer, and a protection layer. First, the presence of a soft-magnetic under-layer mirrors the magnetic pole of the write-head and minimises interference effects of neighbouring grains, thus amplifying and confining the write field to a perpendicular direction to the thin film in a single-bit region [7]. The amplified write field, in turn, allows magnetic writing to be done on media with a large coercivity field by which it is now made possible to enhance areal density via decreasing grain size and increasing anisotropy without sacrificing thermal stability - the balance of these trio of factors is known as the magnetic recording trilemma which will be discussed in detail later. Next, the seed layer helps to decouple the soft-magnetic under-layer from the recording layer and to promote the growth of the recording layer with a perpendicular easy axis. Finally, the protection layer, as its name already implies, is added to protect the recording layer from mechanical damages [6–8]. Since its inception, PRT has largely replaced LRT and remained to be the dominant magnetic recording technique in use today.

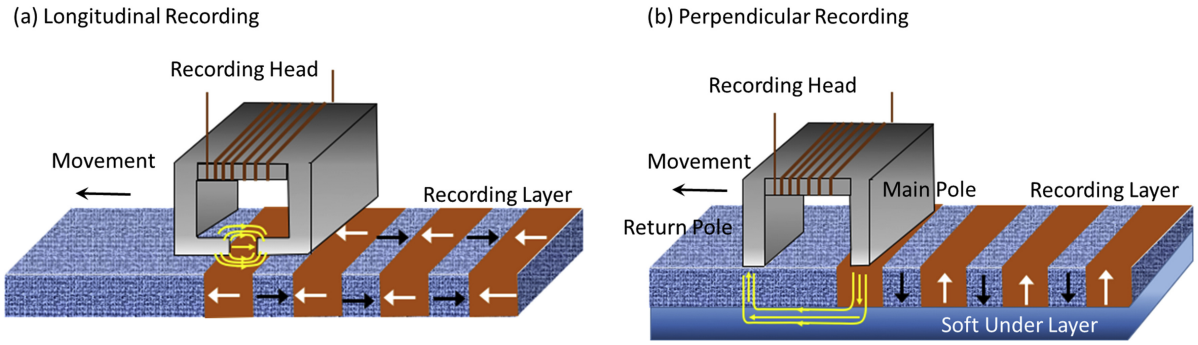

Fig. 1.1 A comparison between the operating principle of (a) the Longitudinal Recording Technique (LRT) and (b) the Perpencicular Rercording Technique (PRT): the written bits are aligned parallel to the media surface in LRT but perpendicular to the media surface in PRT. Source: excerpt from [9].

Magnetic recording functions on the balance between three main factors which form the well-known magnetic recording trilemma: the task of optimising the signal-to-noise (SNR) ratio, thermal stability, and writability [10]. The intertwined connections between these three factors are illustrated in Fig. 1.2. The ultimate design aim of magnetic recording is to improve areal density, and the first consideration is to achieve this target whilst maintaining sufficient Signal-to-Noise (SNR) ratio. In simple terms, in any recording medium there always exists a

portion of "defect" grains with anomalously large switching field higher than the maximum magnitude of the externally applied writing field. These "defect" grains will not be switched by the writing field, thus leading to switching errors. The SNR depends on the ratio for every single data bit between the "functioning" grains that can switch and contribute to information storage and the "defect" grains that do not switch and lead to errors. To achieve an acceptable SNR, it therefore requires to increase the number of grains per bit in order to improve this ratio. However increasing the number of grains per bit obviously decreases areal density, so an alternative has to be found.

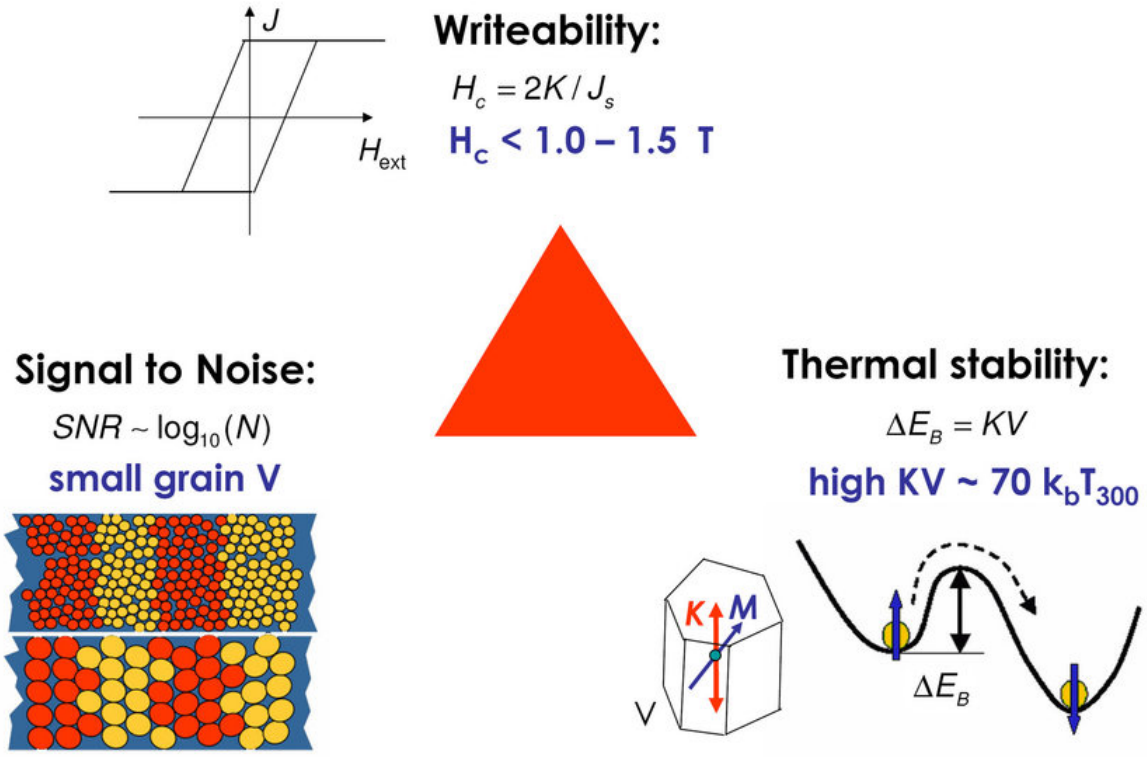

Fig. 1.2 The trilemma of magnetic recording: to improve areal density the grain volume V in the recording media has to be reduced in order to maintain a sufficient Signal-to-Noise ratio. With decreasing grain volume the energy barrier $\Delta E_B = KV$ is decreased, which can be compensated for by the use of a high coercive material with a large anisotropy constant K. However the write field is proportional to K which in turns limits the maximum usable high K value materials. Source: excerpt from [11].

If the number of grains per bit, for now, is found difficult to be reduced, the said alternative to improve areal density is to reduce the grain volume instead. However, reducing grain volume means loss of thermal stability because of a smaller energy barrier KV - with K the anisotropy density and V the volume. It has been shown that an energy barrier of $KV \approx 40 k_B T$ - where k_B is the Boltzmann constant and T the absolute temperature in Kelvin - is required for reliable

information storage for roughly 10 years at room temperature; and yet for practical applications, the minimum requirement has to be pushed to $KV \geq 60k_BT$ so as to leave some margin for external demagnetisation fields and other factors [2]. In order to maintain a sufficient energy barrier when using smaller-sized grains, therefore, it has to be compensated for by finding a recording layer material with high uniaxial anisotropy density K. However, using a high-anisotropy material for the recording medium produces yet another issue that a correspondingly high write field from the writing transducer would be required to switch the grain magnetisation since the write field is proportional to the anisotropy density K. Since the maximum achievable magnitude of write field is largely restricted by current technologies available, the usable high-anisotropy materials are also limited [1, 2, 10]. These considerations constitute the description of the magnetic recording trilemma which any new technological development of the magnetic recording has to take into account for a practical solution.

1.2 Heat-assisted magnetic recording and the quadrilemma

Beyond the previously discussed three factors that constitute the magnetic recording trilemma, a fourth factor has recently been discovered and has to be taken into consideration: a probability of back-switching of spins during the assisted-writing process due to thermally induced transitions. The process of magnetic recording is far from error-free: as the write transducer writes the information bit via switching the grain magnetisation, there is a chance that at any time the switching would fail due to many thermally-driven irregularities. Therefore, besides the original three factors, it is necessary to take into account the rate of switching error. This switching error rate is termed the Bit-Error-Rate (BER) [12] and can be generally understood as the probability of wrongly coding the information to the writing medium. Apparently, high BER would damage the integrity of stored information. In order to achieve an acceptable level of BER, the material saturation magnetisation - M_s - and the external magnetic field produced by the writing transducer - H_{wr} - must be maximised. Currently this acts as a source of DC noise, however in terms of ultra-high storage densities involving heated dot recording, this gives a potential limit of magnetic recording density [12]. The introduction of the BER therefore extends the original trilemma to a quadrilemma that provides a more complete account of considerations for magnetic recording. Overall, the quadrilemma emphasises the importance of thermal fluctuation for small-sized systems which are prone to high BER and thus require design optimisation for applications in the recording media technologies. An illustration of the magnetic recording quadrilemma is shown in Fig. 1.3.

In the quest of finding a solution to the magnetic recording quadrilemma, the Advanced Storage Technology Consortium (ASTC) - currently the Advanced Storage Research Consor-

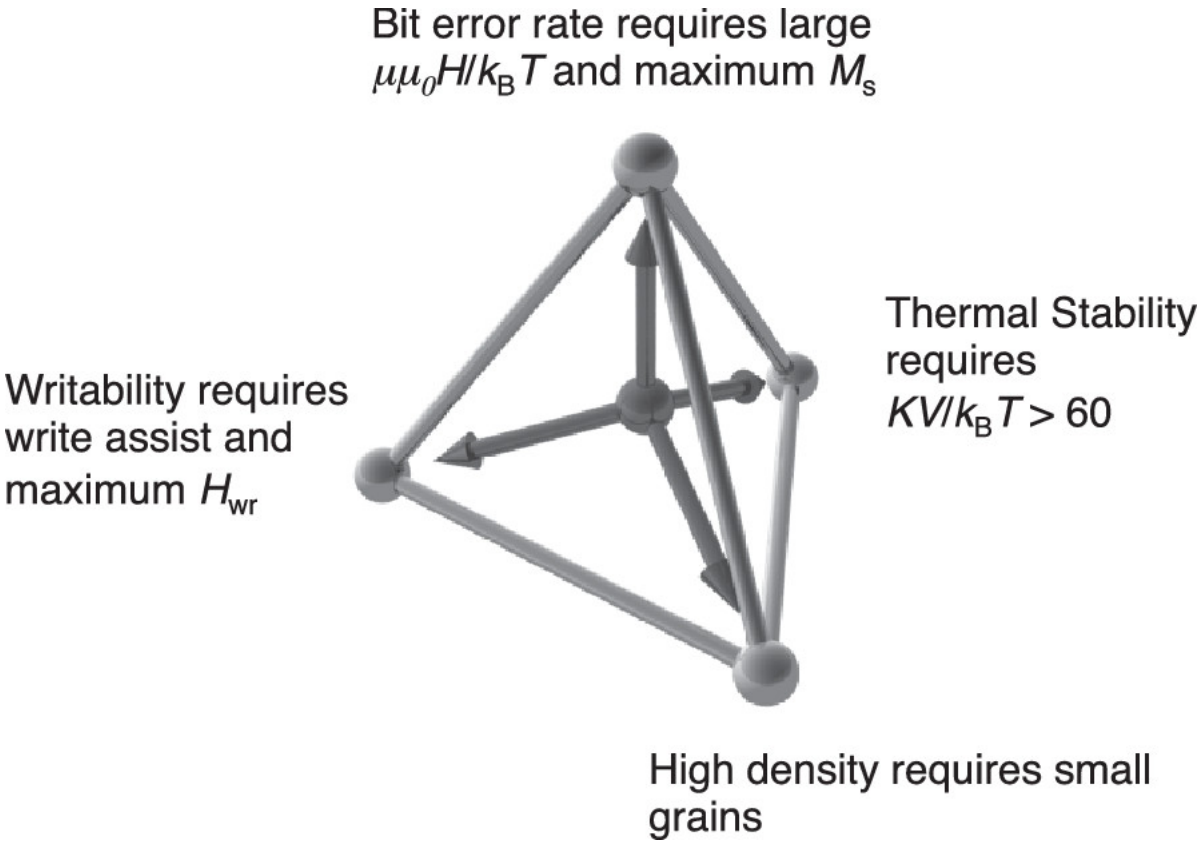

Fig. 1.3 The quadrilemma of magnetic recording: the use of grains with reduced volume requires an compensation in the form of increasing the anisotropy constant K to maintain thermal stability, and also maximising the saturation magnetisation M_s to ensure thermal writability. Source: excerpt from [12].

tium (ASRC) - Technology Roadmap displayed in Fig. 1.4 suggests two main approaches. The first approach is Bit-Patterned Recording (BPR) which aims for achieving ultra-high areal density by reducing the current number of grains required per data bit to as low as one [13]. The second approach is to address the writability issue via the addition of a write assist by which the switching field during the recording process can be reduced without forgoing thermal stability. The scope of this Thesis focuses on one particular form of write-assisted magnetic recording: the thermally-assisted or more commonly known as Heat-Assisted Magnetic Recording (HAMR) [14–16]. The HAMR write-head first applies an intense, highly localised heat spot for a very short time to a recording medium in order to heat it up to or beyond its Curie temperature (T_C), then writes the data inductively after which cooling to ambient temperature restores thermal stability. Since the recording process is performed near the Curie temperature of the writing medium where the anisotropy has been drastically reduced, a write field of magnitude much lower than what would otherwise be required can still switch the magnetisation

equally effectively. An illustration of a typical HAMR design and its operating principle is shown in Fig. 1.5. HAMR has been demonstrated to be able to achieve an areal density close to 1 Tb/in^2 [2, 17] with recent progresses aiming up to 1.402 Tb/in^2 [17] or even more ambitious 4 Tb/in^2 [14]. The theoretical limit of storage densities achievable in HAMR, because of the inevitability of switching error rate, has been suggested be capped at around 15 Tb/in^2 to 20 Tb/in^2 [12]. An ultimate solution which combines the write-assist method with BPR scheme has been envisioned to yield the ultimate densities [18, 19].

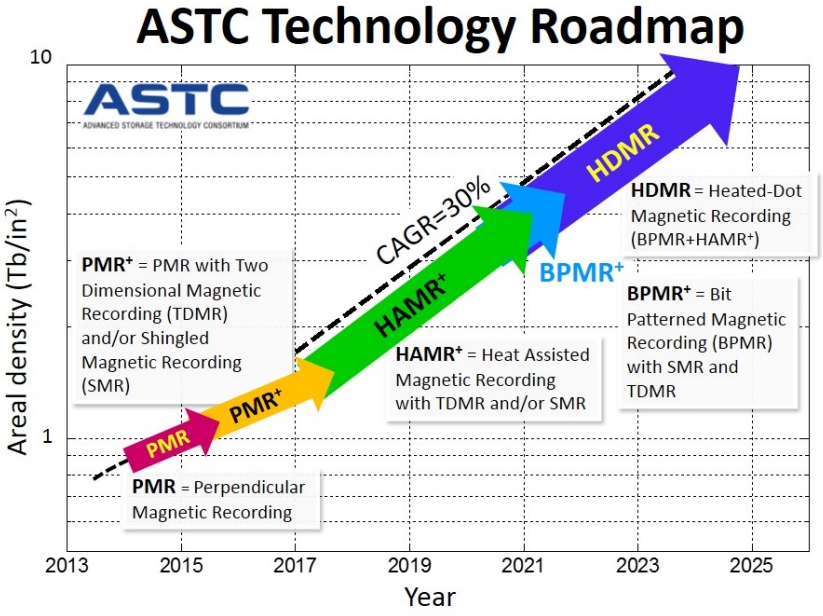

Fig. 1.4 ASTC/ASRC Technology Roadmap showing envisioned progression of storage densities in the near future. Source: excerpt from [20].

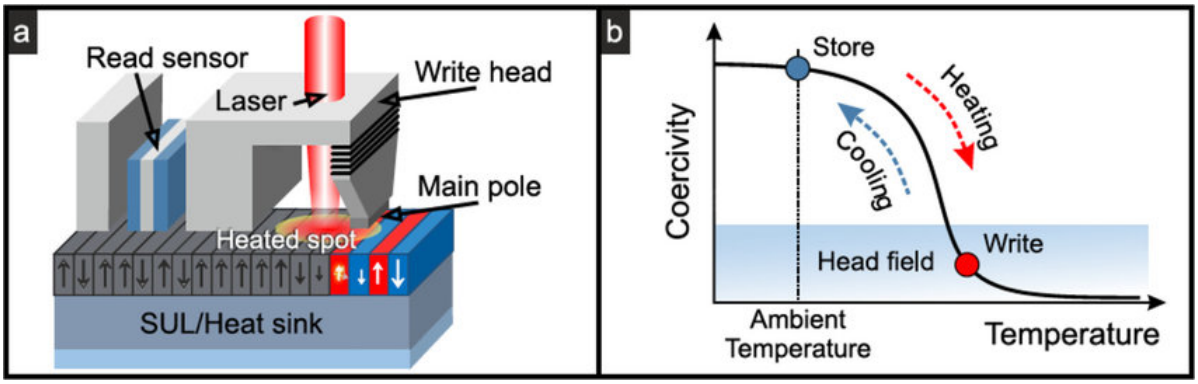

Fig. 1.5 An illustration of (a) a typical design of HAMR head-media recording image and (b) HAMR operating principle. Source: excerpt from [15].

1.3 Thesis outline

This Thesis is aimed to present a coherent and comprehensive research of finite-size and surface effects in Iron Platinum in the $L1_0$ phase ($L1_0$-FePt) for potential applications in Heat-assisted Magnetic Recording (HAMR). Each Chapter is intended not only to be built upon the previous but also to lay the foundation for the next, so as to convey a clear sense of progression in not only computational techniques but also scientific complexity. To achieve such purpose, the Thesis structure is designed to follow this outline.

Chapter 1 - Introduction to magnetic recording and heat-assisted magnetic recording has reviewed the context of Magnetic Recording and it well-known associating trilemma. Rapid developments in the field has culminated in the Heat-Assisted Magnetic Recording (HAMR) technique and consequently extended the trilemma to a quadrilemma.

Chapter 2 - Methodology and theories of magnetic modelling: This Chapter presents an overview of magnetic modelling frameworks of ubiquitous use today, with a focus on the atomistic modelling method which is implemented in this research via the VAMPIRE atomistic simulation code developed at the University of York. Additionally, the key concepts of the Mean-field theory and of the 2-ion anisotropy model of $L1_0$-FePt are also introduced.

Chapter 3 - The influence of finite-size effects on the Curie temperature of $L1_0$-FePt: This Chapter covers the first part of the $L1_0$-FePt study which explains why $L1_0$-FePt is a material highly suitable for HAMR, as well as presents the results of the investigation of the dependence of the Curie temperature dispersion of $L1_0$-FePt on finite-size and surface effects.

Chapter 4 - Higher-order magnetic anisotropy in soft-hard nanocomposite materials: This Chapter encapsulates the second part of the $L1_0$-FePt study which extends the established results in Chapter 3 to investigate the effects of surface faceting and interface interaction on the fourth-order anisotropy of $L1_0$-FePt in a novel phase-coupled core-shell structured grain which closely resembles a real HAMR grain. An analytic model is formulated to explain the results in this Chapter of which applicability is shown to extend beyond the studied core-shell $L1_0$-FePt structure to any generic soft-hard nanocomposite material.

Chapter 5 - HAMR switching efficiency in core-shell $L1_0$/A1-FePt grain: This Chapter presents the last part of the $L1_0$-FePt study in which the established findings of the previous Chapter 3 and 4 are put in use and combined into an investigation of the switching efficiency of the core-shell structured $L1_0$-FePt grain in a HAMR write process.

Chapter 6 - Conclusions and further works: The Thesis will then conclude with a summary which recaptures the key findings of the research and their relevance to the field of study. Further remarks will also be made on potential future directions for a continued development of the research.

2

Methodology and theories of magnetic modelling

2.1 Fundamental concepts of an atomistic model

In this Section, the fundamental concepts of the atomistic modellling method will be presented, including the derivation and discussion of the exchange energy, the magneto-crystalline anisotropy, the energy of an externally applied magnetic field, and the stochastic Landau-Lifshitz-Gilbert dynamics

2.1.1 The exchange energy

The exchange energy is the energy resulting from inter-atomic interactions which try to align neighbouring spins. In ferromagnetic materials, the exchange energy is generally the dominant contribution to the spin Hamiltonian and is responsible for long-range magnetic order. The exchange interaction has its origin as a quantum mechanical effect [21–23] and is caused by a combination of the symmetry of the electron wavefunction and the Pauli exclusion principle which dictates possible orientations of spins in overlapping electron orbitals [24, 25].

For a simple derivation [23, 24], consider the simplest case of a system consisting of 2 indistinguishable electrons: one electron at $\mathbf{r_1}$ in state $\psi_A(\mathbf{r_1})$ and another electron at $\mathbf{r_2}$ in state $\psi_B(\mathbf{r_2})$. The combined wavefunction of the system, $\psi(\mathbf{r_1},\mathbf{r_2})$ can be written as the linear combination of the wavefunctions of the 2 constituent electron $\psi(\mathbf{r_1},\mathbf{r_2}) = \psi_A(\mathbf{r_1})\psi_B(\mathbf{r_2})$ which solves the Schrödinger Equation:

$$\left[\frac{\hbar^2}{2m}\nabla_1^2 + \frac{\hbar^2}{2m}\nabla_2^2 + V(\mathbf{r_1}) + V(\mathbf{r_2})\right]\psi(\mathbf{r_1},\mathbf{r_2}) = (E_A + E_B)\psi(\mathbf{r_1},\mathbf{r_2}) = E\psi(\mathbf{r_1},\mathbf{r_2}), \quad (2.1)$$

where the energy of the system, E, is the sum of the energy of the 2 constituent electrons $E = E_A + E_B$ and $V(\mathbf{r_i})$ is the potential at $\mathbf{r_i}$. Since the 2 electrons in the system are indistinguishable,

the wavefunction of the system can also be written as $\psi(\mathbf{r_2},\mathbf{r_1}) = \psi_A(\mathbf{r_2})\psi_B(\mathbf{r_1})$ which also must be another solution to the Schrödinger equation in Eq. (2.1). For this to be the case, the following equality must be upheld:

$$|\psi(\mathbf{r_1},\mathbf{r_2})|^2 d\mathbf{r_1} d\mathbf{r_2} = |\psi(\mathbf{r_2},\mathbf{r_1})|^2 d\mathbf{r_2} d\mathbf{r_1}, \tag{2.2}$$

which yields either a symmetric solution $\psi(\mathbf{r_1},\mathbf{r_2}) = \psi(\mathbf{r_2},\mathbf{r_1})$ or an anti-symmetric solution $\psi(\mathbf{r_1},\mathbf{r_2}) = -\psi(\mathbf{r_2},\mathbf{r_1})$. The general solution to the wavefunction of the system will be a normalised linear combination of either the symmetric or the anti-symmetric solution. However, because the Pauli exclusion principle dictates that no 2 identical electrons in a system can occupy the same quantum state simultaneously, the symmetric solution is not possible. Therefore, the general wavefunction of the system consisting of 2 indistinguishable electrons must be anti-symmetric:

$$\psi_{\text{anti}}(\mathbf{r_1},\mathbf{r_2}) = \frac{1}{\sqrt{2}}\left[\psi_A(\mathbf{r_1})\psi_B(\mathbf{r_2}) - \psi_A(\mathbf{r_2})\psi_B(\mathbf{r_1})\right]. \tag{2.3}$$

To calculate the total energy of the system, the Heitler-London approximation method can be used by which the orbital wavefunction of a system consisting of 2 indistinguishable electrons is approximated as a linear combination of the atomic orbital wave functions of the said 2 constituent electrons each localised on an atomic site [26, 23]. The total energy E is then given by:

$$E = \int\int \psi^*(\mathbf{r_1},\mathbf{r_2})\mathcal{H}\psi(\mathbf{r_1},\mathbf{r_2})\delta\mathbf{r_1}\delta\mathbf{r_2}, \tag{2.4}$$

where the system Hamiltonian $\mathcal{H}$ can be split into the sum of 3 components $\mathcal{H} = \mathcal{H}_1 + \mathcal{H}_2 + \mathcal{H}_{12}$ with $\mathcal{H}_1$ representing the contribution from electron A, $\mathcal{H}_2$ the contribution from electron B, and $\mathcal{H}_{12}$ the contribution from their interaction. The energy component that concerns only the interaction contribution between the 2 electrons can therefore be expressed by replacing the overall $\mathcal{H}$ by the specific $\mathcal{H}_{12}$:

$$E_{12} = \int\int \psi^*(\mathbf{r_1},\mathbf{r_2})\mathcal{H}_{12}\psi(\mathbf{r_1},\mathbf{r_2})\delta\mathbf{r_1}\delta\mathbf{r_2}. \tag{2.5}$$

The interaction energy E_{12} in Eq. (2.5) is made up of firstly, the Coulomb interaction between each of the negatively-charged electron and its respective positively-charged nucleus, and secondly, an exchange interaction component. This exchange interaction component - it has to be emphasised - is purely quantum mechanical in origin because in the classical scenario the exchange interaction between 2 electrons would not alter the system energy. A link between this quantum mechanical exchange interaction and spin correlation can be established by splitting

the total general wavefunction ψ further into the product of a radial part $\phi(\mathbf{r})$ and a spin part χ, such that $\psi(\mathbf{r}) = \phi(\mathbf{r}).\chi$. In order to maintain the already established anti-symmetric nature of the total wavefunction ψ, the radial $\phi(\mathbf{r})$ and spin part χ can neither be both symmetric nor anti-symmetric. Consider the spin part χ first: it can be in either an anti-symmetric singlet state with paired electrons and total spin $S = 0$, or a symmetric triplet state with unpaired electrons and total spin $S = 1$ [27, 28]. Consequently, a system with the spin part in the anti-symmetric singlet state χ_{singlet} will require the radial part to be symmetric ϕ_{sym}. Contrarily, a system with the spin part in the symmetric triplet state χ_{triplet} will require the radial part to be anti-symmetric ϕ_{anti}. Therefore, the total wavefunction with the spin part in the singlet state - ψ_{singlet} - and one with the spin part in the triplet state - ψ_{triplet} - will have the form of:

$$\begin{aligned}\psi_{\text{singlet}}(\mathbf{r_1},\mathbf{r_2}) &= \phi_{\text{sym}}\chi_{\text{singlet}} \\ &= \frac{1}{\sqrt{2}}\left[\phi_A(\mathbf{r_1})\phi_B(\mathbf{r_2}) + \phi_A(\mathbf{r_2})\phi_B(\mathbf{r_1})\right]\chi_{\text{singlet}},\end{aligned} \tag{2.6}$$

and:

$$\begin{aligned}\psi_{\text{triplet}}(\mathbf{r_1},\mathbf{r_2}) &= \phi_{\text{anti}}\chi_{\text{triplet}} \\ &= \frac{1}{\sqrt{2}}\left[\phi_A(\mathbf{r_1})\phi_B(\mathbf{r_2}) - \phi_A(\mathbf{r_2})\phi_B(\mathbf{r_1})\right]\chi_{\text{triplet}},\end{aligned} \tag{2.7}$$

with the energy for each case given by the integral:

$$E_{\text{singlet/triplet}} = \int\int \psi^*_{\text{singlet/triplet}}\mathcal{H}_{12}\psi_{\text{singlet/triplet}}\delta\mathbf{r_1}\delta\mathbf{r_2}. \tag{2.8}$$

The exchange energy between the 2 electrons in the system can then be computed as the difference between the energy of system in the singlet state and in the triplet state:

$$\begin{aligned}E_{\text{exchange}} &= E_{\text{singlet}} - E_{\text{triplet}} \\ &= 2\int\int \left[\phi_A(\mathbf{r_1})\phi_B(\mathbf{r_2})\mathcal{H}_{12}\phi_A(\mathbf{r_2})\phi_B(\mathbf{r_1})\right]\delta\mathbf{r_1}\delta\mathbf{r_2}.\end{aligned} \tag{2.9}$$

In our case with electrons, it is a system of 2 spin-half particles which are coupled by an exchange interaction that can be expressed mathematically by a joint operator $\mathbf{S_{total}} = \mathbf{S_1} + \mathbf{S_2}$ i.e. $\mathbf{S^2_{total}} = \mathbf{S^2_1} + \mathbf{S^2_2} + 2\mathbf{S_1}\cdot\mathbf{S_2}$. Therefore, the exchange energy, which is the energy difference between the singlet and triplet state, will take the form of a multiplier of $\mathbf{S_1}\cdot\mathbf{S_2}$. Combining the 2 spin-half particles will result in a system with spin quantum number of either $S = 0$ (i.e. overall singlet) if the 2 spin-halves are anti-parallel, or $S = 1$ (i.e. overall triplet) if the 2 spin-halves are parallel. Since the magnitude of the squared spin operator $\mathbf{S}^2$ is given by $S(S+1)$, for the singlet

case it reads $0(0+1) = \frac{1}{2}\left(\frac{1}{2}+1\right) + \frac{1}{2}\left(\frac{1}{2}+1\right) + 2\mathbf{S_1}\cdot\mathbf{S_2}$ i.e. $0 = 3/2 + 2\mathbf{S_1}\cdot\mathbf{S_2}$ which yields $\mathbf{S_1}\cdot\mathbf{S_2} = -3/4$. Similarly, for the triplet case it reads $1(1+1) = \frac{1}{2}\left(\frac{1}{2}+1\right) + \frac{1}{2}\left(\frac{1}{2}+1\right) + 2\mathbf{S_1}\cdot\mathbf{S_2}$ i.e. $2 = 3/2 + 2\mathbf{S_1}\cdot\mathbf{S_2}$ which yields $\mathbf{S_1}\cdot\mathbf{S_2} = 1/4$ [24, 27]. The effective Hamiltonian of the system of 2 electrons, therefore, can be written in this form [24]:

$$\begin{aligned}\mathcal{H} &= \frac{1}{4}(E_{\text{singlet}} + 3E_{\text{triplet}}) - (E_{\text{singlet}} - E_{\text{triplet}})\mathbf{S_1}\cdot\mathbf{S_2} \\ &= \mathcal{H}_{\text{radial}} + \mathcal{H}_{\text{spin}},\end{aligned} \tag{2.10}$$

which yields the eigenvalue E_{singlet} for the singlet state i.e. when $\mathbf{S_1}\cdot\mathbf{S_2} = -3/4$ and E_{triplet} for the triplet state i.e. when $\mathbf{S_1}\cdot\mathbf{S_2} = 1/4$ as is desired. Note that the first term of the effective Hamiltonian, $\mathcal{H}_{\text{radial}}$, does not include any spins and thus can be defined as a spin-independent radial component, whilst the second term $\mathcal{H}_{\text{spin}}$ includes the spins and thus can be defined as a spin-dependent spin component. Since the spin component $\mathcal{H}_{\text{spin}}$ is summed up for both electrons, the contribution from each electron can be calculated by halving it:

$$\mathcal{H}_{\text{spin}} = -\frac{1}{2}(E_{\text{singlet}} - E_{\text{triplet}})\mathbf{S_1}\cdot\mathbf{S_2}, \tag{2.11}$$

and from Eq. (2.11) the exchange constant J_{exchange} can then be defined as:

$$J_{\text{exchange}} = \frac{1}{2}(E_{\text{singlet}} - E_{\text{triplet}}) = \int\int \phi_A(\mathbf{r_1})\phi_B(\mathbf{r_2})\mathcal{H}_{spin}\phi_A(\mathbf{r_2})\phi_B(\mathbf{r_1})\delta\mathbf{r_1}\delta\mathbf{r_2}, \tag{2.12}$$

which helps to simplify the exchange Hamiltonian in the system of indistinguishable 2 electrons to:

$$\mathcal{H}_{\text{exchange}} = -J_{\text{exchange}}\left(\mathbf{S_1}\cdot\mathbf{S_2}\right). \tag{2.13}$$

Generalise this result to a generic system consisting of many particles:

$$\mathcal{H}_{\text{exchange}} = -\frac{1}{2}\sum_{i,j} J_{ij}\left(\hat{\mathbf{S}}_i\cdot\hat{\mathbf{S}}_j\right), \tag{2.14}$$

where J_{ij} is the exchange energy strength between $\hat{\mathbf{S}}_i$ and $\hat{\mathbf{S}}_j$ the unit vector of local spin at site i and j respectively. Note the factor of $1/2$ is added in order to avoid double counting of duplicate (i,j) and (j,i) pairs. In atomistic simulations, the exact form of J_{ij} generally depends on the specific form of the exchange interaction present in the system. For example, in a simple scenario J_{ij} can be treated as a simple scalar quantity, whilst in a more complex case J_{ij} can take the form of a tensor. Generally, $J_{ij} > 0$ corresponds to a system with quantised-parallel, triplet-state ferromagnetic (FM) spin configuration, whilst $J_{ij} < 0$ refers to an anti-parallel, singlet-state anti-ferromagnetic (AFM) spin configuration [28, 23]. The numerical value of J_{ij}

used in atomistic simulations is typically obtainable from either ab-initio calculations or fitting to experimental data [29, 30]. Additionally, another important note is that although in Eq. (2.14) the exchange interaction between all pairs of spins present in the system are accounted for - thus can be conveniently referred to as the "full" exchange Hamiltonian, the magnitude of the exchange energy decreases quickly with increasing distances between increasing levels of nearest-neighbours. Therefore, in practice the exchange contributions from further than the third-level of nearest neighbours can often be safely ignored [31]. This point will be revisited with greater depth in the specific discussions later on the modelling of Iron Platinum in the $L1_0$ phase ($L1_0$-FePt).

2.1.2 The magnetocrystalline anisotropy

Anisotropy refers to the spatial preference of the magnetic properties of a material caused by the preferential alignment of the spins in a material along a specific direction. There are many types of anisotropy, and thus many origins and mechanisms. A convenient way to visualise anisotropy can be achieved by an example of what is known as shape anisotropy, which takes roots in the geometry of a particle. Consider a uniformly magnetised particle which is elongated in shape along a specific direction as seen in Fig. 2.1. Similar to the case of dielectrics, when an external magnetic field H is applied, magnetic polarisation will happen leading to the formation of fictitious magnetic poles at the surface, which in turn leads to the creation of a demagnetising field H_d within the particle in opposition to the external field H. Because the said particle is elongated in a specific direction, the demagnetising field cannot be the same in all directions i.e. an-isotropic. In the particular case of the particle in Fig. 2.1, the demagnetising field H_d will be largest when the external field H_d is applied parallel to the short axis because of the shortest distance separating the 2 magnetic poles, and smallest when H_d is applied along the long axis because of the longest separating distance. Since H_d opposes H, the spins will prefer to align along the long axis where H_d is smallest, or the axis of elongation, leading to the anisotropy of the particle. To make the spins deviate away from the preferred axis, therefore, will require an energy imposed on the system. This energy is called the anisotropy energy [32].

The most common source of anisotropy is known as the magneto-crystalline anisotropy which occurs due to the spin-orbit coupling of the electrons under influence of the crystallographic structure of the material [32, 33]. Spin-orbit coupling is a relativistic effect which determines the interaction between the spin of a particle and its orbital angular momentum around the nucleus [34], whilst the crystallographic structure represents the local crystal symmetries which decide the spatial orientation and arrangement of electron orbitals. Since electron orbitals are generally non-spherical, they tend to orient along specific crystallographic directions. Therefore, when electron spins interact with orbitals, the spins are induced to “prefer”

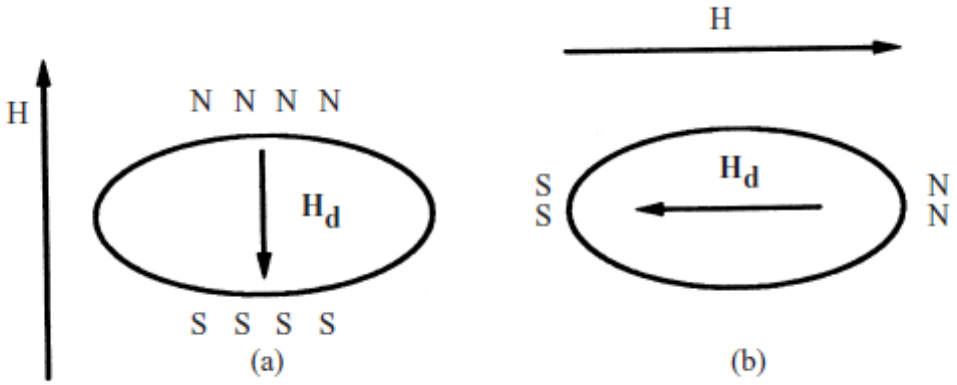

Fig. 2.1 Shape anisotropy in an elongated particle. The demagnetising field H_d is largest when the external field H is applied (a) along the short axis, and smallest when H is applied along the (b) long axis. Thus the preferred direction for the spins to align is along the long axis i.e. the axis of elongation. Source: excerpt from [33].

the alignment along well-defined crystallographic axes which are known as easy axes or easy directions. This preference is the root of the magneto-crystalline anisotropy, which as expected heavily depends on the lattice structure of a material. Similar to the aforementioned case of shape anisotropy, trying to push the spins away from their preferred easy directions will cost anisotropy energy [33].

Magneto-crystalline anisotropy includes many forms. The simplest case is known as uniaxial anisotropy, in which, as the name suggests, the spins prefer to align along a single axis. Uniaxial anisotropy is commonly encountered in materials with shape distortion along a specific direction, for example Iron Platinum in the $L1_0$ phase because of the alternating Iron-Platinum layers on the z-dimension, or hexagonal crystals such as Cobalt. The expression of uniaxial anisotropy energy is given as:

$$\mathcal{H}_{\text{anisotropy}} = -k_u \sum_i (\hat{\mathbf{S}}_i \cdot \hat{\mathbf{e}})^2, \tag{2.15}$$

where $\hat{\mathbf{S}}_i$ is the spin at site i and k_u the uniaxial anisotropy constant having an easy direction along $\hat{\mathbf{e}}$. Generally, uniaxial anisotropy energy can be written in terms of series of anisotropy constants [35] as:

$$E_{\text{anisotropy}} = KV \sin^2(\phi) + \text{higher} - \text{order terms}, \tag{2.16}$$

where ϕ is the angle between the easy direction and the magnetisation, K the first uniaxial anisotropy constant (also often denoted K_2 and called the second-order uniaxial constant

corresponding to the second-order of $\sin(\phi)$), and V the volume of the sample. Higher-order terms correspond to higher-order powers of trigonometric functions and are usually insignificant compared to the first term, thus normally neglected. This expression produces the uniaxial anisotropy energy along one easy axis with two energy minima, separated by a maximum. The resulting energy barrier leads to hysteresis [33].

2.1.3 The energy of an externally applied field

The presence of an externally applied magnetic field, $\mathbf{B}_{\text{applied}}$ or where possible for simplicity just $\mathbf{B}$, will have an impact on the energy levels of electrons within a given magnetic system. The interaction between a given magnetic system and an external magnetic field follows principles of the Zeeman effect [36], and the potential energy resulting from such interaction, $\mathcal{H}_{\text{field}}$, is given as:

$$\mathcal{H}_{\text{field}} = -\sum_i \mu_i (\hat{\mathbf{S}}_i \cdot \mathbf{B}), \tag{2.17}$$

where μ_i is the atomic spin moment of spin $\hat{\mathbf{S}}_i$ and $\mathbf{B}$ the externally applied magnetic field. The total potential energy is summed up from all sites i of the system. It can be seen that the coupling strength between spin $\hat{\mathbf{s}}_i$ and the field $\mathbf{B}$ is proportional to the magnitude of the magnetic moment μ_i, and minimum energy is attained when all spins align with the direction of the external field.

2.1.4 The stochastic Landau-Lifshitz-Gilbert equation

The time-dependent dynamics of a magnetic system is described by the Landau-Lifshitz equation [37] which is given as:

$$\frac{\partial \mathbf{M}}{\partial t} = -\gamma_e \mathbf{M} \times \mathbf{H} - \gamma_e \alpha \mathbf{M} \times (\mathbf{M} \times \mathbf{H}), \tag{2.18}$$

where $\gamma_e = 1.76 \times 10^{11} rads^{-1}T^{-1}$ is the gyro-magnetic ratio of an electron, $\mathbf{M}$ the magnetisation, $\mathbf{H}$ the externally applied magnetic field, and α a phenomenological damping constant specific to the material. This equation consists of two terms. The first term is a precession term which describes an un-damped precession of a magnetisation around an applied field, and the second term the damping term which accounts for the relaxation of the magnetisation towards the effective field direction under the added effect of damping. A damped precession eventually aligns the magnetisation along the external magnetic field. It was later found that the Landau-Lifshitz equation is valid only for systems with small damping; otherwise, the damping term had to be rectified by Gilbert in 1956. This rectified damping term transformed the

original Landau-Lifshitz equation to the Landau-Lifshitz-Gilbert (LLG) equation [38]. For atomistic spin dynamics, the LLG equation can be expressed for each magnetic spin by converting the magnetisation $\mathbf{M}$ to the spin $\mathbf{S}$ via the relation $\mathbf{M} = \mu_s \mathbf{S}$ with μ_s being the local spin moment. Another important note is that in the macroscopic-LLG the phenomenological damping constant α includes both intrinsic contributions (such as spin–lattice and spin–electron interactions) and extrinsic contributions (such as spin-spin interactions arising from demagnetisation fields, surface defects, doping, temperature), while the atomistic-LLG only includes the local intrinsic damping contributions. Therefore, in order to distinguish the two forms of damping, a microscopic damping constant λ needs to be used to replace the phenomenological damping constant α [39]. This leads to the atomistic-LLG equation:

$$\frac{\partial \mathbf{S}_i}{\partial t} = -\frac{\gamma_e}{1+\lambda^2}\mathbf{S}_i \times (\mathbf{H}_i + \lambda \mathbf{S}_i \times \mathbf{H}_i), \tag{2.19}$$

where $\mathbf{S}_i$ is the spin of site i and $\mathbf{H}_i$ the corresponding effective magnetic field acting on it. The effective field is derived from the first derivative of the complete spin Hamiltonian $\mathcal{H}$ which is given as:

$$\mathbf{H}_i = -\frac{1}{\mu_s}\frac{\partial \mathcal{H}}{\partial \mathbf{S}_i}. \tag{2.20}$$

Since the description of the atomistic-LLG equation does not include any temperature-dependent term, it is strictly valid at $T = 0K$ only and thus can also be referred to as the "deterministic" LLG. In order to extend its applicability to non-zero temperatures, i.e. to account for thermal effects, a stochastic term $\xi_i(t)$ has to be added to the effective field $\mathbf{H}_i$ in Eq. (2.20) which now reads:

$$\mathbf{H}_i = -\frac{1}{\mu_s}\frac{\partial \mathcal{H}}{\partial \mathbf{S}_i} + \xi_i(t). \tag{2.21}$$

The introduction of the stochastic term $\xi_i(t)$ is known as the Langevin Dynamics in which the thermal fluctuations are given in form of a zero-mean Gaussian distribution in three dimensions [39, 40]. It has been shown that the stochastic term $\xi_i(t)$ can be defined through these correlations:

$$\begin{aligned} \langle \xi_i(t) \rangle &= 0 \\ \langle \xi_{i\eta}(t)\xi_{j\upsilon}(t') \rangle &= \frac{2\lambda k_B T}{\gamma_e \mu_s}\delta\left(t-t'\right)\delta_{ij}\delta_{\eta\upsilon}, \end{aligned} \tag{2.22}$$

where the notation $\langle\rangle$ denotes the mean value averaging over different realisations of the fluctuation field, i and j the spin sites, η and υ the Cartesian coordinates, t and t' the time at which the Gaussian fluctuations are evaluated, $k_B T$ the thermal energy with $k_B = 1.38 \times 10^{-23} J/K$ being the Boltzmann constant and T the absolute temperature in Kelvin, δ_{ij} and $\delta_{\eta\upsilon}$

the Kronecker Delta of respective indices, and $\delta(t-t')$ the Delta function. The addition of the stochastic term $\xi_i(t)$ to the effective field $\mathbf{H}_i$ converts the deterministic-LLG to the stochastic-LLG. An illustration that compares the dynamics of undamped precession, deterministic-LLG, and stochastic-LLG is shown in Fig. 2.2.

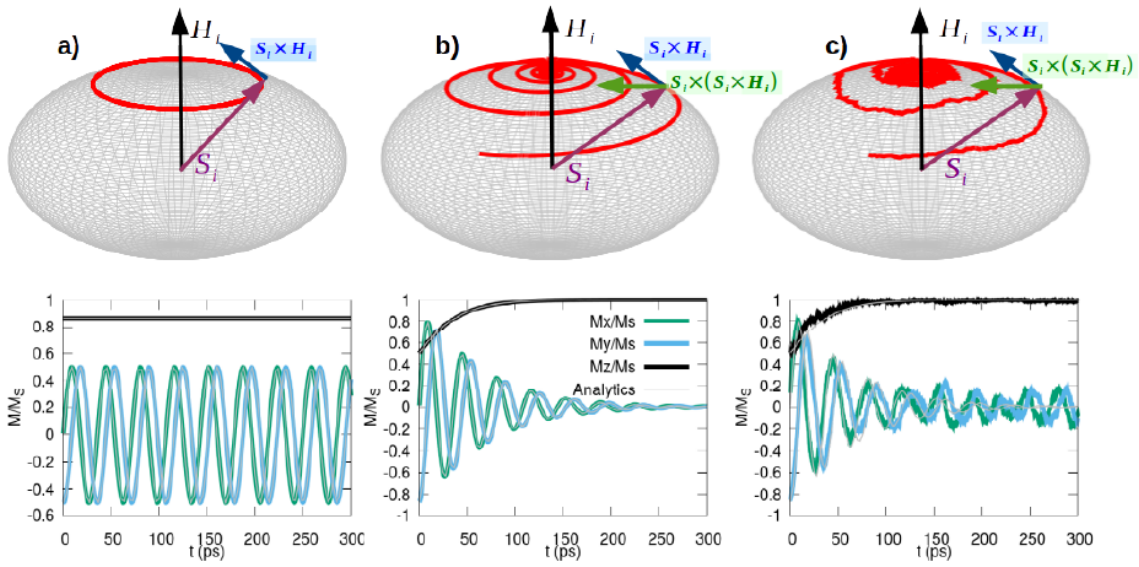

Fig. 2.2 The dynamics of (a) undamped precession, (b) deterministic-LLG (strictly $T = 0$), and (c) stochastic-LLG ($T \geq 0$). The black arrow indicates the effective field $\mathbf{H}_i$ acting on the spin $\mathbf{S}_i$ (purple arrows) together with the precession (blue arrows) and damping (green arrows) energy terms, which result in the red trajectory. The lower plots show the temporal evolution of the three magnetisation components. The Analytics line corresponds to an analytic solution to the LLG equation in a special case, with further discussion in [41]. Source: excerpt from [41].

2.2 A review of magnetic modelling frameworks

The origin of long-range magnetic order in a sub-class of magnetic materials is a fundamental scientific question which despite extensive investigation remains yet to be fully understood. In the field of magnetism, there has not been a single comprehensive, universally accepted grand theory applicable on all length-scales over all time-scales which could successfully capture and explain all the complex magnetic properties of magnetic materials. Instead, today there are three widely used computational frameworks which are still being continuously developed for the study of magnetic materials: Micromagnetics, Atomistic, and Ab-initio in a decreasing order of level of length-scale of the studied system. Given a particular question, depending on

the level of complexity that it poses, a specific degree of precision will be required and one of the three available modelling frameworks might be best suited to study the said question.

2.2.1 Micromagnetics

Overview

The oldest of the three computational frameworks is Micromagnetics. The birth of Micromagnetics can be traced back to a paper by Landau and Lifshitz in 1935 on the structure of a domain wall between two anti-parallel domains [37], followed by further studies by W. F. Brown in the 40s. The groundwork of the Micromagnetics model is laid out by Brown two decades later in his book "Micromagnetics" [42]. Micromagnetics as a theory is proposed to link classical Electromagnetism with Heisenberg's quantum mechanical treatment of the exchange energy [21]. At the foundation of Micromagnetics is the hypothesis that macroscopic magnetic properties arise from a combination of two factors: first, the very short-range exchange energy between neighbouring atomistic spins, and second, the longer-range magnetostatic energy which includes surface and boundary contributions from the shape of the material [43]. Obviously, these two factors are effective on entirely different length-scales, and therefore the objective of Micromagnetics is to provide a framework which enables the computational investigation of macroscopic properties of a material using a reasonable approximation of its microscopic properties.

Micromagnetics is most suitable to study systems at the length-scale of micrometres at which it is both sufficiently small to retain the classical representation of atomic spins and sufficiently large to resolve magnetic domains. The underlying principle is to replace atomistic spins by a continuous vector field which can be used to calculate magnetostatic fields within the system. In particular, in a ferromagnetic system, atomistic spins aligning in a co-linear orientation due to an internal magnetic field are collectively combined as macrospins, with each macrospin being assigned the representative equivalence of a magnetisation vector. In Micromagnetics theory, these macrospins function as irreducible building blocks upon which other magnetic properties of the said ferromagnetic system can be fully derived. The exact definition of macrospins, however, varies across different Micromagnetics frameworks [44]: the finite-difference approach divides the system into a finite mesh of cuboids with each cuboid represented by a macrospin, whilst in the finite-element method the discretised finite mesh can be made up of tetrahedral- or triangular-shaped elements. An illustration of comparison between the two methods is shown in Fig. 2.3: it can be seen that the finite-element method allows more flexible covering of irregular surfaces without increasing computational cost, thus resulting in a smoother discretisation of the system. The replacement of the atomistic spins

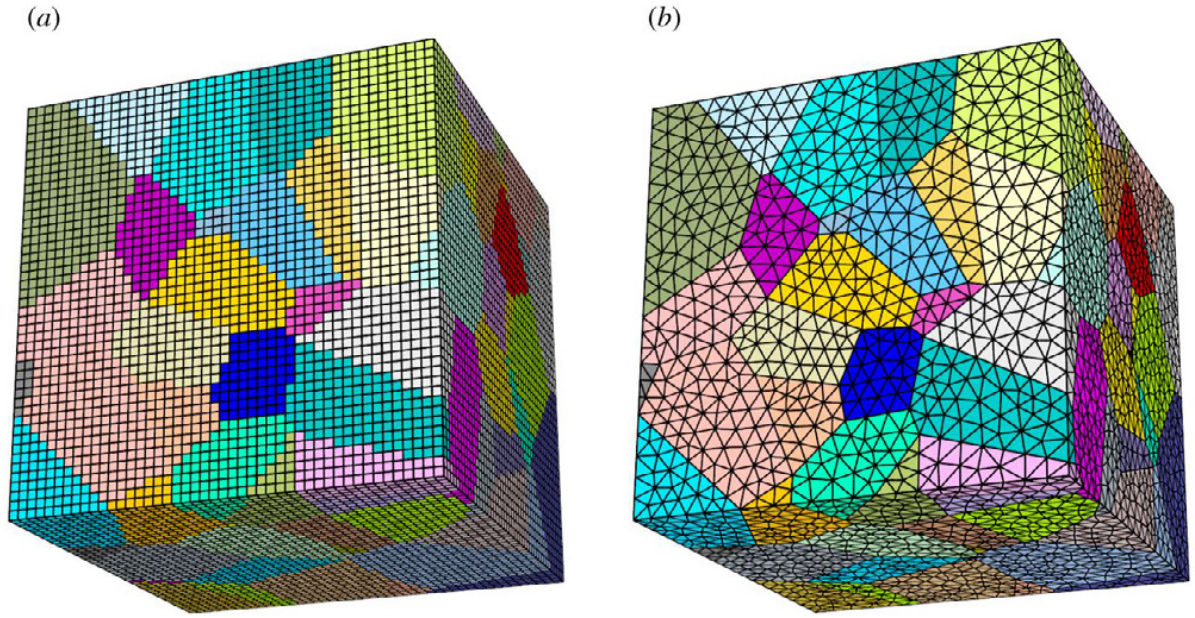

Fig. 2.3 Comparison of (a) the finite-difference and (b) finite-element meshes with different shapes of elements in the discretised system. Source: excerpt from [44].

by the magnetisation vector field then allows the replacement of the Heisenberg's quantum mechanical treatment by a continuous approximation formalism of the exchange interaction. This approximation to the exchange interaction and the energy minimisation principle form the basis of the classical Micromagnetics formalism [33].

Different computational models based on Micromagnetics are capable of simulating large systems of multi-micrometres in sizes over microseconds in time with acceptable degrees of precision [45–49]. The downsides of Micromagnetics, however, lies inherently in its fundamental assumption of a continuous magnetisation vector field since the macrospin representation method does not allow sufficiently rapid spatial variation of the magnetisation vector. Furthermore, the resolution limit of the model is at a length-scale usually much larger than a typical atomistic lattice spacing, which explains why the exchange energy can only be approximated. Overall, Micromagnetics have been proven less than ideal for the calculation of magnetic properties when a very high level of precision is desired, especially at elevated temperatures such at the Curie temperature. Simply put, Micromagnetics is not the best tool available nowadays to determine intrinsic material properties; rather, it is useful for determining how the material, with known properties, will behave.

Formalism

The basic formalism of Micromagnetics can be summarised as following [33]. Under the Heisenberg's quantum mechanical treatment of exchange interaction, the exchange energy between neighbouring pairs of atomistic spins $\hat{\mathbf{S}}_i$ and $\hat{\mathbf{S}}_j$ is given by:

$$E_{\text{exchange}} = -2J_{ij}\left(\hat{\mathbf{S}}_i \cdot \hat{\mathbf{S}}_j\right), \tag{2.23}$$

where J_{ij} is the exchange integral as discussed earlier. Generally, J_{ij} assumes positive values for ferromagnetic materials and negative values for anti-ferromagnetic materials. Also, J_{ij} depends on the specific distance between the two atoms in consideration. The fundamental principle of Micromagnetics assumes the magnetisation to be a continuous vector field $\mathbf{M}(\mathbf{r})$ of the position vector $\mathbf{r}$ satisfying:

$$\mathbf{M}(\mathbf{r}) = M_s \mathbf{m}(\mathbf{r}), \tag{2.24}$$

where M_s is the saturation magnetisation and $\mathbf{m}(\mathbf{r}) \cdot \mathbf{m}(\mathbf{r}) = 1$. The basic approach of Micromagnetics involves calculating the magnetic energy in term of this continuous magnetisation vector field and then minimise the energy to determine static magnetisation structures of the material. For the exchange energy, this is done by assuming a short-range summation over nearest neighbouring atoms i and j only and a slow spatial variation of the magnetisation vector $\mathbf{m}(\mathbf{r})$. A slow spatial variation of the magnetisation vector means that the dot-product between neighbouring spins $\hat{\mathbf{S}}_i$ and $\hat{\mathbf{S}}_j$ can be expressed as $\hat{\mathbf{S}}_i \cdot \hat{\mathbf{S}}_j = S^2 \cos\left(\phi_{ij}\right)$, where the angle ϕ_{ij} between spin $\hat{\mathbf{S}}_i$ and $\hat{\mathbf{S}}_j$ is small. Therefore, applying the first-order expansion of the Taylor series of cosine (dropping the constant 1) will transform Eq. (2.23) to:

$$E_{\text{exchange}} = -2JS^2 \sum_{i,j} \cos\left(\phi_{ij}\right) = -2JS^2 \sum_{i,j} \frac{-\phi_{ij}^2}{2} = JS^2 \sum_{i,j} \phi_{ij}^2. \tag{2.25}$$

Since ϕ_{ij} is a small angle, following Equation (2.24) it can be approximated as the difference between $\mathbf{m}_i$ and $\mathbf{m}_j$ of neighbouring spins i and j, which can be further expanded as:

$$\phi_{ij} \approx |\mathbf{m}_i - \mathbf{m}_j| = |\left(\mathbf{s}_i \cdot \nabla\right)\mathbf{m}_j|^2, \tag{2.26}$$

where $\mathbf{s}_i$ is the displacement vector between the lattice point i and j. Substitute Eq. (2.26) into Eq. (2.25) to obtain:

$$E_{\text{exchange}} = JS^2 \sum_{i} \sum_{\mathbf{s}_i} |\left(\mathbf{s}_i \cdot \nabla\right)\mathbf{m}_j|^2, \tag{2.27}$$

where the first summation involving each spin i can be converted into a volume integral over the entire system. Also, note that the second summation involving $\mathbf{s}_i$ is carried out over nearest-neighbour spins of the referenced spin i only. Consider the calculation of E_{exchange} in the simplest case of a system of simple cubic crystal structure with a lattice constant a:

$$E_{\text{exchange}}^{\text{cubic}} = \oint_V \frac{JS^2}{a} (\nabla \mathbf{M})^2 \, dV, \tag{2.28}$$

where $(\nabla \mathbf{M})^2 = (\nabla \mathbf{M_x})^2 + (\nabla \mathbf{M_y})^2 + (\nabla \mathbf{M_z})^2$ [33]. The material constant A can be defined as $A = JS^2/a$. Eq. (2.28) is significant in the regard that it has established a relation between the intrinsic atomistic properties of the material - represented via the exchange integral J which can be obtained from experiment - and the continuous magnetisation vector field - represented via the spatial gradient $(\nabla \mathbf{M})$. Therefore, the fundamental hypothesis of Micromagnetics has now been fulfilled.

Additionally, it is important to note a critical limitation of the classic energy minimisation principle that whilst it can help to determine the nucleation fields of a micromagnetic system, it is incapable of making a consistently accurate description of the state of the system after magnetisation reversal [33]. A solution to this weakness is found in the development of dynamic approaches instead, which are based on the Landau-Lifshitz equation of motion [37]. The first progress was made by Gilbert in 1956, later known as the Landau-Liftshitz-Gilbert (LLG) equation [38], in which the damping effect is added to the classical description of an un-damped precessional motion by using a Rayleigh dissipation function. However, the LLG model still adheres to the fundamental micromagnetic assumption of a slow spatial variation of the magnetisation vector - which means the magnetisation length remains unchanged. This requirement restricts the applicability of the LLG model to low temperatures only where ferromagnetic order still remains conserved and no loss of magnetisation of the macrospins has occurred. The next significant improvement was achieved in 1997 when a closed equation of motion for magnetisation - now known as the LLB equation - was derived which interpolated between the classical Landau-Lifshitz equation at low temperatures the and Bloch equation at high temperatures [50]. Therefore, the new LLB model finally enabled the simulation of micromagnetic systems at both high and low temperature range, and both the LLG and LLB models have remained in common use today.

2.2.2 Ab-initio and atomistic Spin models

In contrast to Micromagnetics, the most recent computational framework is the ab-initio approach which aims to produce a discrete description of a simulated system down at the

electronic length-scale. Magnetic properties can be calculated directly from electronic structure via first principles without the need of approximation. As a result, a very high level of precision of calculation can be achieved. However, the cost of an extraordinary level of precision is a severe restriction in length-scale where only few thousands of atoms can be simulated even on massively parallel computers [51]. Since the magnetic system that can be simulated using the ab-initio method is far too small in size, dynamics calculations - especially of properties that are heavily dependent on size effects such as the Curie temperature - are extremely limited. The ab-initio framework today, despite promising potentials, has still remained largely under development.

The atomistic framework, therefore, has its place as a compromise between the large length-scale of Micromagnetics and the high precision of ab-initio. In particular, a typical atomistic model will utilise material magnetic parameters that can be obtained from ab-initio calculations - for example electronic structure, exchange integral, anisotropies, magnetic moments etc.- in a system of the length-scale of nanometres consisting of millions of atoms via higher order of approximation than that of Micromagnetics [39]. Since the spins are no longer replaced by a continuous magnetisation vector field as in Micromagnetics, although still necessarily assumed having fixed lengths, rapid spatial variation is made possible. Furthermore, the resolution limit is now comparable to atomistic lattice spacing so in comparison to Micromagnetics, a more precise calculation of not only the exchange energy but also other magnetic properties at all temperature ranges can be achieved. Although the atomistic approach is less precise than ab-initio, it requires much less computational cost and can simulate much larger systems, thus being much more flexible with dynamics calculations. A detailed description of fundamental concepts of the atomistic modelling method has already been presented in the preceding section 2.1.

2.3 The VAMPIRE atomistic simulation software package

The Atomistic modelling method which has so far been discussed in this Chapter has been implemented into the VAMPIRE code, an open-source atomistic spin dynamics software package developed by the Computational Magnetism group at the University of York [39, 52]. The code base is written in C++ and can run on most hardware, in either serial, parallel or GPU modes. The work carried out in this Thesis is mainly conducted from simulations performed by VAMPIRE which handles both simulations and data output. The simulations are all run extensively on the VIKING Cluster, which a high performance compute facility provided by the University of York. In this Section, the main operating principles of the VAMPIRE code will be outlined.

2.3.1 The Monte-Carlo and constrained Monte-Carlo methods

Time-dependent dynamics and properties can be investigated in the VAMPIRE atomistic code using the LLG equations. In this case, the calculation is performed from the starting point of the simulation through the equilibrium point where the system is fully relaxed. However, the time-scale for this whole calculation to be completed is usually impractically long. Meanwhile, there are scenarios where the interest lies solely with the investigation of the final equilibrium point, not the entire dynamics of the process. In these situations, an alternative to the LLG is required, which is found in the Metropolis Monte-Carlo algorithm [53]. The Metropolis Monte-Carlo algorithm, or for convenience just Monte-Carlo, is a very robust and efficient algorithm to determine equilibrium properties without the cost of fully investigating the intermediate dynamics.

In a classical spin system, the Monte-Carlo algorithm starts with choosing a random spin at site i being at the initial direction $\mathbf{S}_i^{initial}$. The direction of the said spin is then moved to a new direction, called a "trial" direction, $\mathbf{S}_i^{final}$ and the energy difference between the 2 directions is calculated as $\Delta E = E(\mathbf{S}_i^{final}) - E(\mathbf{S}_i^{initial})$. Whether this move will be accepted or rejected will be decided by calculating the acceptance probability P given by:

$$P = \exp\left(-\frac{\Delta E}{k_B T}\right), \tag{2.29}$$

where k_B is the Boltzmann constant and T the temperature (Kelvin) at the moment of the trial move. It can be immediately noted that in the special case where $\Delta E < 0$ i.e. the energy of the trial state is less than the energy of the initial state, $P > 1$ and thus the move is automatically accepted. Otherwise, if $P < 1$, the acceptance probability P will then be compared to a random number between 0 and 1, and the trial move will only be accepted if P is larger than the said number. The purpose of this trial move is to allow for thermal fluctuations to cause a small increase in energy before making the decision to accept the move or not. The whole process is applied for every spin in the system, and once the outcomes have been determined for all spins in the system it is said that one single Monte-Carlo step has been completed.

There are two requirements for a valid Monte-Carlo process: reversibility and ergodicity. First, reversibility means that the probability of a move from position A to B must be the same as from B to A. This requirement is immediately satisfied by Eq. (2.29) since the acceptance probability P depends only on the initial and final energy. Second, ergodicity, requires that all moves should be possible so that all states are accessible. This is mainly true at high temperatures where the probabilities of moves can be considered equally probable. However, at low temperatures, the exchange energy only allows moves which result in small deviations in spin direction, hence most trial moves will likely be rejected. A solution is to use a more tuned

step size, for example a Gaussian trial move algorithm developed by Hinzke and Nowak [54] which ensures a uniform distribution of points but allows the angular displacement of the spin moments to be tuned to the temperature. A trial step, $\mathbf{S}_i^{trial}$, is made from the initial spin position, $\mathbf{S}_i^{initial}$ by:

$$\mathbf{S}_i^{trial} = \mathbf{S}_i^{initial} + \delta_i^k, \tag{2.30}$$

where the superscript k refers to the x, y, z direction and δ_i^k, also on the respective coordinate direction, is a Gaussian random number with a mean of zero and width ρ where ρ is a function of temperature. The new trial spin position is then normalised to unit length [55]. The width of the Gaussian distribution needs to be predetermined so as to yield an acceptance rate of Monte-Carlo moves at around 50 percent, which is required for an optimal sampling of the phase space [31].

Later developments of the Metropolis Monte-Carlo algorithm led to a modification known as the Constrained Monte-Carlo method [56]. The Constrained Monte-Carlo method enables the traversing of the phase space of a classical spin system while in the meantime fixing the direction of the magnetisation vector $\mathbf{M}$. One direct application of the Constrained Monte-Carlo method, which will be discussed in more details in Chapter 4, is that an atomistic simulation can be run in which magnetisation vector $\mathbf{M}$ can be constrained at and angle θ to the easy axis. The Constrained Monte-Carlo method has been shown to be capable of modelling the temperature dependence of magnetic anisotropy, in particular for bulk uniaxial and cubic anisotropies it can successfully reproduces the low-temperature Callen-Callen power laws of $\mathbf{M}$ [57]. The basic principles of the Constrained Monte-Carlo method is to compute thermodynamic properties by averaging over the Boltzmann distribution using the Metropolis algorithm by which the elementary moves of the random walk can be modified so as to conserve the average magnetization direction $\hat{\mathbf{M}} = \left(\sum_i \hat{\mathbf{S}}_i\right) / ||\sum_i \hat{\mathbf{S}}_i||$. The key benefit this method offers is that the system can be kept out of thermodynamic equilibrium in a controlled manner whilst its microscopic degrees of freedom are still allowed to thermalise. It is important to note that since the system is not allowed to reach full equilibrium, the average of the total internal torque does not vanish and is shown to be equal to the macroscopic torque on the system. From this torque, the temperature-dependence anisotropy constants can be calculated.

2.3.2 The temperature rescaling method

The VAMPIRE atomistic code can model a very wide range of magnetic materials of various forms. Material parameters obtained from ab-initio or experiments can be input into VAMPIRE simulations to produce well defined outputs of the simulated system. However, in comparison with experimental literature, a disparity has been noticed in the temperature-scaling behaviours

of the magnetisation or specific heat. The main cause of this disparity lies in the classical in nature of the VAMPIRE model where the spins are defined as localised, classical atomistic on the surface of the unit sphere. Therefore, in a classical system, the spins can be assigned in any directions. However, in reality magnetic spins at the atomistic length-scale obey principles of quantum mechanics, thus being quantised to particular eigenvalues and constrained to particular directions. This effect leads to different thermodynamic outputs at the macroscopic scale.

A solution to this problem is proposed by Evans et al. [58]. The key idea is to apply a temperature-rescaling method to equate the temperature-dependent magnetisation obtained from a classical regime with that from a quantum mechanical regime. An illustration for the effect of temperature-rescaling on the physical representation of the spins is shown in Fig. 2.4

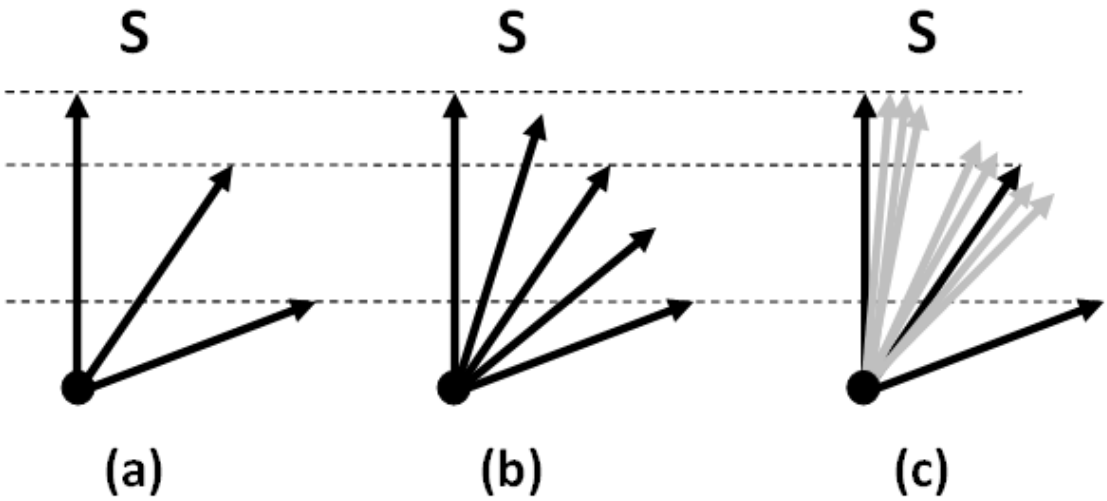

Fig. 2.4 The effect of temperature rescaling on the physical representation of spins in (a) a quantum mechanical regime where the spins are quantised and restricted to specific directions, (b) a classical regime where the spins can take any directions, and (c) a classical regime with temperature-rescaling where the spins are "rescaled" as close as possible to the available quantised states as in a quantum mechanical regime. Source: courtesy of Dr. Sarah Jenkins.

It is found that the effect of spin quantisation is negligible in the high temperature range close to the Curie temperature T_C of the material where the magnetisation generally obeys the scaling power law:

$$M(\tau) = (1-\tau)^{\beta}, \tag{2.31}$$

where $\tau = T/T_C$ is the reduced temperature and β the critical scaling exponent. For a Heisenberg model, the numerical value of β is usually taken as $1/3$ [59, 60]. It is observed that the behaviours of classical and quantum mechanical regimes can be easily related at low tempera-

tures, and converge at high temperatures. Therefore, it is suggested that the Bloch's law [24] which governs low-temperature behaviour can be extrapolated to link with high-temperature behaviour which follows the aforementioned scaling power law. The result is a good match between both regimes for all temperatures which can be formalised using the Curie-Bloch equation:

$$M(\tau) = (1 - \tau^{\alpha})^{\beta}, \tag{2.32}$$

where α is the temperature-rescaling exponent. Note that since the parameter β is assumed to be the same for both classical and quantum mechanical regime, the temperature-rescaling exponent α is the only parameter required to be determined from fitting to experimental data. Once an appropriate value of α and the Curie temperature T_C of the material have been found, a VAMPIRE simulation can be rerun with the temperatures being rescaled by:

$$\frac{T_{\text{simulation}}}{T_C} = \left(\frac{T_{\text{experiment}}}{T_C}\right)^{\alpha}. \tag{2.33}$$

This temperature-rescaling method has been applied to elemental ferromagnets and shown to be able to produce outputs in very good agreement with experimentally measured magnetisations for all studied materials [58]. A sampled comparison can be seen in Fig. 2.5.

2.3.3 The atomistic Spin Hamiltonian

In the Atomistic model adopting Monte-Carlo simulations, the energy of a magnetic system is described in terms of the Spin Hamiltonian $\mathcal{H}$ as the sum of all energy contributions [28]. The three most important contributions include the exchange interaction between pairs of local spins $\mathcal{H}_{\text{exchange}}$, the magnetic uniaxial anisotropy $\mathcal{H}_{\text{anisotropy}}$, and the externally applied magnetostatic field $\mathcal{H}_{\text{field}}$. In most cases, all these three major contributions need to be accounted for since the dynamics of the simulated material depends on the balance between these energy terms. It is generally unfeasible to treat the magnetostatic and anisotropy contribution as a perturbation of the exchange energy using a quantum mechanical approach. The explicit form and/or derivation of these three major energy contributions have been presented before, and combined together the explicit expression of the atomistic spin Hamiltonian of a simulated system therefore can be given as follows:

$$\begin{aligned}\mathcal{H} &= \mathcal{H}_{\text{exchange}} + \mathcal{H}_{\text{anisotropy}} + \mathcal{H}_{\text{field}} \\ &= -\frac{1}{2}\sum_{i,j} J_{ij}\,(\hat{\mathbf{S}}_i \cdot \hat{\mathbf{S}}_j) - k_u \sum_i (\hat{\mathbf{S}}_i \cdot \hat{\mathbf{e}})^2 - \sum_i \mu_i (\hat{\mathbf{S}}_i \cdot \mathbf{B}),\end{aligned} \tag{2.34}$$

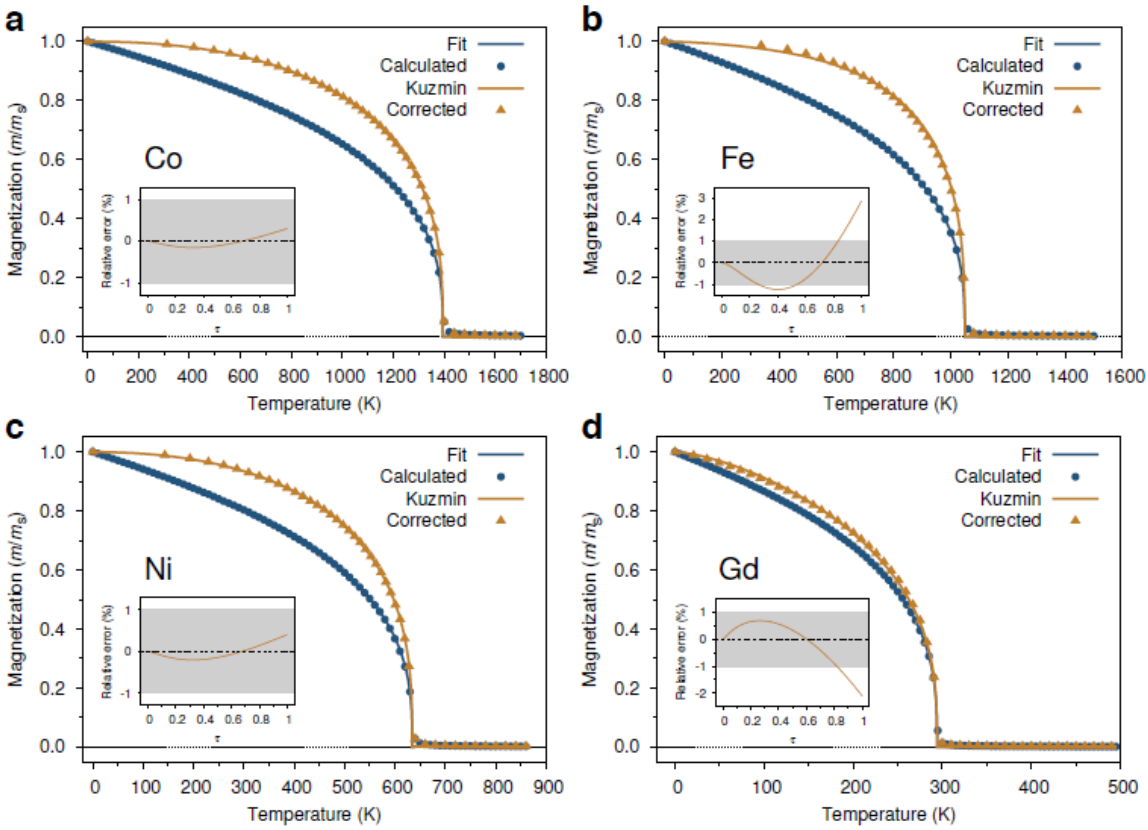

Fig. 2.5 Temperature-dependent magnetisation for the elemental ferromagnets (a) Co, (b) Fe, (c) Ni, and (d) Gd. Blue curves plot the non-scaled mangetisation and gold curves the rescaled temperatures fitted by Eq. (2.32) with very good agreement with experimental data. Insets are plots of relative error of the rescaled magnetisation compared to the fit. Source: excerpt from [58].

where J_{ij} is the exchange energy strength between $\hat{\mathbf{S}}_i$ and $\hat{\mathbf{S}}_j$ the unit vector of local spins at site i and j, k_u is the uniaxial anisotropy constant having an easy direction $\hat{\mathbf{e}}$, μ_i the atomic spin moment, and $\mathbf{B}$ the externally applied magnetic field. As previously discussed, it can be noted that out of the three major energy contributions, the exchange and anisotropy terms are intrinsic to the specific material. The last term, the external field contribution, accounts for the effect of external magnetic forces, such as from other magnetic materials in the vicinity or from an electric current. The relation between the exchange energy strength J_{ij} and the Curie temperature T_C of the material is then given by Garanin [61] as:

$$J_{ij} = \frac{3k_B T_c}{\varepsilon z}, \tag{2.35}$$

where k_B is the Boltzmann constant, z the number of nearest-neighbour interactions in a unit-cell, and ε the correction factor relating to the coordination-dependent spin wave stiffness. Both z and ε are uniquely determined for each crystal structure [39, 61].

2.4 The Mean-field theory

The main focus of this Thesis is a comprehensive study of finite-size and surface effects on magnetic properties of nanograins for potential application in Heat-assisted Magnetic Recording media. Previous literature, especially those by Penny et al.[62] have shown that a mean-field approach is particularly valuable for the investigation of finite size effects, including lattice types and particle shapes. Therefore, in order to support the interpretation atomistic model calculations which will be presented and analysed in later Chapters, a lattice site resolved Mean-field model is employed which can be outlined as follows [63]. Consider the standard Heisenberg spin Hamiltonian including an applied field $\mathbf{B}$ and here using for convenience the same spin notation as in [63]:

$$\mathcal{H} = -\frac{1}{2}J\sum_{\langle ij\rangle}\hat{\mathbf{s}}_i\cdot\hat{\mathbf{s}}_j - \mu\sum_i \hat{\mathbf{s}}_i\cdot\mathbf{B}, \tag{2.36}$$

where the individual terms represent the ferromagnetic exchange interaction energy and the Zeeman energy. The symbol $\langle\cdot\rangle$ in the first sum implies that only the nearest neighbour spin pairs are summed over. The spin variables are unit vectors $\hat{\mathbf{s}}_i = \mu_i/\mu$, $i = 1,\ldots,N$, where μ_i is the magnetic moment associated with the spin i and $\mu = |\mu_i|$ is its magnitude.

A conventional way to derive the mean-field approximation is to express the spin variables in Eq. (2.36) as $\hat{\mathbf{s}}_i = \tilde{\mathbf{m}}_i + \delta\hat{\mathbf{s}}_i$, where $\tilde{\mathbf{m}}_i$ and $\delta\hat{\mathbf{s}}_i$ are respectively the thermally averaged and fluctuating parts of the spin variable $\hat{\mathbf{s}}_i$. Neglect the fluctuations $\delta\hat{\mathbf{s}}_i$ beyond the first order and rewrite Eq. (2.36) as:

$$\mathcal{H}_{\mathrm{mf}} = \frac{1}{2}J\sum_{\langle ij\rangle}\tilde{\mathbf{m}}_i\cdot\tilde{\mathbf{m}}_j - \sum_i \hat{\mathbf{s}}_i\cdot\left(J\sum_{j\in i}\tilde{\mathbf{m}}_j + \mu\mathbf{B}\right), \tag{2.37}$$

where the expression in the parentheses:

$$\mu\mathbf{B}_i^{\mathrm{e}} = J\sum_{j\in i}\tilde{\mathbf{m}}_j + \mu\mathbf{B} \tag{2.38}$$

is the effective field acting on the mean-field spin moment $\tilde{\mathbf{m}}_i$ due to its neighbours j and is derived as the variational derivative with respect to $\tilde{\mathbf{m}}_i$. The notation $j \in i$ means the summation

is carried out over all interacting neighbours j of the spin i. The mean-field spin moment $\tilde{\mathbf{m}}_i$ can be evaluated from Eq. (2.37) using the canonical statistical mechanics:

$$\tilde{\mathbf{m}}_i = \frac{\mathrm{Tr}_{\mathbf{s}_i} \mathbf{s}_i \exp\left(-\beta \mathcal{H}_{\mathrm{mf}}\right)}{\mathrm{Tr}_{\mathbf{s}_i} \exp\left(-\beta \mathcal{H}_{\mathrm{mf}}\right)}. \tag{2.39}$$

Note that since $\tilde{\mathbf{m}}$ is no longer a unit vector, Eq. (2.37) no longer conforms with the usual Heisenberg definition of the exchange. However, if we transform to unit vectors by multiplying through by $\tilde{\mathbf{m}}^2/\tilde{\mathbf{m}}^2$ we are left with the prefactor of the summation term in Eq. (2.37) as $J\tilde{\mathbf{m}}^2$ which represents the temperature dependence of the effective exchange in the mean-field sense [64]. Upon considering that stable moment configurations are aligned with their effective fields, i.e. $\tilde{\mathbf{m}}_i \parallel \tilde{\mathbf{B}}_i^{\mathrm{e}}$, allows expressing $\tilde{\mathbf{m}}_i$ as:

$$\tilde{\mathbf{m}}_i = \mathcal{L}\left(\beta\mu|\tilde{\mathbf{B}}_i^{\mathrm{e}}|\right) \frac{\tilde{\mathbf{B}}_i^{\mathrm{e}}}{|\tilde{\mathbf{B}}_i^{\mathrm{e}}|}. \tag{2.40}$$

Here $\mathcal{L}(x) = \coth x - x^{-1}$ is the Langevin function, and $\beta = (k_B T)^{-1}$ with k_B being the Boltzmann constant and T the temperature. Eq. (2.38) and Eq. (2.40) represent a set of coupled nonlinear algebraic equations which can be solved iteratively in a straightforward way, as discussed elsewhere [63].

Furthermore, it can be shown that the relation between the exchange energy constant J_{ij} and the Curie temperature T_C can be derived from the Mean-field theory. First rewrite Eq. (2.40) in the scalar form as:

$$m_i = \mathcal{L}(\beta\mu B_i^e), \tag{2.41}$$

where as before:

$$\mu B_i^e = J\sum_{j\in i} m_j + \mu B. \tag{2.42}$$

Assume zero applied field $B = 0$ and express $m_i = \mathcal{L}(\beta J \sum_j m_j)$. Imagine the system is in a paramagnetic state, then $m_i = 0$ for all i in the mean-field model. When the freezing occurs at T_C then all spins will freeze co-linearly (because there is no DMI which would prefer non-collinear spin alignment, for example), and get some finite moment $m_i = m$. Rewrite the equation as $m = \mathcal{L}(\beta J z m)$, where z is the spin-coordination number, i.e. $\sum_j m = zm$. Differentiate this rewritten function of m with respect to the field B (imagine an increment to small non-zero field), by chain-rule it gives:

$$\frac{dm}{dB} = \mathcal{L}'(\beta J z m).\beta J z.\frac{dm}{dB}, \tag{2.43}$$

where $\mathcal{L}'(\beta Jzm)$ is the derivative of the Langevin function with respect to the field B, which expanded to the first order yields the factor of $1/3$. Insert this factor in and express:

$$\frac{dm}{dB}\left(1-\frac{1}{3}\beta Jz\right)=0. \tag{2.44}$$

This has a non-trivial solution if $3^{-1}\beta Jz=1$, which upon arranging gives:

$$T_C=\frac{zJ}{3k_B}. \tag{2.45}$$

This relation is the same as in Eq. (2.35) before, apart from the omission of the correction factor ε which in the mean-field model $\varepsilon=1$. Thus, Eq. (2.35) derived from a spin Hamiltonian model is essentially a mean-field formula with a correction factor ε, which is needed in order to "fit" the mean-field solution ansatz to non-mean-field models.

2.5 The 2-ion anisotropy model for Iron Platinum FePt

The material of interest in this Thesis, Iron Platimum in the $L1_0$-phase ($L1_0$-FePt) has a exceptionally large magneto-crystalline uniaxial anisotropy that persists even at extremely small grain sizes [65]. Interestingly, the majority of this large anisotropy does not come from the local, single-site anisotropy of the constituent Fe and Pt atoms, but rather from a so-called 2-ion anisotropy component. This 2-ion anisotropy component stems from the strong spin-orbit coupling between the 3d-element Fe and 5d-element Pt interlayers along the (001) lattice direction in which the Fe moments can be viewed to be mediated by the Pt moments. This strong Fe-Pt spin-orbit coupling produces, in addition to the local single-site anisotropies, a much more dominating 2-ion anisotropy component [66].

A study by Mryasov in 2005 [67] presented a comprehensive investigation on how this dominant 2-ion anisotropy in $L1_0$-FePt can be incorporated into the spin Hamiltonian model. Ab-inito calculations [67] show that the Fe moment is well localised whilst the Pt moment is delocalised. This presents a problem to the fundamental assumption of the Heisenberg model which requires that moments are localised to the atomic sites. However, Fe moments are also found to polarise the Pt moments, so numerically the effective delocalised Pt moments $\mathbf{m}_v$ can be reasonably well approximated by the exchange field from surrounding Fe moments by:

$$\mathbf{m}_v=\frac{\chi_v}{M_v^0}\sum_i J_{iv}\mathbf{S}_i, \tag{2.46}$$

where χ_v is the local Pt susceptibility, M_v^0 the local Pt saturation magnetisation, J_{iv} the Fe-Pt exchange interaction strength, and $\mathbf{S}_i$ the Fe moment. An explicit spin Hamiltonian consisting of the localised Fe moments and delocalised Pt moments can be written as:

$$\mathcal{H} = -\frac{1}{2}\sum_{i,j} J_{ij}\mathbf{S}_i \cdot \mathbf{S}_j - \sum_i k_{Fe}(\mathbf{S}_i^z)^2 - \sum_v \mathcal{I}\mathbf{m}_v^2 - \sum_v k_{Pt}\mathbf{m}_v^2, \tag{2.47}$$

where J_{ij} is the Fe-Pt exchange interaction strength and $\mathcal{I}$ the Pt-Pt exchange interaction strength, $k_{Fe} = -0.097$ meV is the Fe anisotropy constant and $k_{Pt} = 1.427$ meV the Pt anisotropy constant. Note that the superscript z refers to the z-component of the spins. By using the Fe moments-dependence expression for Pt moments in Eq. (2.46), this explicit Hamiltonian in Eq. (2.47) can be reduced to an effective form that depends only on the Fe degrees of freedom:

$$\mathcal{H} = -\frac{1}{2}\sum_{i,j} \mathcal{J}_{ij}\mathbf{S}_i \cdot \mathbf{S}_j - d_i^z(\mathbf{S}_i^z)^2 - \frac{1}{2}\sum_{i,j} d_{ij}^z \mathbf{S}_i^z \cdot \mathbf{S}_j^z, \tag{2.48}$$

where $\mathcal{J}_{ij}$ is the effective Fe-Fe exchange interaction strength, d_i the effective single-ion anisotropy constant, and d_{ij} the effective 2-ion anisotropy constant. The explicit expressions for $\mathcal{J}_{ij}$, d_i, and d_{ij} are given as:

$$\mathcal{J}_{ij} = J_{ij} + \mathcal{I}\left(\frac{\chi_v}{M_v^0}\right)^2 \sum_v J_{iv}J_{jv}, \tag{2.49}$$

$$d_i^z = k_{Fe} + k_{Pt}\left(\frac{\chi_v}{M_v^0}\right)^2 \sum_v J_{iv}^2, \tag{2.50}$$

$$d_{ij}^z = k_{Pt}\left(\frac{\chi_v}{M_v^0}\right)^2 \sum_v J_{iv}J_{jv}. \tag{2.51}$$

The expression of this reduced effective spin Hamiltonian of FePt induces a 2-ion anisotropy which depends on the effective Fe-Pt exchange interaction, J_{iv}, therefore clearly illustrating the effect of the delocalised moments on the overall magnetic properties of FePt. Since the single-ion anisotropy is approximatedly 10 times smaller than the 2-ion anisotropy, it is the 2-ion anisotropy which forms the dominant part of the overall macroscopic anisotropy constant. Additionally, since in Eq. (2.48) both the 2-ion anisotropy term and the exchange interaction term share a similar mathematical form, in VAMPIRE simulations it is possible, and in fact more computationally efficient, to combine the 2-ion anisotropy component into the exchange interaction to form an anisotropic exchange. Using this approach, the vector components of the effective Hamiltonian can be expressed explicitly, by decomposing and collecting the terms in

Eq. (2.48) in respective spin component, as:

$$\mathcal{H}_x = -\frac{1}{2}\sum_{i,j}\mathcal{J}_{ij}\mathbf{S}_i^x \cdot \mathbf{S}_j^x, \tag{2.52}$$

$$\mathcal{H}_y = -\frac{1}{2}\sum_{i,j}\mathcal{J}_{ij}\mathbf{S}_i^y \cdot \mathbf{S}_j^y, \tag{2.53}$$

$$\mathcal{H}_z = -d_i^z(\mathbf{S}_i^z)^2 - \frac{1}{2}\sum_{i,j}\left(\mathcal{J}_{ij} + d_{ij}^z\right)\mathbf{S}_i^z \cdot \mathbf{S}_j^z. \tag{2.54}$$

Note that the z-component of the Hamiltonian $\mathcal{H}_z$ now includes both the single-ion anisotropy contribution expressed through the d_i^z term, and the 2-ion anisotropy contribution incorporated into the exchange interaction via the $\left(\mathcal{J}_{ij} + d_{ij}^z\right)$ term. This is the mechanism by which the 2-ion anisotropy of $L1_0$-FePt is implemented in VAMPIRE simulations in later Chapters 4 and 5.

2.6 Summary

In this Chapter an overview of different magnetic modelling frameworks has been presented with a brief summary and context of the Micromagnetics and Ab-inito methods as well as a deeper focus on fundamental principles of Atomistic modelling. A description of the implementation of the Atomistic modelling method into the VAMPIRE simulation code has also been given, which will lay the foundation for computational studies presented in subsequent Chapters. Finally, the key concepts of the Mean-field theory as well as of the 2-ion anisotropy model in $L1_0$-FePt have also been outlined, both of which will become essential to enable the analysis and discussions of simulation results in Chapters 4 and 5.

3

The influence of finite-size effects on the Curie temperature of $L1_0$-FePt

We employ an atomistic model using a nearest-neighbour Heisenberg Hamiltonian exchange to study computationally the dependence of the Curie temperature of $L1_0$-FePt on finite-size and surface effects in Heat-assisted Magnetic Recording (HAMR) media. We demonstrate the existence of a size threshold at 3.5nm below which the impact of finite-size effects start to permeate into the centre of the grains and contribute to the reduction of the Curie temperature. We find a correlation between the Curie temperature and the percentage of atomistic bonds lost on the surface as a function of grain size, which can be extended to apply to not only $L1_0$-FePt but also generic magnetic systems of any crystal structure. The investigation gives insight into finite-size effects which, because the inevitable grain size dispersion leads to an irreducible contribution to a dispersion of the Curie temperature, has been predicted to be a serious limitation of HAMR.

3.1 Motivation

Heat-assisted Magnetic Recording (HAMR) is emerging as the next-generation approach for magnetic recording [68, 69]. The HAMR writing head first applies an intense, highly localised heat spot for a very short time to a recording medium to heat it up to or beyond its Curie temperature (T_C), then writes the data inductively after which cooling to ambient temperature restores thermal stability. The functioning of HAMR therefore requires the writing medium to be made of a magnetic material with high anisotropy and relatively low Curie temperature. Iron Platinum in the $L1_0$ phase satisfies these two requirements, and thus has been receiving extensive studies [15, 16] for potential HAMR applications in which $L1_0$-FePt can function either as a single layer or as part of a composite multi-layer recording medium [15, 70–74].

In room condition, bulk-alloy FePt exists in the $A1$ phase in which the constituent Fe and Pt atoms are randomly distributed, thus resulting in a very low uniaxial anisotropy. However, at temperatures in the typical range of a HAMR write-head, FePt can undergo a transition to the $L1_0$ phase [75]. $L1_0$-FePt has a face-centre cubic (fcc) crystal structure - sketched in Fig. 3.1 - which comprises of alternating layers of 3d-element Fe and 5d-element Pt atoms along the (001) direction and therefore is highly chemically ordered. As discussed before in Chapter 2, in the $L1_0$ phase the Fe spins polarise the Pt spins and the strong spin-orbit coupling between the Fe and Pt inter-layers produces, in addition to the much weaker local single-site anisotropies, an exceptionally large 2-ion anisotropy component [66] necessary for the thermal stability of data storage [67, 16]. A detailed mathematical formalism of this dominant 2-ion anisotropy component of $L1_0$-FePt has already been given in Chapter 2, and an investigation of the 2-ion anisotropy of FePt will be the focus of the next Chapter 4.

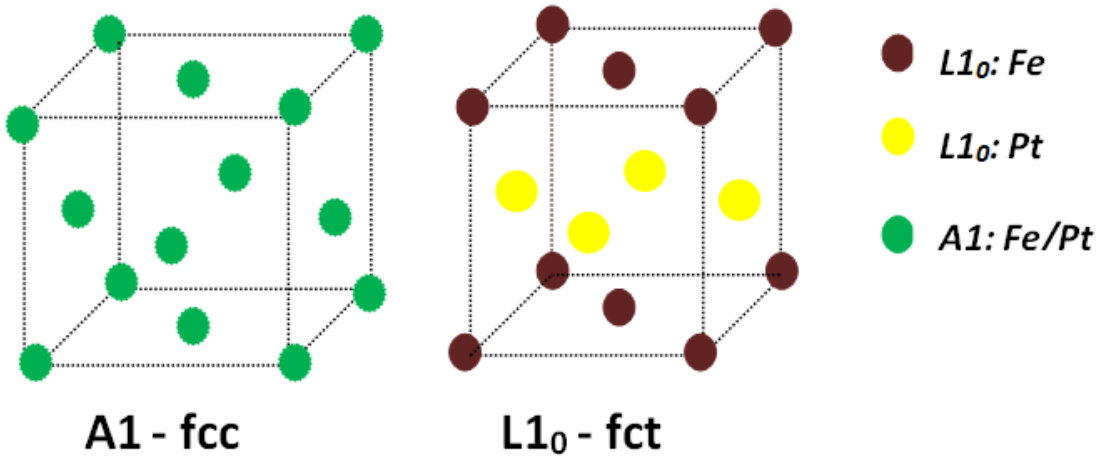

Fig. 3.1 Crystal structures of FePt: (left) disordered $A1$-fcc bulk-alloy $Fe_{0.5}Pt_{0.5}$ at room temperature; (right) ordered $L1_0$-fct at HAMR temperature

Simulations by Li and Zhu [76, 77] have shown that the dispersion of T_C is a serious limitation for the ultimate storage density achievable for HAMR. Consequently, a crucial aspect for successful HAMR media is controlling the Curie temperature dispersion of the recording medium. However, the exact Curie temperature of $L1_0$-FePt has yet to be established; rather, it has been reported to fall between 650K and 780K under various treatments and measurements [78]. Also, the Curie temperature of $L1_0$-FePt was shown to exhibit a strong dependence on grain size [79, 80]. Consequently, in a recording medium using $L1_0$-FePt the grain size distribution, which always exists, would inevitably lead to an irreducible dispersion

of the Curie temperature σ_{T_c} which potentially limits the recording density. Therefore, it poses an important question to determine not only the precise dependence of the Curie temperature distribution in $L1_0$-FePt grains on finite size effects but also the governing mechanisms behind it.

This Chapter presents a computational investigation of the impact of finite-size effects in $L1_0$-FePt grains using a nearest-neighbour Heisenberg Hamiltonian atomistic Spin model in which short-range exchange interactions are assumed to dominate. Although the exchange interactions in FePt are long-ranged, Waters et al. [78] have shown that the critical exponent of FePt conforms to the three dimensional Heisenberg universality class. The starting point is the consideration of thermal fluctuations, which can modify T_C and even shift the ground state solutions to induce changes in magnetic phases. To verify this, it is necessary to look at how the free energy changes as a function of system size. Generally, the free energy will have a functional part reflecting the surface effects due to reduced coordination number, but there will be another term that will correspond to renormalisation of state energies resulting from fluctuations [81]. Which part is more important will depend on the system and the size. A correlation is then hypothesised between the Curie temperature distribution of $L1_0$-FePt and the percentage of atomistic bond loss on the surface of the grains as a function of grain size, which allows to separate the surface and fluctuation contributions to the finite-size effects. It is found that this hypothesised correlation could be extended to encompass the role of crystal structure, which suggests it is not restricted to $L1_0$-FePt specifically but is universally applicable for any generic magnetic system.

3.2 Simulation methods and settings

3.2.1 Theoretical background

The underlying theories that will be employed for the analyses of calculations in this Chapter include the Atomistic Spin Hamiltonian and the Mean-field models - both of which have been discussed in details in Chapter 2. Therefore, in order to aid the flow of arguments, only a few key points will need to be briefly recapped. Numerical simulations are carried out by the VAMPIRE atomistic code [52, 39] version 4 using an Atomistic Spin model in which the energy of a magnetic system is described by the general Hamiltonian $\mathcal{H}$ as the sum of energy contributions. All simulations in this Chapter are carried out under the absence of an externally applied magnetic field $\mathbf{B}$, so the field - or Zeeman - component in the general Spin Hamiltonian can be omitted, which leaves the Spin Hamiltonian with just the exchange interaction $\mathcal{H}_{\text{exchange}}$

and the anisotropy $\mathcal{H}_{\text{anisotropy}}$ terms:

$$\mathcal{H} = -\frac{1}{2}\sum_{i,j} J_{ij}\,(\hat{\mathbf{S}}_i \cdot \hat{\mathbf{S}}_j) - k_u \sum_i (\hat{\mathbf{S}}_i \cdot \hat{\mathbf{e}})^2, \tag{3.1}$$

where J_{ij} is the exchange energy strength between $\hat{\mathbf{S}}_i$ and $\hat{\mathbf{S}}_j$ - the unit vector of local spin at site i and j respectively, and k_u the uniaxial anisotropy constant having an easy direction along $\hat{\mathbf{e}}$. Furthermore, because finite-size effects are being investigated, the exchange interaction does not have to be fully long-range - i.e. inclusive of all neighbouring atoms in the simulated system. Instead, the exchange interaction can reasonably be limited to a short-range exchange involving nearest-neighbours only in order to account for broken and missing atomistic bonds on the surface. Therefore, the exchange energy strength J_{ij} between each neighbouring pair of spins $\hat{\mathbf{S}}_i$ and $\hat{\mathbf{S}}_j$ can be reduced to a constant - with its notation simplified to just J and pulled out of the summation. Consequently, Eq. (3.1) can be simplified to:

$$\mathcal{H} = -\frac{1}{2}\,J\sum_{i,j} (\hat{\mathbf{S}}_i \cdot \hat{\mathbf{S}}_j) - k_u \sum_i (\hat{\mathbf{S}}_i \cdot \hat{\mathbf{e}})^2. \tag{3.2}$$

The Hamiltonian of $L1_0$-FePt derived from first principle calculations includes anisotropy contributions from both constituent Fe and Pt atoms. However, as previously discussed in Chapter 2, Mryasov et al. [67] using Density Functional Theory in the constrained local-spin-density approximation has theoretically demonstrated that the Pt moments can be well approximated by the neighbouring Fe moments, and therefore the Hamiltonian of $L1_0$-FePt could be rewritten to be dependent on the Fe degree of freedom only. Consequently, the energy of a $L1_0$-FePt system will depend only on the lattice arrangement of the Fe atoms. This conclusion leads to two crucial implications. First, following Mryasov et al.'s treatment, the original fct lattice structure of $L1_0$-FePt in Fig. 3.1 can be reduced to an effective tetragonal simple-cubic (sc) lattice structure by removing all Pt atoms in the middle-layers [60, 82] - an illustration of this method is sketched in Fig. 3.2. The remaining Fe-only system with modified lattice properties - a configuration henceforth will be referred to as the modified-sc FePt - is still equivalent to the original fct lattice $L1_0$-FePt, whilst in the meantime because of having fewer atoms can help to reduce computational time significantly. The second implication is that because only the Fe lattice arrangement will matter, it will be possible to extend the investigation of finite-size effects to encompass the role of different crystal structures beyond the strictly fct $L1_0$-FePt. In particular, two artificial configurations of FePt are added to the investigation: a face-centre cubic (fcc) and a body-centre cubic (bcc) lattice systems both of which, for comparison purpose, are made to share the same magnetic attributes of the original fct $L1_0$-FePt system.

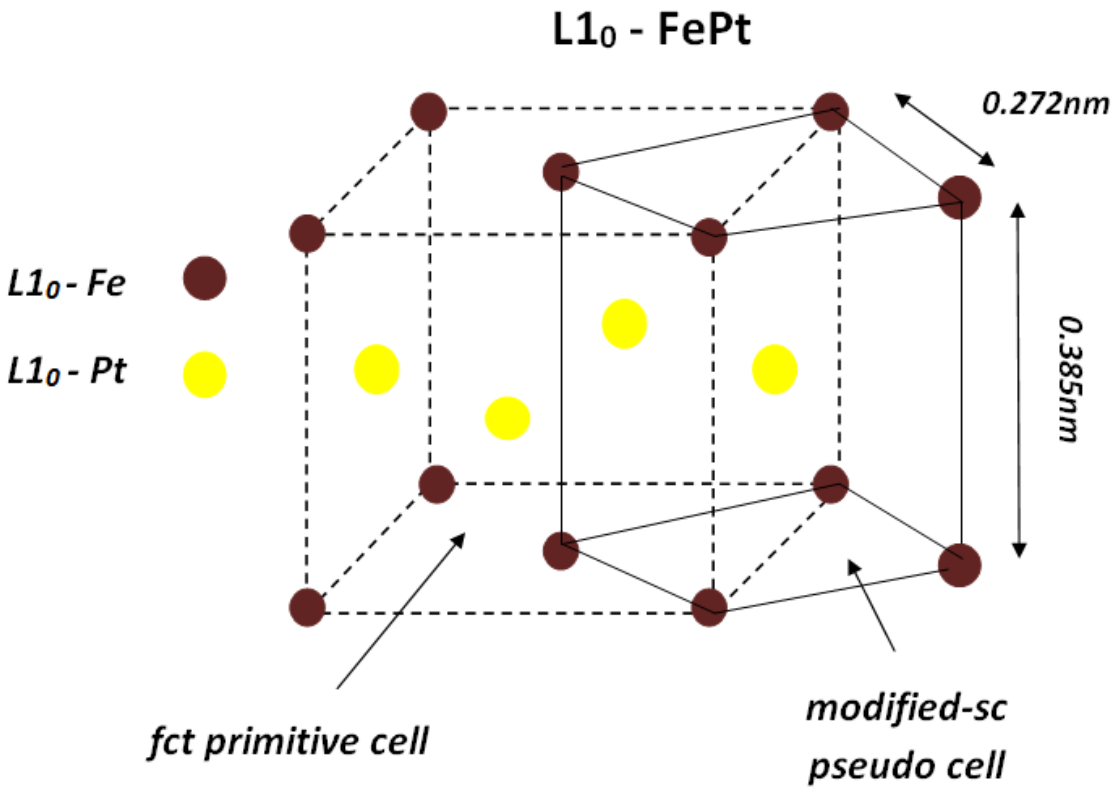

Fig. 3.2 An illustration of the creation of an equivalent modified-sc pseudo-cell from the original fct primitive cell of $L1_0$-FePt.

3.2.2 Construction of FePt grains

FePt grains are constructed in parallelepiped shape. As aforementioned, in order to account for the effects of crystal structure, three lattice configurations of FePt grains are simulated: a modified-sc lattice FePt configuration which is equivalent to the original fct $L1_0$-FePt, an artificial fcc lattice FePt and an artificial bcc lattice FePt configuration both of which are assigned similar magnetic attributes of the original fct $L1_0$-FePt. An illustrative cross-sectional view of the three simulated lattice structures are shown in Fig. 3.3. The unit cells of all three configurations following the experimentally derived data for bulk powder are set to have dimensions of $x_0 = y_0 = 2.72$ Å and $z_0 = 3.85$ Å [83, 84].

The height for each grain along the z-dimension is fixed at the nominal value of 10 nm. The base of each grain on the xy-dimension is square-shaped and can be varied in a nominal range from 1 nm to 10 nm in 0.5 nm increment. It has to be noted that the adjective "nominal" prefixing the grain sizes is used for a convenient reference only, whilst the "exact" grain sizes are slightly different. Since finite-size effects are the focus of investigation, it is undesirable to

Fig. 3.3 Sampled cross-sectional views of the 3 simulated lattice structures: (left) modified-sc lattice FePt equivalent to the original fct $L1_0$-FePt, (middle) an artificial fcc lattice FePt, and (right) an artificial bcc lattice FePt. Visualisation using Jmol [85].

create grains with incomplete unit cells - i.e. with dangling atoms - on the surface. Therefore, a grain having a specific nominal base size $\widetilde{D}$ is made to comprise of an integer number of unit cells N in each xy-dimension of the base so that the exact base size $D = N \times x_0$, which numerically is a multiplier of x_0, must be as close to $\widetilde{D}$ as possible. The nominal grain sizes $\widetilde{D}$, each with the corresponding number of unit cells included in the grain base N and the exact grain size D, are presented in Table 3.1.

$\widetilde{D}$ (nm)	1.0	1.5	2.0	2.5	3.0	3.5	4.0	4.5	5.0	5.5
N	4	6	7	9	11	13	15	17	18	20
D (nm)	1.088	1.632	1.904	2.448	2.992	3.536	4.080	4.624	4.896	5.440
$\widetilde{D}$ (nm)	6.0	6.5	7.0	7.5	8.0	8.5	9.0	9.5	10.0	
N	22	24	26	28	29	31	33	35	37	
D (nm)	5.984	6.528	7.072	7.616	7.888	8.432	8.976	9.520	10.064	

Table 3.1 The nominal and exact grain sizes of simulated FePt grains

3.2.3 Determining the Curie temperature

VAMPIRE simulations use a Metropolis Monte-Carlo integrator - which follows the mechanism already described in Chapter 2 - to compute the value of normalised mean magnetisation length $\langle M/M_s \rangle$ and the longitudinal susceptibility χ at each temperature T of the simulated

temperature range. Combining all values of $\langle M/M_s \rangle$ and χ obtained from across the entire simulated temperature range will produce the normalised magnetisation distribution $\langle M/M_s \rangle(T)$ and longitudinal susceptibility distribution $\chi(T)$ as functions of temperature - an example is given in Fig. 3.4(a) and Fig. 3.4(b) respectively. It can be noted that a small magnetic "tail", where the magnetisation does not drop down to zero, can be seen above the Curie temperature in the $\langle M/M_s \rangle$ plot in Fig. 3.4(a). This visible trailing tail is essentially a finite size effect due to a finite probability of a spontaneous instantaneous magnetisation in small-sized of systems. Applying the temperature-rescaling method in Chapter 2 with appropriate parameteres can help to "rectify" this trailing tail, thus modifying the $\langle M/M_s \rangle$ curve to be more aligning with experimental data.

There are then 2 commonly used methods to determine the Curie temperature. First, the Curie temperature can be found by fitting the scaling law given by Eq. (2.31) in Chapter 2 directly into $\langle M/M_s \rangle(T)$. The precision of this method, however, depends heavily on the behaviour of magnetisation - in particular where the magnetisation curve drops to zero - and therefore is only accurate at fitting into bulk material of large-sized grains where the correlation length has diverged. Alternatively, a more accurate method involves finding the peak of the susceptibility distribution $\chi(T)$. The justification of the susceptibility-peak method is given through the Curie-Weiss law which links the Curie temperature T_C with the susceptibility χ of a ferromagnet in the paramagnetic region above the Curie temperature [23] by:

$$\chi = \frac{C}{T - T_C}, \tag{3.3}$$

where C is the Curie constant. Therefore, as T approaches T_C, χ attains the maximum value which is the peak of the susceptibility distribution. This means the $\chi(T)$ curve always exhibits a well-define peak at the location of the Curie temperature, thus making the susceptibility-peak method applicable for even smaller-sized grains. An illustration of how the susceptibility-peak method is implemented is given in Fig. 3.4(b).

However, the method of finding the peak of susceptibility distribution will return an accurate value of Curie temperature only if the susceptibility distribution obtained from VAMPIRE simulation is sufficiently smooth, especially around the Curie temperature region, thus displaying a well-defined peak. This condition can only be met when the simulated system has been properly equilibrated before calculations are performed on it. In VAMPIRE, there are two simulation parameters which control this process: the Monte-Carlo (MC) Equilibration step and the MC Total time step. The system is first let to equilibrate for a number of MC steps specified by the Equilibration step, during which VAMPIRE tries to "equilibrate" the magnetisation. Once the equilibration has been completed, the system is "reset" and started afresh during which cal-

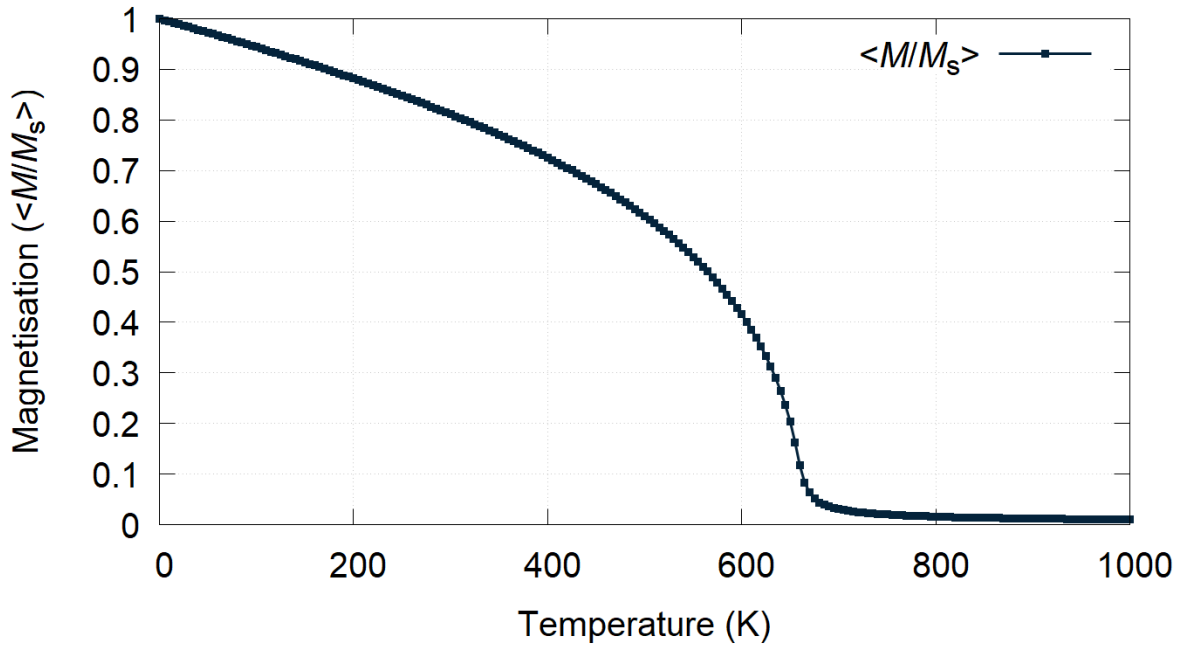

(a)

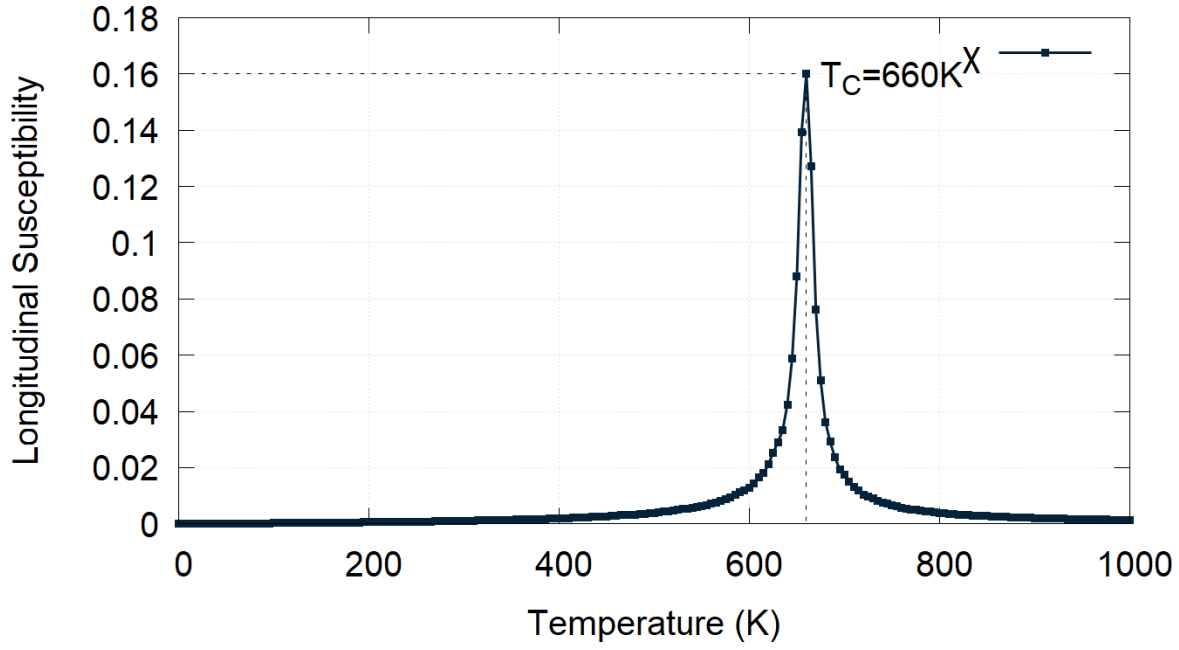

(b)

Fig. 3.4 A sample of the temperature-dependent distribution of the (a) Magnetisation $\langle M/M_s \rangle$, and (b) Longitudinal susceptibility $\chi(T)$ obtained from VAMPIRE atomistic simulation for a sampled sc-lattice grain of $9 \times 9 \times 10$ nm size. Note that the Longitudinal susceptibility plot exhibits a sharp, well-defined peak necessary for an accurate locating of the Curie temperature.

culations will be performed using the final value of magnetisation retained at the end of the equilibration period. The total number of MC steps carried out during the entire simulation, inlcuding the equilibration period, is equal to the MC Total time steps.

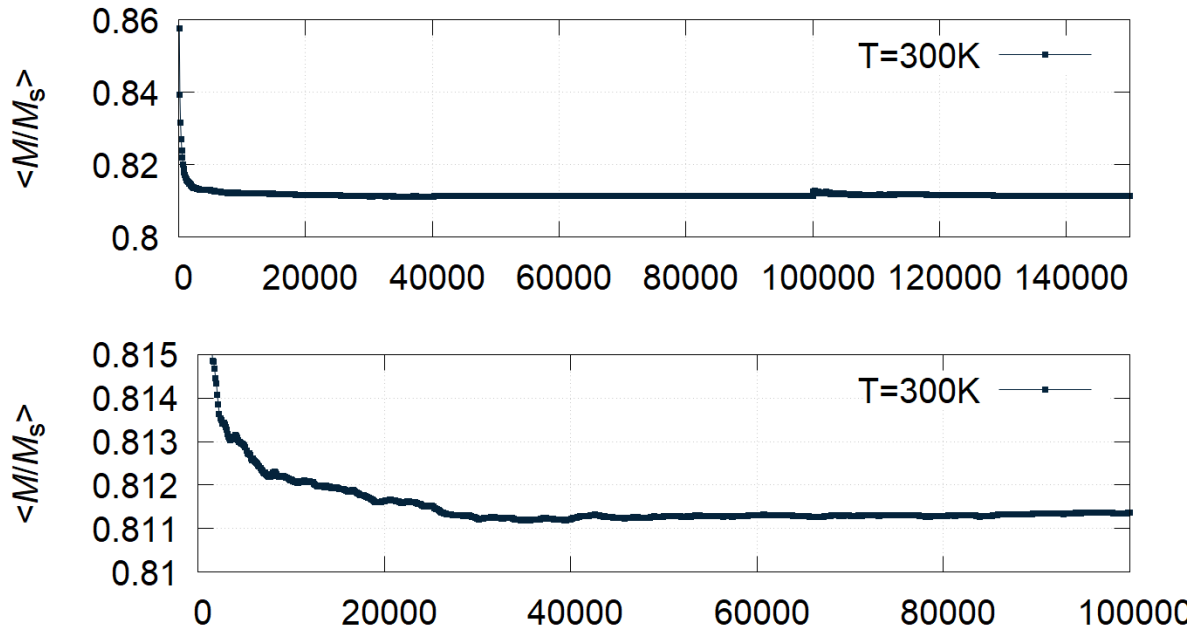

Fig. 3.5 The effects on Monte-Carlo Equilibration and Total time steps on the equilibrating of the simulated system. Sample is taken at 300 K with an Equilibration step set to 100000 - where an upward strike is visible at 100000 MC step indicating that the equilibration process has been completed and the system is to be reset after which calculations will take place. The bottom plot is a close-up view during the equilibration period of the upper $\langle M/M_s \rangle$ plot. It can be seen in the $\langle M/M_s \rangle$ plot that the magnetisation curve does not converge to a stable value until almost 50000 MC steps, meaning that the Equilibration step must be set to at least 50000.

An illustration for the impact of these MC steps on simulation can be seen in Fig. 3.5. In this example the MC Equilibration step is set to 100000, which is observable via the visible upward strike in the $\langle M/M_s \rangle(T)$ plot at the 100000^{th} MC step. During the equilibration period, as can be seen, the numerical value of $\langle M/M_s \rangle$, after being initiated from starting conditions, are converging to a stable value at around the 50000^{th} MC step. This means the preset value of the Equilibration step of 100000 is in fact a bit higher than necessary, so for computational optimisation it can be lower to around but not less than 50000. At the reset point at the 100000^{th} MC step, the aforementioned converging, stable value of $\langle M/M_s \rangle$ is recorded and simulation restarts. Since the equilibration process has been done properly, the stable value of $\langle M/M_s \rangle(T)$ is carried onto later calculations until final output. Otherwise, if the equilibration process has not been done properly, $\langle M/M_s \rangle$ will not converge before system reset. Consequently,

subsequent calculations using an non-equilibrated value of $\langle M/M_s \rangle$ will lead to a heavily noised $\chi(T)$ curve without a well-defined peak. The Equilibration and Total time steps can only be determined via trial and error, and they are found to be dependent on grain sizes. The grain size-dependent MC parameters appropriate for the simulations in this Chapter are given in Table 3.2. Simulations can be repeated many times to compute statistical values. In order to re-create varying initial conditions as in real experiments, each time the simulation runs, a randomly generated number can be assigned to it which represents a unique sets of initial conditions.

Grain Size (nm)	Equilibration step	Total time step
1.0 - 1.5	5×10^7	2.5×10^8
2.0 - 2.5	10^7	10^8
3.0 - 5.5	10^6	10^7
≥ 6.0	10^5	10^6

Table 3.2 VAMPIRE MC parameters

3.2.4 Simulation parameters of FePt

The effects of crystal lattices are investigated with the Curie temperature in each case first preset to a theoretically calculated critical temperature of 660K [86] in the largest-sized grain of 10nm nominal base size. Recall the linear relation between the Curie temperature T_C and the exchange energy strength J [61]:

$$J = \frac{3k_B T_C}{\varepsilon z}, \tag{3.4}$$

where k_B is the Boltzmann constant, z the number of nearest-neighbour interactions in a unit cell, and ε the correction factor relating to the coordination-dependent spin wave stiffness. It has already been shown in Chapter 2 that Eq. (3.4) can also be derived from the Mean-field theory. Both z and ε are uniquely determined for each crystal structure [39, 61]. For a specific lattice structure, J is determined computationally by interpolation to give a consistent $T_C = 660K$ - a reference value derived from previous studies [86, 87] - for each lattice structure using Eq. (3.4) as shown in Fig. 3.6. Numerical values of J, z, and ε are given in Table 3.3. Other parameters representing magnetic properties of FePt which are shared by all three simulated crystal configurations include the atomic spin moment μ_S and uniaxial anisotropy constant k_u, which followed from Strungaru et al. [60] are fixed at $\mu_S = 3.23\mu_B$ (with $\mu_B = 9.274 \times 10^{-24}$

J/T being the Bohr magneton constant) and $k_u = 2.63 \times 10^{-22}$ J/atom respectively. Sampled VAMPIRE input and material files for the simulations of this Chapter are given in Appendix B.

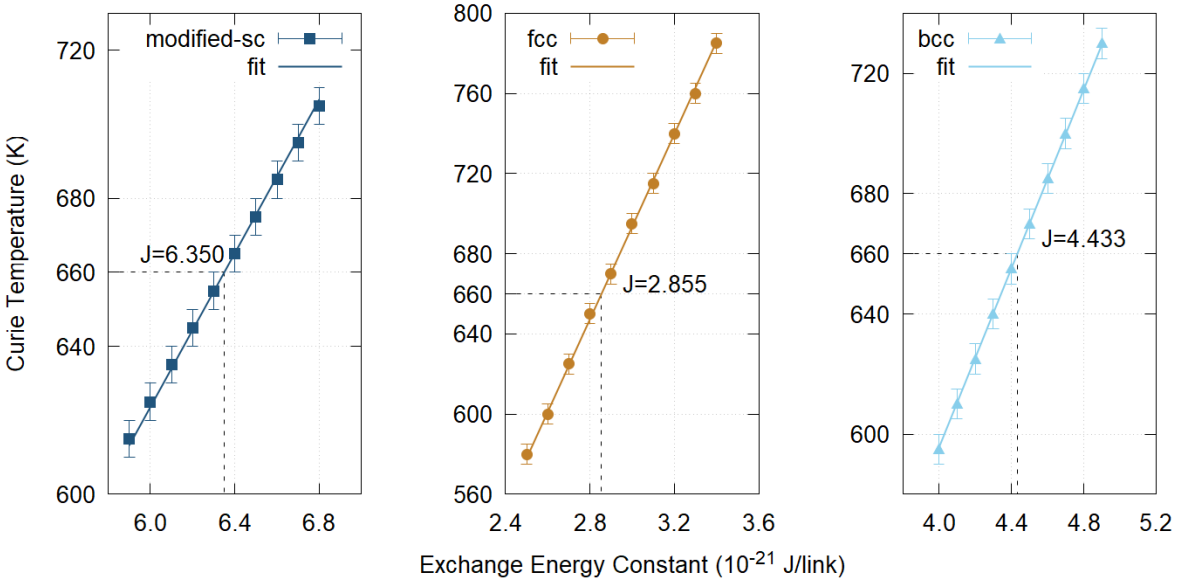

Fig. 3.6 Determination of the exchange energy constant for simulated FePt grains with different crystal structures. As expected there is a linear dependence of Curie temperature on exchange strength. By interpolation the exchange energy is determined to give a consistent $T_C = 660$K for each lattice structure.

Configuration	z	ε	J (Joule per link)
modified-sc	6	0.719	$(6.303 \pm 0.004) \times 10^{-21}$
fcc	12	0.790	$(2.866 \pm 0.002) \times 10^{-21}$
bcc	8	0.766	$(4.430 \pm 0.002) \times 10^{-21}$

Table 3.3 Unit cell parameters for each simulated configuration of FePt.

3.3 Results and discussion

3.3.1 The Curie temperature variation with grain size

The Curie temperatures of each grain size D for each simulated lattice structure are given in Table A.1 of Appendix A and plotted in Fig. 3.7. The Curie temperature variation with grain

size T_C(D) generally conforms to the well known Finite-size Scaling Law (FSSL) which is given by [79, 88]:

$$T_C(D) = T_C(bulk)(1 - x_0 D^{-1/\nu}), \tag{3.5}$$

where D is the characteristic grain size, ν is a critical exponent, and x_0 is a fitting parameter on the order of the lattice spacing. Eq. (3.5) is applied to determine x_0 and ν as well as the bulk Curie temperature T_C(bulk). The percentage Curie temperature decrease, $\Delta T_C(D)$, can then be defined as the percentage difference between the Curie temperature at each grain size $T_C(D)$ and the bulk Curie temperature $T_C(bulk)$ obtained from the FSSL fit:

$$\Delta T_C(D) = \frac{T_C(bulk) - T_C(D)}{T_C(bulk)} = x_0 D^{-1/\nu}, \tag{3.6}$$

which shares the similar mathematical form as seen in previous literature [89, 90]. It is important to remark that the fits to the FSSL often give values of ν which differ: in apparent contradiction to the nature of ν as a universal exponent. As a result, ν^{-1} is often replaced by a so-called shift exponent λ which may or may not agree with ν depending on the various system properties [89]. A possible mechanism for the deviation from the critical exponent will be proposed later.

The investigation of finite-size dependence of the Curie temperature is carried out using the atomistic model outlined earlier. Fig. 3.7 demonstrates that the dependence of the Curie temperature on size T_C(D) fits well to the (FSSL) [88] given in Eq. (3.5), consistent with previous experimental data [78, 80, 87]. Numerical values extracted from the FSSL for the fitting parameter x_0, the critical exponent ν, and the bulk Curie temperature T_C(bulk) are given in Table 3.4. It can be noted that, although the FSSL fits the data well for all grain sizes investigated, the values found for ν do not agree exactly with the expected value of 0.7 for the Heisenberg model [80, 91] - a deviation which has been seen and discussed before in literature [92, 93]. This deviation of ν can be explained by considering how the FSSL is obtained in the first place. the FSSL follows from the correlation scaling relation $\xi \sim (1 - T/T_c)^{-\nu}$ [43, 89] which leads to the scaling law in Eq. (3.6). Note that this scaling relation for ξ is valid only for bulk systems, leading, in fitting to experimental data, to the empirical replacement of the exponent ν, which is universal, by the so-called shift exponent λ which is non-universal and may include corrections to scaling [80]. Here, a possibility has to be given considerations that, for small grain sizes, the correlation length becomes dependent on the characteristic size as a result of the rescaling of system energies resulting from the fluctuations.

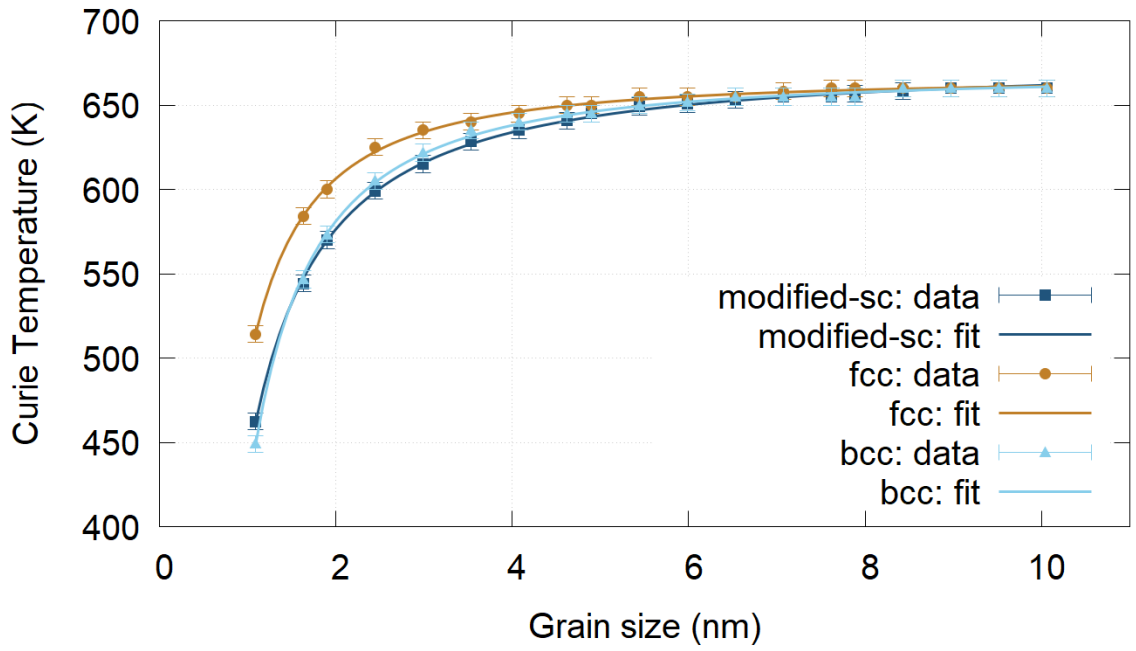

Fig. 3.7 The dependence of Curie temperature on grain size fits well with the FSSL for all 3 simulated crystal structures. The T_C increases sharply at smallest grain sizes and converges to the bulk value from around 8 nm. In section 3.3.4, an analytic model is described to discuss the comparison between the three simulated cases.

Configuration	$T_C(bulk)$	x_0	ν
modified-sc	674.2 ± 1.1	0.352 ± 0.002	0.783 ± 0.014
fcc	666.2 ± 0.7	0.260 ± 0.002	0.651 ± 0.013
bcc	668.3 ± 0.9	0.375 ± 0.003	0.656 ± 0.011

Table 3.4 FSSL fitting parameters for each simulated configuration of FePt.

3.3.2 The layer-resolved magnetisation profiles

To provide further insight, it is necessary to look into a detailed analysis of the layer-resolved magnetisation profiles which are obtained by averaging the spins in each layer. Examples of the magnetisation profile at 550 K in the x-direction along the grain depth are given in Fig. 3.8 for different grain sizes of the fcc lattice grains. In larger grains (9.0 nm) surface disorder (low magnetisation) causing the drop in magnetisation is seen to penetrate only a few layers inside the grain. On the contrary, in smaller grains where the total number of layers is reduced to the 10-12 range, surface effects begin to dominate. Calculations show that in smaller-sized grains the loss of order causing the decrease of Curie temperature across surface layers propagates

into the centre of the grain: an effect potentially responsible for causing a larger overall drop in the Curie temperature of the whole grain.

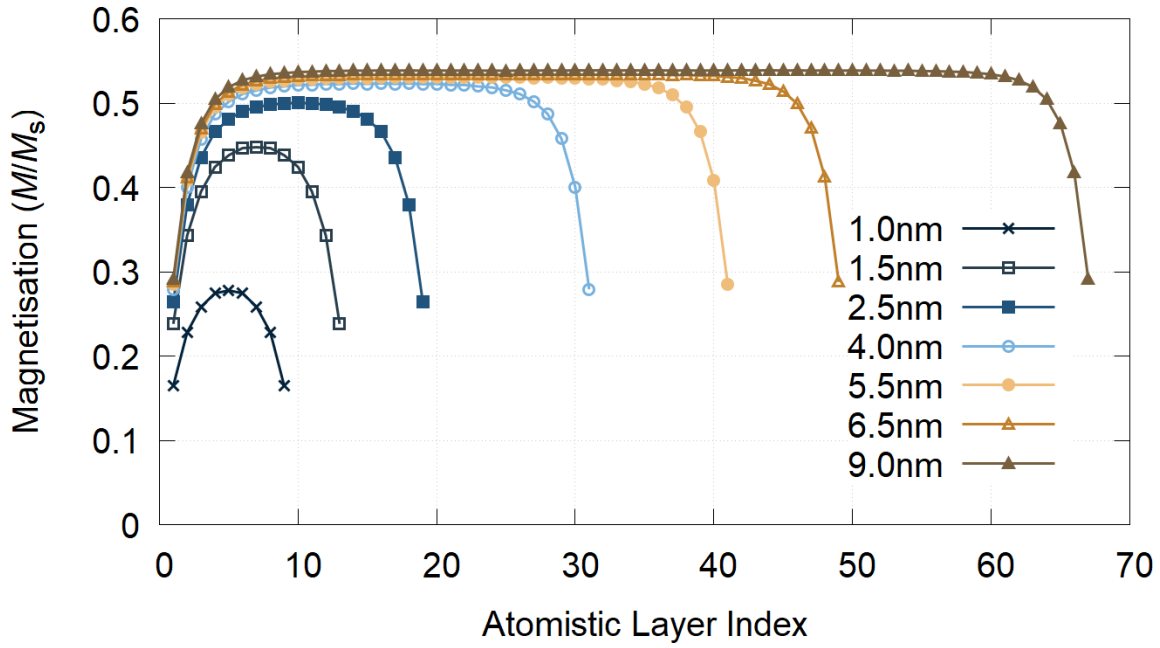

Fig. 3.8 The layer-resolved magnetisation profile for fcc lattice grains of selected sizes at 550 K showing that in smaller grains (fewer atomistic layers) the magnetisation drop on the surface contributes more to the overall loss of the grain magnetisation.

Similar patterns can be seen for the modified-sc and bcc lattices. The magnetisation profile for modified-sc lattice is shown in Fig. 3.9 and bcc-FePt lattice in Fig. 3.10. As expected the behaviour is similar to the fcc lattice results in Fig. 3.8, although the penetration depth is clearly smaller for the modified-sc lattice. It can be seen that there is a periodic behaviour for the bcc lattice, which is a physical effect arising from atoms having different numbers of nearest neighbors. Interestingly this persists to elevated temperatures in the bulk of the grain albeit somewhat reduced at the grain boundaries, suggesting that the disorder propagates inward from the surfaces.

The magnetisation profiles obtained from atomistic simulations are next compared with calculations from the Mean-field model, a mathematical description of which has been given in Chapter 2. The mean-field data for FePt grains used in this comparison are obtained in collaboration with Dr. Sergiu Ruta. Two regimes of behaviour for small and large grain sizes can be seen in Fig. 3.11. Particularly, the larger grains retain order in the central region, with increasing loss of order close to the surface, whereas for the smaller grains the disorder essentially penetrates the whole grain. The Mean-field model gives good qualitative agreement with the atomistic model calculations, supporting the localisation of the disorder close to the

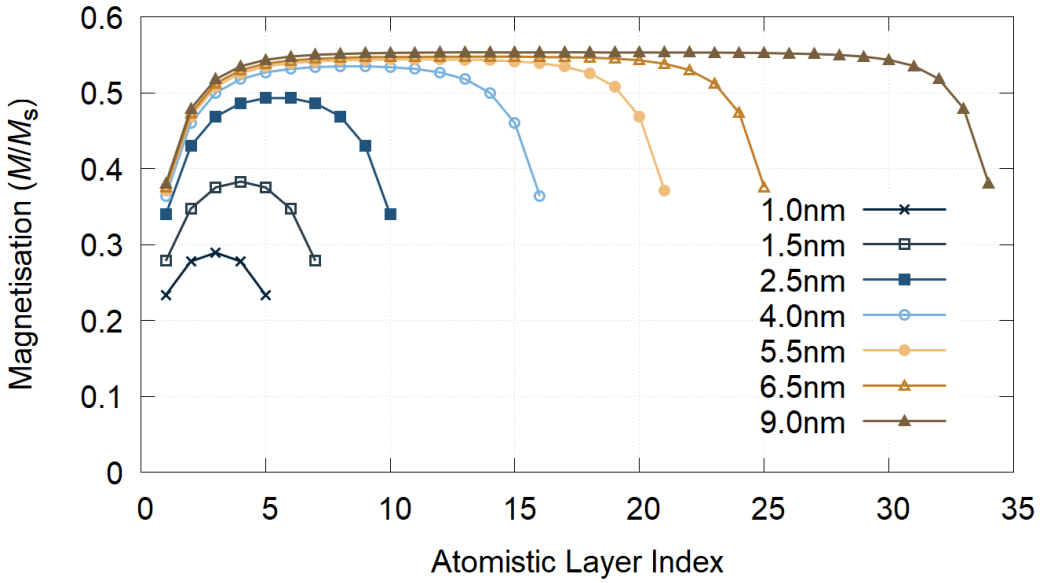

Fig. 3.9 The layer-resolved magnetisation profile for modified-sc lattice grains - equivalent of the original fct $L1_0$-FePt - of selected sizes at 550 K showing that in smaller grains (fewer atomistic layers) the magnetisation drop on the surface contributes more to the overall loss of the grain magnetisation.

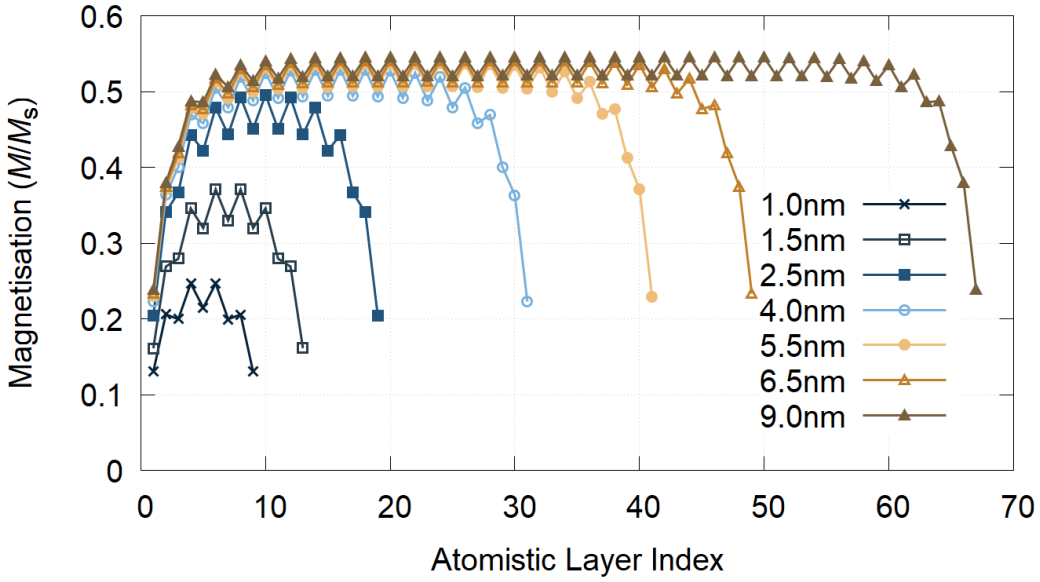

Fig. 3.10 The layer-resolved magnetisation profile for bcc lattice grains of selected sizes at 550 K showing that in smaller grains (fewer atomistic layers) the magnetisation drop on the surface contributes more to the overall loss of the grain magnetisation. The bcc structure exhibits a periodic behaviour which is a physical effect due to atoms having different numbers of nearest neighbours.

surface of the grain. Based on these results, a simple analysis designed to characterise the penetration depth of the disordered region can be formalised and presented in section 3.3.4.

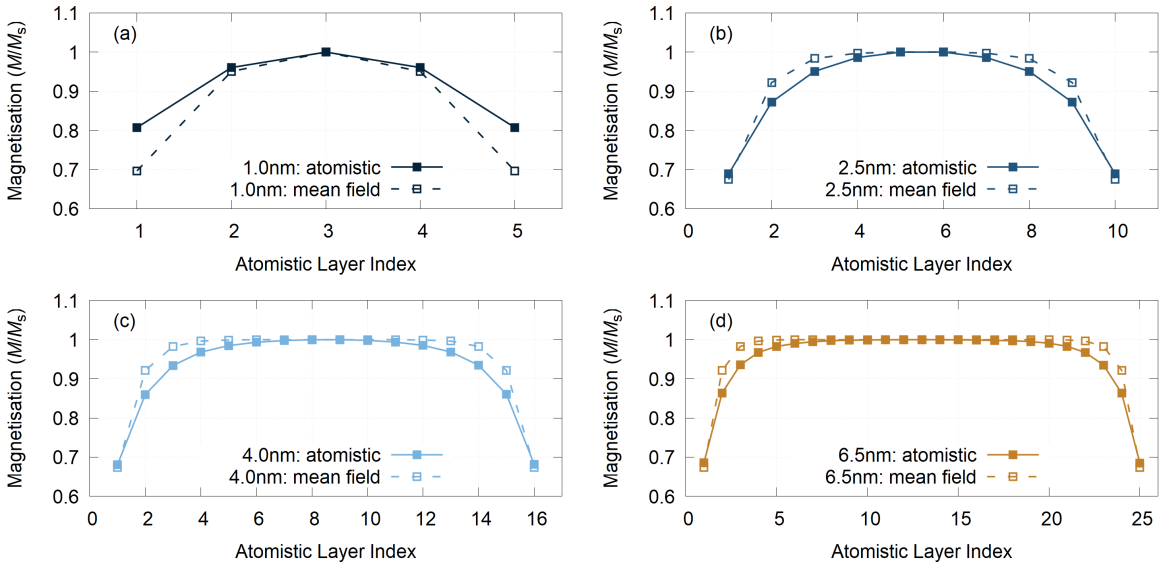

Fig. 3.11 Comparison between atomistic and semi-analytic mean field calculation of layer-resolved magnetisation at 550 K for grains of size (a) 1.0 nm, (b) 2.5 nm, (c) 4.0 nm, and (d) 6.5 nm shows a good agreement between 2 models, with a slight disparity occurring at the outermost surface layers of each grain.

3.3.3 The cross-sectional magnetisation profiles

The evolution of the cross-sectional magnetisation profile for the fcc lattice grains at 550 K in Fig. 3.12 shows a decrease of magnetisation across the grain surface which appears to be more pronounced in smaller grains, consistent with the data shown before in Fig. 3.8. These patterns suggest that surface disorder might be an important contribution to the rapid drop in T_C at smaller sizes as captured before by the FSSL: the hypothesis is that the propagation of the surface disorder into the grain has an effect on the correlation length such that $\xi = \xi(D)$. This hypothesis is consistent with the effects of a term corresponding to renormalisation of state energies which results from fluctuations [81]. Hence, the correlation length is also modified. However, in Fig. 3.8 it is clear that the renormalisation of the state energies decreases with distance away from the surface. Additionally, similar behaviours are again observed for modified-sc and bbc lattice grains - as illustrated in Fig. 3.13 and Fig. 3.14 respectively. This observation suggests that the decrease of magnetisation across the grain surface is not a lattice-specific but rather a universal property.

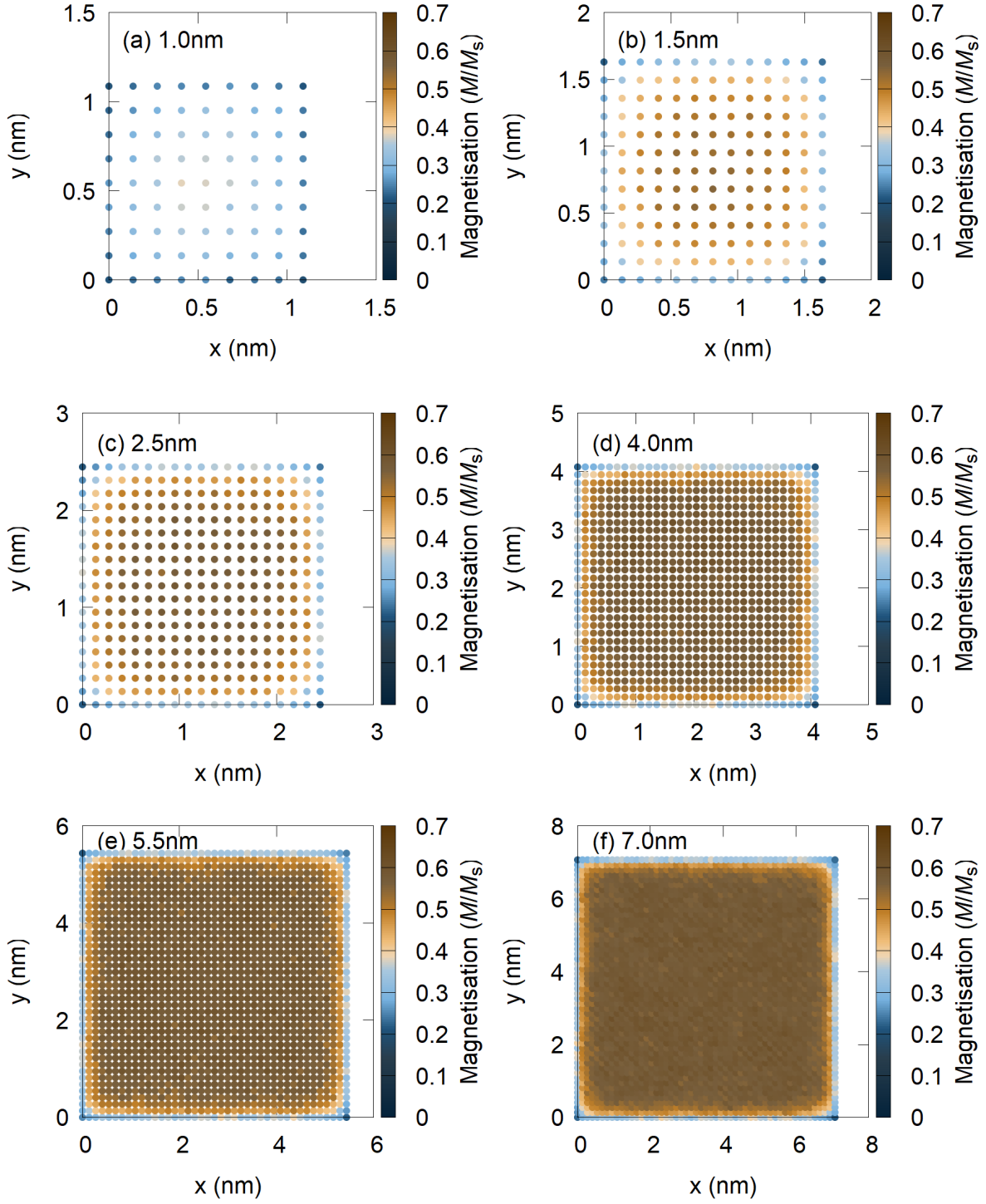

Fig. 3.12 Evolution of the cross-sectional magnetisation profile for fcc lattice grains at 550 K of (a) 1.0 nm, (b) 1.5 nm, (c) 2.5 nm, (d) 4.0 nm, (e) 5.5 nm, and (f) 7.0 nm in size. The grain magnetisation can be seen to be decreasing across the grain surface.

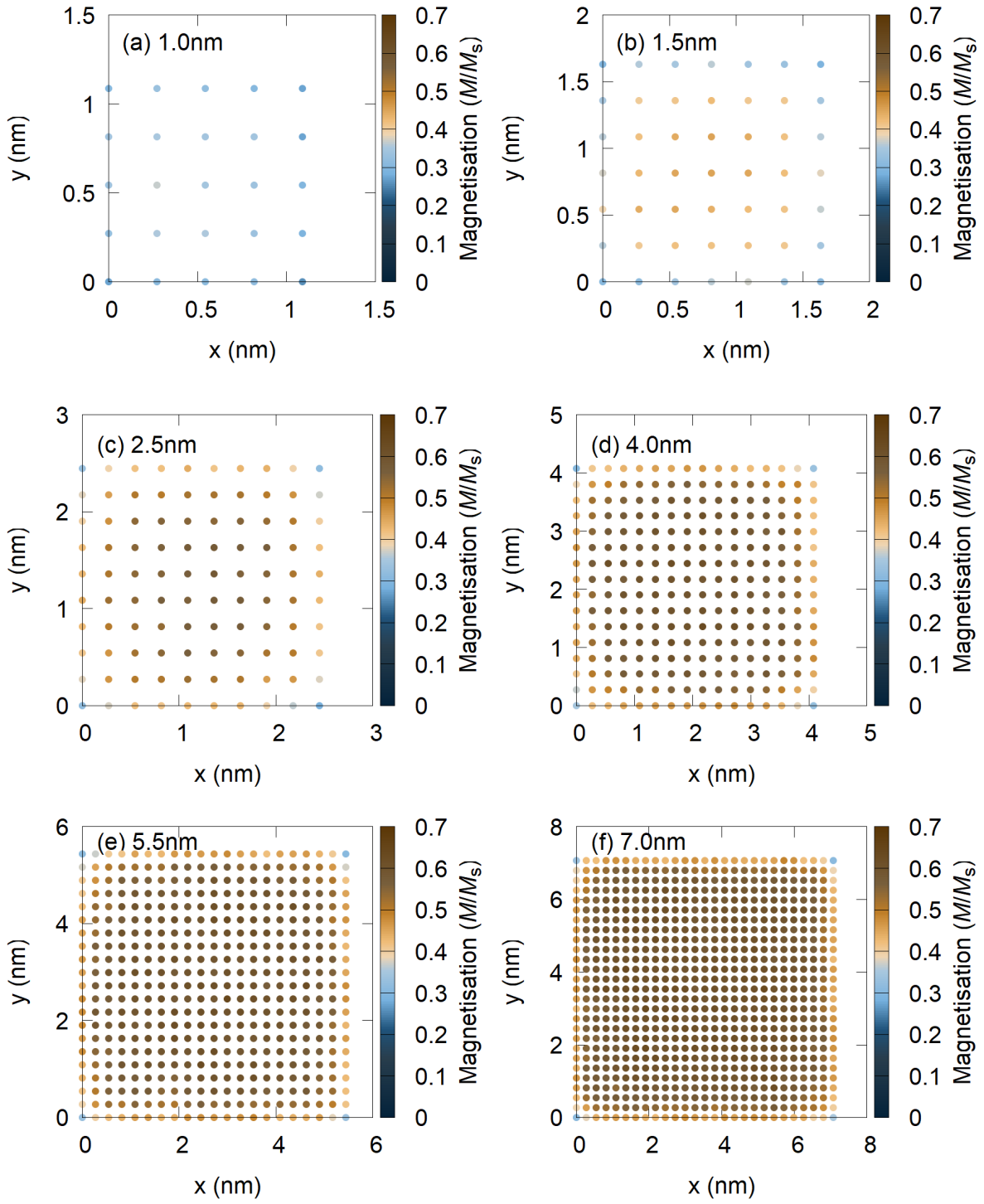

Fig. 3.13 Evolution of the cross-sectional magnetisation profile for modified-sc lattice grains at 550 K of (a) 1.0 nm, (b) 1.5 nm, (c) 2.5 nm, (d) 4.0 nm, (e) 5.5 nm, and (f) 7.0 nm in size. The grain magnetisation can be seen to be decreasing across the grain surface.

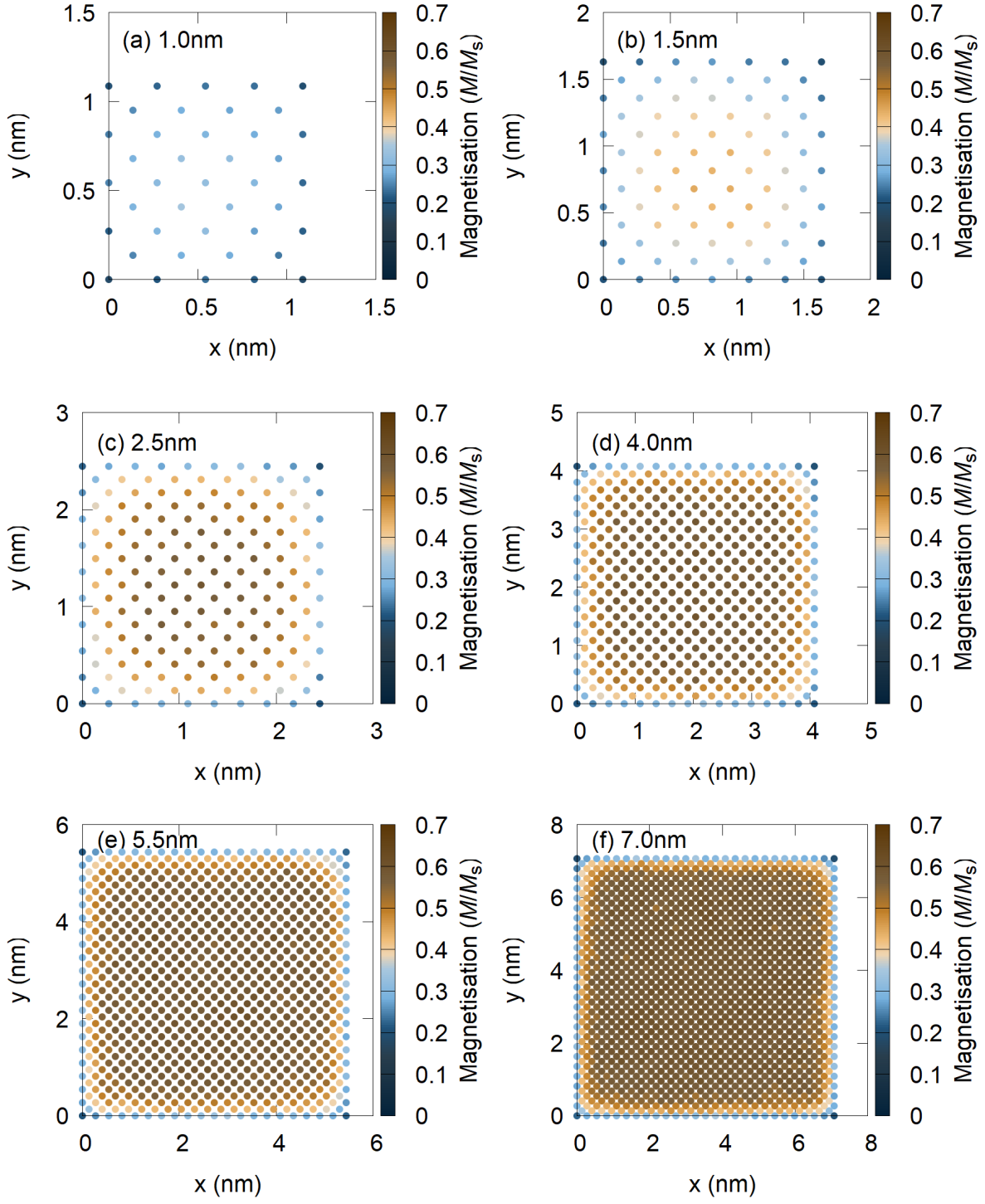

Fig. 3.14 Evolution of the cross-sectional magnetisation profile for bcc lattice grains at 550 K of (a) 1.0 nm, (b) 1.5 nm, (c) 2.5 nm, (d) 4.0 nm, (e) 5.5 nm, and (f) 7.0 nm in size. The grain magnetisation can be seen to be decreasing across the grain surface.

3.3.4 The correlation between the magnetisation loss and the atomistic bond loss

A simple analysis model reflecting both contributions - which are the loss of magnetisation on the grain surface and the propagation of surface disorder into the grain bulk - can be formalised as follows. The starting point is to assume that the Curie temperature reduction ΔT_c, relative to the bulk value $T_C(bulk)$, is entirely due to the loss of coordination at the surface. Thus ΔT_c is assumed proportional to the number of surface bonds broken. As a first approximation it can be assumed that the number of broken bonds n_{bb} is proportional to the surface area of the grains. Then, it is straightforward to show that the fractional increase in broken bonds Δn_{bb} - which is related to the number of total bonds in the bulk - as a function of the grain height h and dimater (width) D is given by:

$$\Delta n_{bb} = B(h^{-1} + 2D^{-1}), \tag{3.7}$$

where h is the height of the grain and B is a constant depending on the crystal structure and is determined by fitting to the numerical calculation. The exact amount of atomistic bonds lost in a particular grain can be calculated computationally: for each atom in the grain, the number of nearest-neighbours can be counted and thus the number of missing nearest-neighbours can be determined, noting that a "fully bonded" atom should have 6 nearest-neighbours in a modified-sc lattice system, 12 in a fcc lattice system, and 8 in a bcc lattice system. If the grain were a part of the bulk, a grain made up of N atoms in modified-sc, fcc, and bcc lattice structure would have an "ideal" total of $6N$, $12N$, and $8N$ nearest-neighbour atomistic bonds respectively. Then, summing up over all atoms and comparing with the "ideal" number of total bonds for each lattice type will yield the fractional or percentage bond loss Δn_{bb}. The percentage bond loss and Curie temperature reduction for each simulated lattice structure are tabulated in Table A.2 of Appendix A.

Eq. (3.7) is found to give a good fit to the numerical results for all crystal structures studied, as shown in the inset of Fig. 3.15(a). In terms of fitting to the values of ΔT_c, it is found that the assumption of $\Delta T_c \propto \Delta n_{bb}$ with Δn_{bb} following the expression in Eq. (3.7) is valid only for large diameters, indicating that in this regime the decrease in T_C is essentially a surface effect. As is shown later, for small diameter, the surface disorder propagates into the center of the grain leading to a more rapid decrease of T_C, albeit one which is captured by the finite size scaling law. This effect can be quantified this by fitting to a modified function:

$$\Delta T_c = \alpha \exp(-D/D_p) + \beta \Delta n_{bb}, \tag{3.8}$$

where α and β are fitting constants and D_p is a characteristic distance associated with the propagation of the disorder into the center of the grain. As shown in Fig. 3.15(a), Eq. (3.8) fits well to the numerical calculation for all lattice structures. Values of the fitting constants are given in Table 3.5. A propagation term ΔT_{cp} which represents the propagation of surface disorder into the grain can then be defined as follows:

$$\Delta T_{cp} = \Delta T_c - \beta \Delta n_{bb}. \tag{3.9}$$

Eq. (3.9), along with the numerical calculation, is shown in Fig. 3.15(b). It can be seen that, for diameter $D \lessapprox 3.5$ nm there is an exponential increase in ΔT_c as the diameter decreases. Note that the cut-off value of 3.5nm can be interpreted as the penetration depth of surface magnetisation loss into the grain bulk. It is approximately 4 times D_p, which from Eq. (3.8) corresponds to approximately 1.8% of T_C drop. Clearly the lost surface bonds drive the loss of magnetic order and the reduction in T_C. However, it is important to note the role played by the renormalisation of the state energies arising from the fluctuations originating at the surface. This gives rise to the progressive decrease of the loss of magnetisation when moving toward the centre of the grain. For small grain sizes $D \leq 3.5nm$, the decrease in magnetic order due to state energy renormalisation cannot be stabilised by a fully-ordered central core. In this regime the state energy renormalisation becomes the dominant factor leading to a rapid collapse of the magnetisation and T_C. Hovorka et al. [80] have given an expression relating the dispersion of T_C directly to the dispersion of diameter. This suggests that for decreasing grain sizes, such as expected for the evolution of Heat-assisted Magnetic Recording, any grain size variation would give an increasingly large distribution of T_C which could become a limiting factor for the technology. On the other hand, numerous designs for Heat-assisted Magnetic Recording media involve coupling layers with high anisotropy and low T_C with layers of lower anisotropy and higher T_C. It is likely, from the analysis presented here, that for strongly exchange coupled layers the surface disorder and hence reduction of the T_C of the high anisotropy could be somewhat mediated by the proximity effect of a higher T_C layer. Finally, the existence and the lattice-type dependence of a threshold size above which the percentage Curie temperature drop ΔT_C rapidly becomes negligible - as illustrated in Fig. 3.15 - are again in good agreement with mean-field calculations seen in previous literature [62].

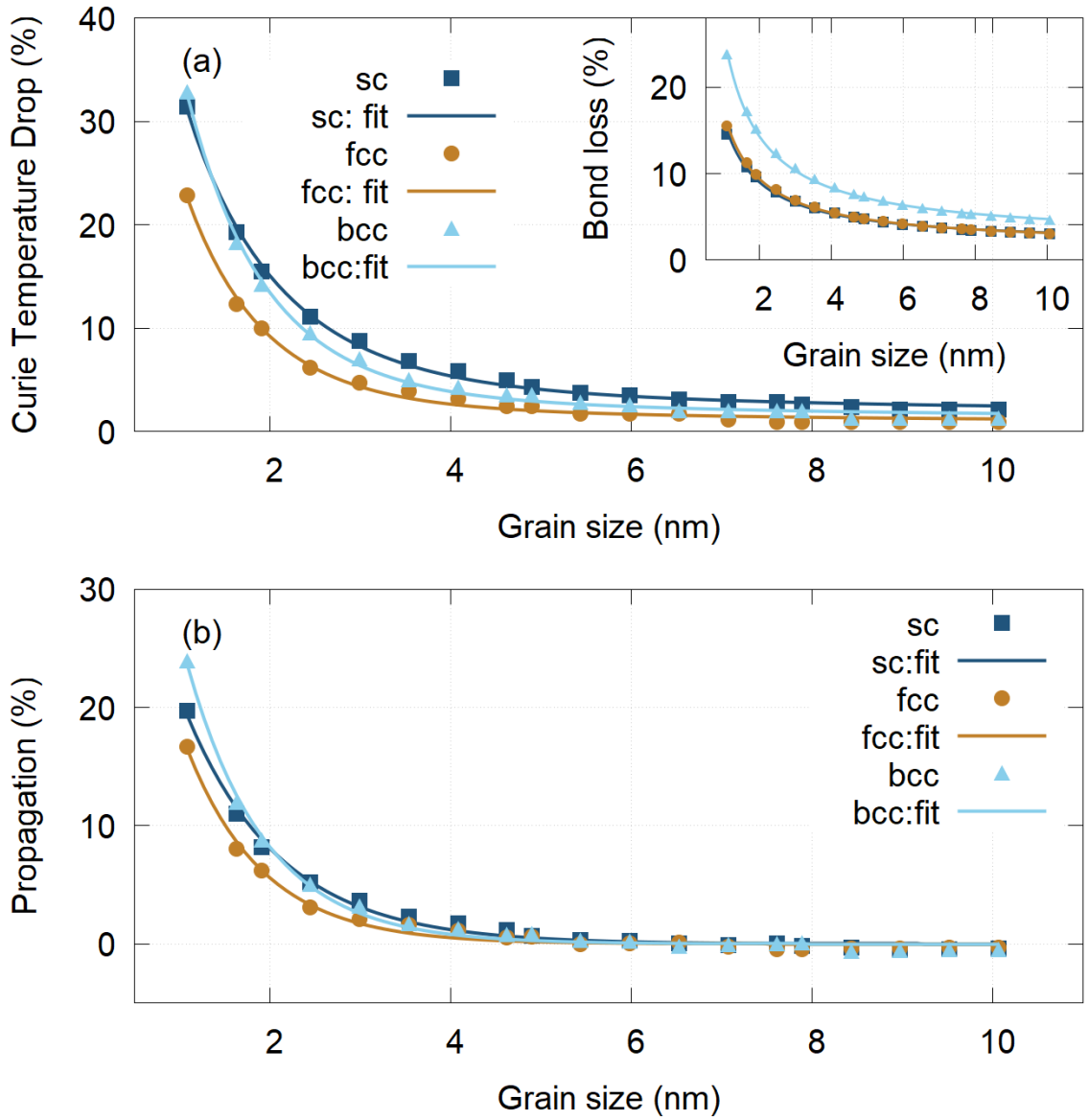

Fig. 3.15 Correlation between the Curie temperature drop and atomistic bond loss for each lattice structure: (a) ΔT_C(D) following from the FSSL fit to Eq. (3.8) and the inset showing the percentage bond loss; (b) The surface-effects propagation term ΔT_{cp} showing a cut-off value at $D \approx 3.5$ nm for all 3 studied lattice structures.

3.4 Further remarks

On a final remark, it is worth to mention that during this research there was an intention to include, in addition to the study of the role of crystal structure already presented, an investigation of the role of grain shape on finite-size effects. In fact, different grain shapes including

Configuration	α	D_p (nm)	β
modified-sc	54.4 ± 2.7	1.049 ± 0.046	0.779 ± 0.034
fcc	59.4 ± 4.3	0.846 ± 0.046	0.386 ± 0.031
bcc	83.1 ± 4.4	0.863 ± 0.035	0.368 ± 0.022

Table 3.5 Correlation fitting parameters for each simulated configuration of FePt.

cylindrical grains and "voronoi" grains were initially tested - the latter case involves grains having irregular, randomly-generated surfaces. An illustration of a sampled voronoi-structured grain is shown in Fig. 3.16. Unfortunately, the version 4 of the VAMPIRE code used at that time suffered from a serious limitation that the extraction of magnetic properties of each atomistic layer, which is a crucial prerequisite feature for the construction and analysis of magnetisation profiles later, can be done for only parallelepiped-shaped grains. It is especially difficult to

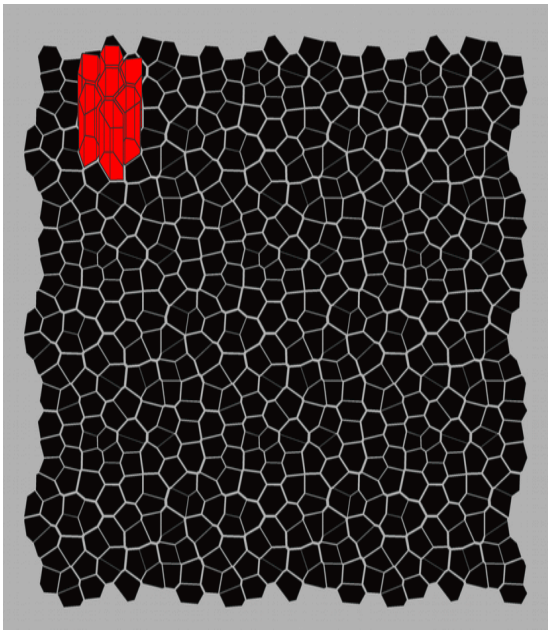

Fig. 3.16 A sample of voronoi-structured grains. Source: courtesy of Dr. Sergiu Ruta.

study voronoi-structured grains which do not have clear layers. Therefore, the investigation of non-parallelepiped grains could not be proceeded further. However, the omitted role of grain shape has been effectively mitigated by the later introduction of the shape-independent surface bond loss as the main variable in the mathematical description of magnetisation loss propagation. However, with more sophisticated versions of the VAMPIRE code having been

continuously developed since then, there is a possibility to revive the said investigation of the role of grain shape on finite-size effects. These could be the ideas for potential research in the future.

3.5 Summary

In this Chapter, the finite-size effects in small grains have been investigated. Simulation data fit to the classic Finite-size Scaling Law and show a rapid decrease of T_C at small sizes. We show that this is due to the propagation of surface disorder resulting from the loss of exchange coordination at the surface into the grain. This effect becomes important at grain sizes smaller than 4nm and is supported by semi-analytic mean field calculation. The findings overall are consistent with the mean-field calculation and have been extended to incorporate different crystal structures, which strongly suggests that if using a suitable correlation factor the T_C distribution of a generic material can be correlated to the percentage of atomistic bond loss on the surface as a universal parameter. The reduction of T_C is driven by surface magnetic disorder resulting from the loss of exchange coordination at the surface. These fluctuations cause a renormalisation of state energies through which the magnetic disorder propagates into the grain. A physically reasonable expression is proposed which separates the two processes, and defines a penetration depth for the propagation of disorder into the grain. For small grain sizes less than around 3-4 nm, the decrease in magnetic order due to state energy renormalisation cannot be stabilised by a fully-ordered central core. In this regime the state energy renormalisation becomes the dominant factor leading to a rapid collapse of the magnetisation and T_C and a consequent increase of the dispersion of T_C for small diameter. From the viewpoint of materials design for nanoscale applications such as spintronics and particularly Heat Assisted Magnetic Recording, finite size effects will become an increasingly important consideration with decreasing device size. Because of the strong surface effects on the decrease of T_C, the increased T_C dispersion for small grains could be somewhat mediated in designs coupling low T_C hard materials such as FePt with high T_C materials which would reduce the loss of magnetic order through the proximity effect. Overall, surface effects could limit the performance of Heat-assisted Magnetic Recording, which could be important for $L1_0$-FePt in particular because of the 2-ion anisotropy which will be further explored in the next Chapter 4.

4

Higher-order magnetic anisotropy in soft-hard nanocomposite materials

We studied computationally the properties of higher-order magnetic anisotropy constants in a $L1_0$/A1-FePt core-shell system which is characterised by a strong 2-ion Fe-Pt anisotropy component. We discover that the core-shell structure exhibits an unexpected fourth-order anisotropy term whose magnitude depends on the core-size ratio R. The K_2/K_1 ratio, with K_1 and K_2 being the second and fourth-order anisotropy constant respectively, displays a non-monotonic variation with a peak occurring at $R \approx 0.50$. Furthermore, we find that K_2 scales with the normalised magnetisation (M/M_s) at temperatures below the Curie temperature with a scaling exponent of approximately 2.2 - a remarkable deviation from the established Callen-Callen theory which instead predicts a scaling exponent of 10. We construct a simple analytic model which shows the fourth-order term to arise from the canting of the core and shell magnetisation. In particular, our model demonstrates that the magnitude of the fourth-order term is proportional to K_1^2/J, with J the exchange coupling. Given that in $L1_0$-FePt the 2-ion K_1 constant scales approximately with $(M/M_s)^{2.1}$ and J with $(M/M_s)^2$, the predicted scaling exponent agrees very well with our simulation. Generally, the fourth-order anisotropy constant is shown to exhibit a strong dependence on the system geometry, thus suggesting that the Callen-Callen power law is non-universal and valid only for single-ion anisotropies.

4.1 Motivation

Chapter 3 has discussed the suitability of $L1_0$-FePt as a recording media for Heat-assisted Magnetic Recording (HAMR) and presented a study on the first key magnetic attribute of $L1_0$-FePt for potential applications in HAMR, namely the strong size-dependence of its Curie temperature. This Chapter, in turn, will encompass an investigation on the second magnetic

attribute of $L1_0$-FePt which is its very strong 2-ion anisotropy contribution to the overall exceptionally high uniaxial anisotropy of the material [66, 94]. The origin of this 2-ion anisotropy component in the chemically layered ferromagnet $L1_0$-FePt has been well established to be from the contribution of the $5d$ element which has a large spin-orbit coupling whilst the $3d$ element provides the exchange splitting of the $5d$ sub-lattice [95–100].

Measurements of the second-order anisotropy constant K_1 in $L1_0$-FePt using a simple angular form of the magnetic anisotropy energy function $E = K_1 \sin^2\theta$ have generally been consistent and well established [66, 87, 94, 101, 102] with values for the magnetic anisotropy energy as high as 6.2 MJ/m^3 [103]. On the contrary, there has not been a consensus on the existence and the significance of the fourth-order term K_2. Previous studies have arrived at conflicting conclusions where K_2 has been argued to be a misinterpretation [103], negligibly small compared to K_1 [102], or non-negligible [66]. This presents a potential problem for HAMR application since the thermal stability of the writing medium is determined by anisotropy. In addition, there has been a reported deviation of the scaling of K_2 [102] from the classical Callen-Callen power law [57] which, interestingly, has also been observed in other materials [104, 105].

Furthermore, a recent study by Sepehri-Amin et al. [106] on $L1_0$-FePt thin film discovered an effect of Pt enrichment on the film surface regardless of the FePt composition, which subsequently was shown to distort the ordered structure of the $L1_0$ phase and thus reduce the magnetocrystalline anisotropy of the FePt grain. This phenomenon is illustrated in Fig. 4.1 taken from Sepehri-Amin et al. [106] which clearly shows a heavy intermixing of the Fe atoms and Pt atoms on the grain surface. The proportions of Fe and Pt atoms at various distances from the surface, which are plotted in the sub-graphs underneath, are shown to be dependent on grain size. The intermingling between Fe and Pt atoms at the grain surface compromises the chemical ordering of $L1_0$-FePt grain, thus reducing the grain uniaxial anisotropy. The impact of this Pt segregation is found to be more pronounced in grains smaller than 15nm, which is detrimental for HAMR functioning where smaller grain sizes are desired. Furthermore, the varying relative proportion of the two $L1_0/A1$ phases has also been reported to affect the uniaxial magnetic anisotropy in previous experimental studies of phase-graded thin films [72]. The effect of Pt surface segregation in a phase-graded FePt system, therefore, necessitates a substantial investigation into the role of grain shape and composition on the anisotropy of $L1_0$-FePt.

The background contexts which have recently been discussed provide the justifications for the focus of this Chapter on an investigation of higher-order anisotropy of $L1_0$-FePt, in particular the properties of the fourth-order anisotropy constant K_2, for the implementation of $L1_0$-FePt as a HAMR recording media. In this Chapter, an analytic model will be proposed and

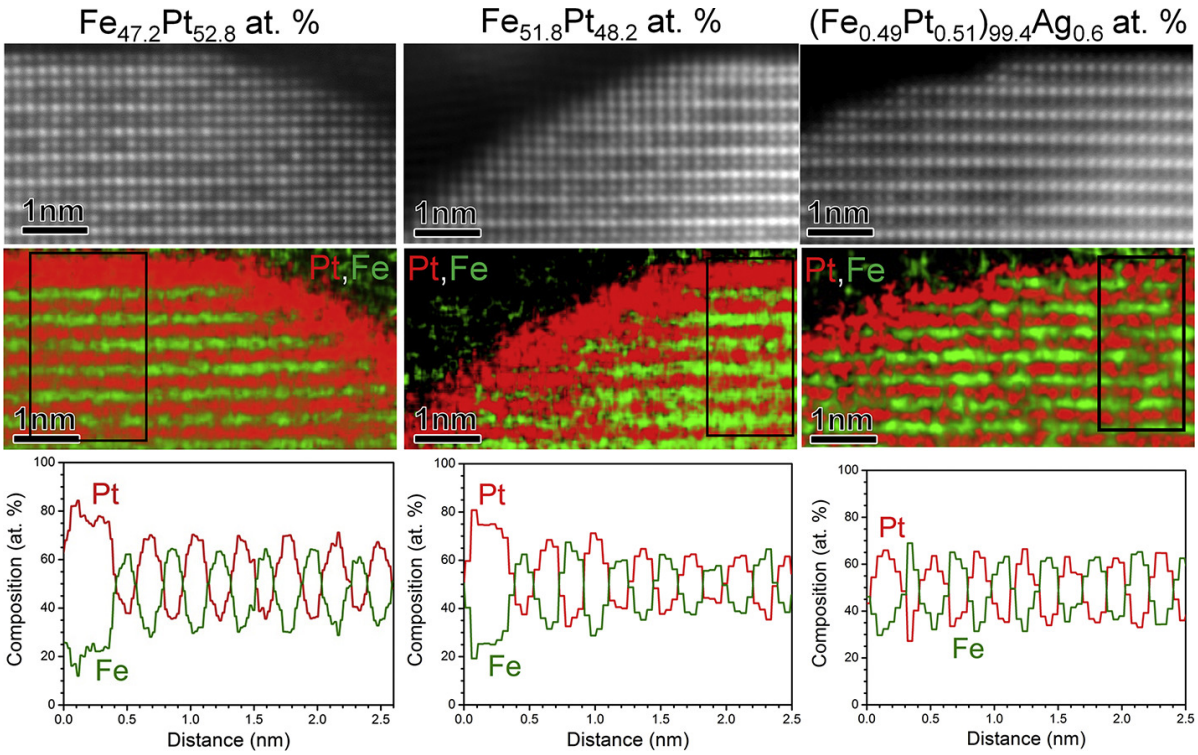

Fig. 4.1 Pt surface segregation observed in experimental $L1_0$-FePt grains of various compositions. The Fe atoms in green and Pt atoms in red are seen to be intermixed heavily at the grain surface. The proportions of Fe and Pt atoms as a function of distance from the surface are plotted in the sub-graphs underneath and show a grain-size dependence. Source: excerpt from [106]

described to explain the origin and mechanism of this fourth-order anisotropy. The applicability of this analytic model will be shown to be extendable to not just $L1_0$-FePt but a generic nanocomposite material with soft-hard magnetic inter-layers.

4.2 Simulation methods and settings

4.2.1 Construction of the FePt core-shell grains

In Chapter 3, because of the particular interest of extracting magnetic properties on the scale of atomistic layers, FePt grains were deliberately simplified to having paralellepiped shape which offers the highest degree of symmetry and regularity. Real grains which are produced and tested in experiments, rarely have such cubic shape. In this Chapter, therefore, simulated FePt grains are created in an elongated cylindrical shape with faceted surfaces which more closely resembles ones typically found in a HAMR recording media. The VAMPIRE code

features the creation of such faceted, systems via the input specification of 3 cutting fractional radii along the [100], [110], and [111] crystal lattice directions [107]. The characteristic grain diameter, based on the investigation of grain sizes in Chapter 3, is chosen to be 8nm. The grains are made elongated along its height on the z-dimension by a shape factor of 1.5, thus resulting in the overall dimensional sizes of $8 \times 8 \times 12$ nm. The front, side, and top views of the VAMPIRE-generated FePt grains are shown in Fig. 4.2.

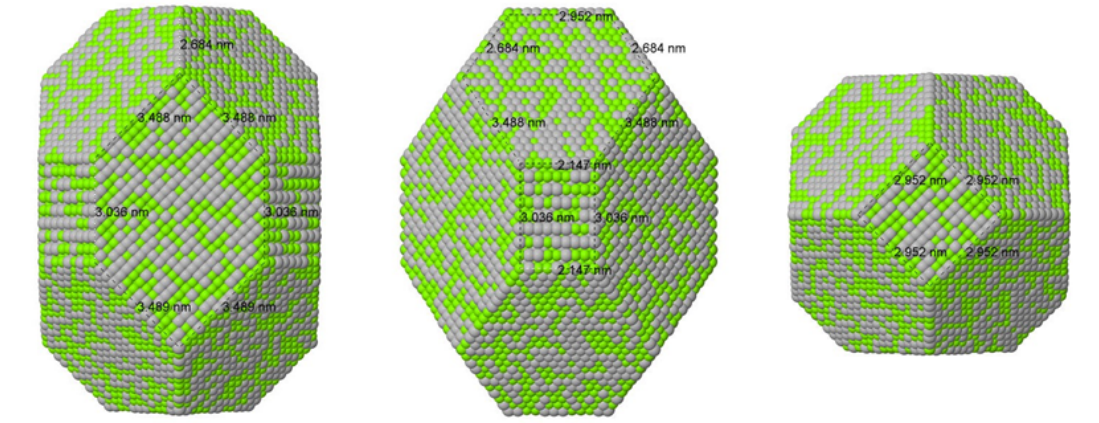

Fig. 4.2 Jmol-generated visualisations of the faceted, elongated FePt grain with Fe atoms in green and Pt atoms in white: (left) front view, (middle) side view, and (right) top view. This grain is created with the cutting fractional radius of 1.00, 1.05, and 1.00 along the [100], [110], and [111] crystal lattice direction respectively.

In order to replicate the effect of Pt surface segregation in Sepehri-Amin et al. [106], the simulated FePt grain will have a core-shell structure with a core made of the ordered $L1_0$-phase FePt surrounded by a disordered $A1$-phase FePt shell. The diameter of the core, d_{core}, can be freely adjusted so as to reproduce the varying degrees of ordering. The fractional core size R of the grain is defined as the ratio of the core diameter d_{core} to the entire grain diameter d_{grain} and in simulations is varied between 0.05 and 0.95 in a 0.5 increment:

$$R = \frac{d_{\text{shell}}}{d_{\text{grain}}}. \tag{4.1}$$

The lower and upper bounds of R represent two extreme cases: when $R = 0.05$ the $L1_0$ core consists of only one single atom, whilst when $R = 0.95$ the grain has only one atomistic layer of the $A1$-phase shell. An illustration of the cross-sectional views of the constructed core-shell grains with various core sizes R are shown in Fig. 4.3. The unit cell of the fct $L1_0$-FePt is slightly compressed on the c-axis [82, 83, 108] whilst the unit cell of the fcc $A1$-FePt is not.

To average this disparity, a common unit cell is implemented for both the $L1_0$ and $A1$ phases with a uniform cubic shape and a lattice spacing of $a = 0.3795$ nm which is obtained from experiments and in consistency with previous computational studies [70, 83, 108, 109].

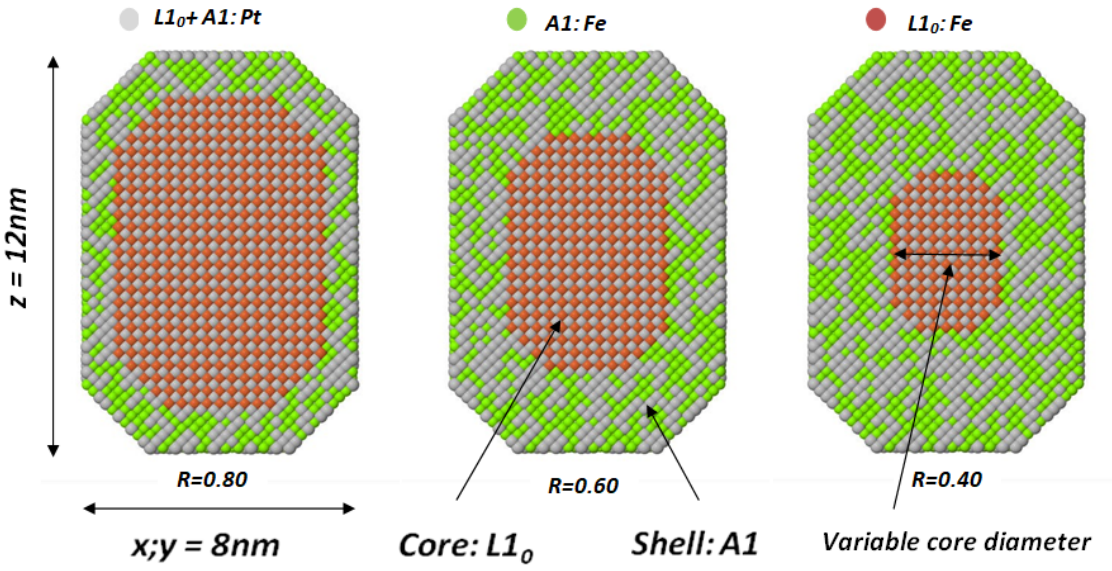

Fig. 4.3 Jmol-visualised cross-sectional view of sampled core-shell grains with core size (left) $R = 0.80$, (middle) $R = 0.60$ and (right) $R = 0.40$. The size-adjustable core is made of the ordered $L1_0$-FePt whilst the shell is made of the disordered $A1$-FePt. Pt atoms are coloured in white; Fe atoms in brown if of the $L1_0$ phase and in green if of the $A1$ phase.

4.2.2 The truncated exchange interaction

The exchange interaction $\mathcal{J}_{ij}$ implemented in the core-shell simulations in this Chapter takes the form of a 3-dimensional tensor including components on the xyz-dimensional directions and extending further than the strictly nearest-neighbour only form which was presented in the previous Chapter 3 - the reason for which, again, is to account for the impact of surface disorder due to the aforementioned Pt segregation effect [106]. However, as previously explained in Chapter 2, the exchange interaction strength decreases sharply with increasing distances between neighbouring atoms, thus quickly dropping to a negligible magnitude. Therefore, instead of using a full-range exchange interaction derived from ab-initio calculation, a reasonably good estimation will include the exchange interactions up to the third-level of nearest-neighbours. This model of the exchange is termed a truncated exchange interaction - illustrated in Fig. 4.4 - and is calculated from the full-range version in order to preserve the bulk properties of FePt. The truncated exchange interaction strength can be expressed

mathematically as:

$$J^0 = \sum_{k=1,2,3} n_k J^k, \tag{4.2}$$

where J^0 is the "total" exchange interaction strength summing from all k-level nearest-neighbour components, n_k the number of k-level nearest-neighbours, and J^k the exchange interaction between k-level nearest-neighbours. Note the use of the term "k-level" prefixing "nearest-neighbours" is purely for simplicity, so that the 1st-level refers to the nearest neighbours, 2nd-level the next-nearest neighbours, and 3rd-level the next-next-nearest neighbours.

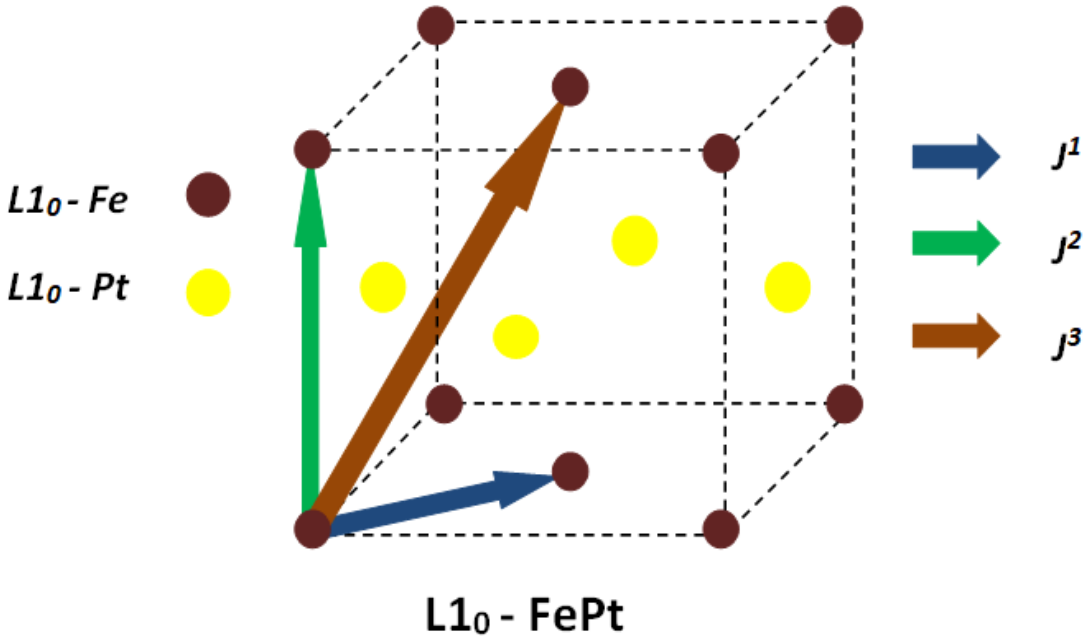

Fig. 4.4 Visualisation of the Fe neighbours in $L1_0$-FePt up to the third-level of nearest-neighbour. The Fe atoms are coloured brown; the Pt atoms are coloured yellow and are incorporated into the effective Hamiltonian following Mryasov et al.'s treatment [67] utilising only the Fe degrees of freedom. Each $k^{th} - level$ nearest-neighbour has its own associated effective exchange interaction J^k.

Because the exchange tensor $\mathcal{J}_{ij}$ applies to both the fct-lattice $L1_0$ and fcc-lattice $A1$ phases, the calculation of the exchange component J^k - with the superscript k denoting the interaction between the referenced atom with its k-level of nearest neighbours - will need to take into account the different numbers of k-level nearest-neighbours, n_k, existing in the lattice structure of each phase. The starting point is the observation that for the "artificial" bulk fcc-FePt configuration investigated in Chapter 3, using an exchange energy strength of

$J_{fcc}^{nn} \approx 3 \times 10^{-21}$ J/link, where the superscript *nn* indicates nearest-neighbour interaction, would yield a Curie temperature of approximately 700 K which is reasonable in comparison with experiment [80]. Since simulations in Chapter 3 involves only nearest neighbours, which in bulk fcc is a total of 12, the total exchange interaction strength in bulk fcc is summed up from all 12 nearest-neighbours and can be expressed as $J_{fcc}^{0} = 12J_{fcc}^{nn}$. Since both the $A1$-FePt and $L1_0$-FePt are lattice-wise equivalent to the bulk fcc, the total exchange interaction strength of each phase can similarly be assigned the same numerical value $J_{A1}^{0} = J_{L1_0}^{0} = J_{fcc}^{0} = 12J_{fcc}^{nn}$.

Mryasov et al.'s model of the 2-ion anisotropy component of $L1_0$-FePt [67] allows the removal of Pt atoms from the fct lattice structure, thus leaving only Fe-Fe interactions with modified properties as explained in detail in Chapter 3. For the $A1$ phase, the random distribution of Fe and Pt atoms results in a highly chemically disordered structure with extremely low uniaxial anisotropy [110] in which the non-magnetic Fe-Pt interactions do not contribute to the magnetic properties of the material. Consequently, in VAMPIRE simulations the Pt atoms of both $A1$ and $L1_0$ phase of FePt are treated as non-magnetic and will not be accounted for in calculations.

In the $A1$ phase, an atom can have at maximum 12, 6, and 24 1st-level, 2nd-level, and 3rd-level nearest neighbours respectively. However, since statistically 50 percent of total atoms in the $A1$ phase are the non-magnetic Pt, the averaged numbers of neighbours in the $A1$ phase need to be correspondingly halved. Therefore Eq. (4.2) applied for the $A1$ phase will become:

$$J_{A1}^{0} = 6J^1 + 3J^2 + 12J^3 = 12J_{fcc}^{nn}. \tag{4.3}$$

For the $L1_0$ phase, with 4 Pt atoms in each middle layers being removed, there are 4, 6, and 8 nearest-neighbours of the 1st, 2nd, and 3rd-level respectively. Therefore the total exchange interaction strength in the $L1_0$ phase can be expressed as:

$$J_{L1_0}^{0} = 4J^1 + 6J^2 + 8J^3 = 12J_{fcc}^{nn}. \tag{4.4}$$

Another approximation is derived from a study by Hinzke et al. [111] which found that for the $L1_0$ phase the ratio between out-of-plane total exchange to in-plane total exchange can be roughly estimated at $3/4$. From the illustration in Fig. 4.4 it can be seen that the out-of-plane exchange comprises of all 8 J^3 components and the 2 J^2 components along the [001] lattice direction, whilst the in-plane exchange includes all 4 J^1 components and the 4 remaining J^2 components along the [100] and [010] lattice direction. Therefore:

$$8J^3 + 2J^2 = \frac{3}{4}\left(4J^1 + 4J^2\right). \tag{4.5}$$

Solving Eq. (4.3), Eq. (4.4), and Eq. (4.5) simultaneously yields the solution, to 7 decimals and being imported directly into VAMPIRE simulations, as:

$$\begin{aligned} J^1_{xyz} &= 0.7142857 J^{nn}_{fcc} = 2.1428571 \times 10^{-21}\ J/link \\ J^2_{xyz} &= J^{nn}_{fcc} = 3.0000000 \times 10^{-21}\ J/link \\ J^3_{xyz} &= 0.3928571 J^{nn}_{fcc} = 1.1785714 \times 10^{-21}\ J/link. \end{aligned} \tag{4.6}$$

Overall, under these treatments, the entire core-shell grain is expected to exhibit closely comparable Curie temperatures for both the $L1_0$ core and the $A1$ shell which again, is consistent with experiment [106].

4.2.3 The truncated 2-ion anisotropy

The implementation of the dominant 2-ion anisotropy in the $L1_0$ phase is done in a similar method to the previous calculation of the truncated exchange interaction. First, the 2-ion anisotropy also takes the form of a 3-dimensional tensor $\mathcal{K}^{2ion}_{ij}$ which, following Mryasov et al.'s treatment [67], introduces a 2-ion Hamiltonian component $\mathcal{H}_{2ion}$:

$$\mathcal{H}_{2ion} = -\frac{1}{2} \sum_{i,j \in core} \left(\hat{\mathbf{S}}^z_i\right)^T \mathcal{K}^{2ion}_{ij} \hat{\mathbf{S}}^z_j, \tag{4.7}$$

where $\hat{\mathbf{S}}_i$ and $\hat{\mathbf{S}}_j$ are spin unit vectors and the superscript z indicates that the 2-ion anisotropy applies only to the z-component of the spins - thus the 2-ion anisotropy tensor $\mathcal{K}^{2ion}_{ij}$ has all x and y-dimensional components equal 0. Furthermore, the 2-ion anisotropy tensor $\mathcal{K}^{2ion}_{ij}$ is also truncated instead of being fully long-range, extending up to the 3rd-level of nearest-neighbours. The numerical values of the non-zero z-component of the 2-ion anisotropy applicable for each 1st, 2nd, and 3rd-level nearest-neighbours are the solution to the following 3 simultaneous equations:

$$\begin{aligned} 6K^1 + 3K^2 + 12K^3 &= k_{2ion} \\ 4K^1 + 6K^2 + 8K^3 &= k_{2ion} \\ 8K^3 + 2K^2 &= \frac{3}{4}\left(4K^1 + 4K^2\right), \end{aligned} \tag{4.8}$$

where $k_{2ion} = 12K^0 = 1.427$ meV/link $= 2.2832 \times 10^{-22}$ J/link is the 2-ion anisotropy constant extracted from Mryasov et al. [67]. The solution, similar to the exchange solution before and

recalling that the 2-ion anisotropy tensor has only a non-zero z-component, is given as:

$$\begin{aligned} K_z^1 &= 0.7142857K^0 = 1.9026667 \times 10^{-23}\ J/link \\ K_z^2 &= K^0 = 1.3590476 \times 10^{-23}\ J/link \\ K_z^3 &= 0.3928571K^0 = 7.4747611 \times 10^{-24}\ J/link. \end{aligned} \tag{4.9}$$

4.2.4 The Spin Hamiltonian

The spin Hamiltonian of the core-shell simulations is the sum of the respective Hamiltonian of the $L1_0$-phase core and of the $A1$-phase shell $\mathcal{H} = \mathcal{H}_{\text{core}} + \mathcal{H}_{\text{shell}}$ which, following the standard Heisenberg form, includes the exchange and anisotropy components. Similar to simulations in Chapter 3 there will be no externally applied magnetic field $\mathbf{B}$. The explicit mathematical expression for the Hamiltonian of the core and of the shell are given as follows:

$$\mathcal{H}_{\text{core}} = -\frac{1}{2} \sum_{i,j \in core^*} \left(\hat{\mathbf{S}}_i\right)^T \mathcal{J}_{ij} \hat{\mathbf{S}}_j - k_{loc}^{L1_0} \sum_{i \in core} (\hat{\mathbf{S}}_i^z)^2 - \frac{1}{2} \sum_{i,j \in core} \left(\hat{\mathbf{S}}_i^T\right)^z \mathcal{K}_{2ion} \hat{\mathbf{S}}_j^z, \tag{4.10}$$

$$\mathcal{H}_{\text{shell}} = -\frac{1}{2} \sum_{i,j \in shell} \left(\hat{\mathbf{S}}_i\right)^T \mathcal{J}_{ij} \hat{\mathbf{S}}_j - k_{loc}^{A1} \sum_{i \in shell} (\hat{\mathbf{S}}_i^z)^2, \tag{4.11}$$

where $\hat{\mathbf{S}}_i$ and $\hat{\mathbf{S}}_J$ are spin unit vectors, $\mathcal{J}_{ij}$ the exchange energy tensor between neighbouring pair (i, j), and k_{loc} the local, in-plane single-site anisotropies of the respective phase. The notation $i, j \in core^*$ of the first summation in Eq. (4.10) accounts for exchange interactions not only in the core but also across the core/shell interface as well. The superscript z, where applicable, denotes the z-component of the spins. The superscript T, where applicable, denotes the transpose of the spin matrix. In VAMPIRE simulations the numerical values of the in-plane single-site anisotropies are set to $k_{loc}^{A1} = 0$ [110] and $k_{loc}^{L1_0} = -0.097$ meV/atom $= -1.552 \times 10^{-23}$ J/atom [67]

Furthermore, as explained before in Chapter 2, since the 2-ion anisotropy acts on neighbouring pairs of spins in a similar fashion to that of the exchange interaction, for computational efficiency it can be combined directly with the exchange energy term to form an anisotropic exchange. A sample of the VAMPIRE material file showing the implementation of such anisotropic exchange in simulations is given in Appendix B.

4.2.5 The torque method

The magnetocrystalline anisotropy constants of the core-shell grains are computed by the torque method [112, 113], with the basic principles outlined as follows. First, the torque $\tau(\theta)$

can be defined as the angular derivative of the energy $E(\theta)$ by $\tau(\theta) = -dE(\theta)/d\theta$. In a uniaxial system, the angular-dependent magnetocrystalline anisotropy energy $E(\theta)$ can be mathematically expressed as a series of anisotropy constants in even orders of $\sin(\theta)$ such that $E = E_0 + K_1 \sin^2(\theta) + K_2 \sin^4(\theta) + ...$ which can be expanded as much as appropriate, where the constant E_0 can usually be omitted in mathematical formalism and K_1 and K_2 are the second and fourth-order anisotropy constants respectively. Therefore, by fitting to the torque computed from simulation output, the values of anisotropy constants can be determined. Also, the magnetocrystalline anisotropy energy can be calculated by $E_{\text{anisotropy}} = E(\theta = 90^o) - E(\theta = 0^o) = K_1 + K_2 + ...$ In specific cases which include up to the fourth-order anisotropy constant, it can be shown straightforwardly that the magnetocrystalline anisotropy energy can also be calculated via the torque as $E_{\text{anisotropy}} = -\tau(\theta = 45^o)$.

Calculations based on the torque method are performed in the VAMPIRE atomistic code [39, 52] through the implementation of a constrained Monte-Carlo (CMC) integrator [56] in which the system magnetisation can be constrained at an angle θ to the easy axis. In the case of $L1_0$-FePt, the easy axis lies along the [001] lattice direction which is chosen to be the z-dimension. At each value of the angle θ, the angular dependence of the restoring torque $\tau(\theta)$ on the simulated system can be calculated and output. At any given temperature, a full angular sweep is performed for θ from 0 to 180 degrees in 5-degree steps. The simulation is then carried out for temperature from 0 K to 1000 K in 5 K steps.

Other technical aspects of VAMPIRE simulations which have been previously described in Chapter 2 and 3 are all valid and continue to be applicable. In summary, the numerical values of exchange energy and anisotropies, as well as other simulation parameters are tabulated in Table 4.1. Sampled VAMPIRE input and material files for the simulations of this Chapter are given in Appendix B.

Parameter	Notation	Unit	$L1_0$-phase	A1-phase
Damping Constant	ζ		1.0	1.0
Atomistic Spin Moment	μ_s	μ_B	3.23	3.23
Local anisotropy	k_{loc}	J/atom	-1.55×10^{-23}	0
2-ion anisotropy	k_{2ion}	J/atom	2.23×10^{-22}	0
Total Exchange Strength	J^0	J/link	3×10^{-21}	3×10^{-21}
CMC Equilibration step			2×10^5	2×10^5
CMC Total step			8×10^5	8×10^5

Table 4.1 VAMPIRE parameters for the core-shell simulations.

4.3 Results and discussion

4.3.1 Validating the scaling law of the second-order anisotropy

The Callen-Callen theory [57] describes the temperature dependence of the n^{th}-order magnetic anisotropy constant for simple, single-sublattice ferromagnets by scaling it against the magnetisation by a power law:

$$\frac{K(T)}{K(0)} = \left[\frac{M_s(T)}{M_s(0)}\right]^{\beta}, \tag{4.12}$$

where the scaling exponent obeys $\beta = n(n+1)/2$. Therefore, for the second-order and fourth-order anisotropy constant the scaling exponent according to the Callen-Callen power law would be $\beta = 3$ and $\beta = 10$ respectively. For the case of the second-order anisotropy constant K_1 of FePt specifically, classical mean-field estimations [114] and low-temperature measurements [87] somewhat conforms to Callen-Callen prediction, whereas more refined numerical calculation and experiment data [67, 114–119] have established a more precise and widely accepted value of $\beta \approx 2.1$. This well-established scaling exponent of K_1 of $L1_0$-FePt, therefore, can serve as a reliable benchmark against which the previously described models of the truncated exchange interaction and 2-ion anisotropy can be validated. The argument is that if the calculations are done correctly, the values of the truncated exchange interaction and 2-ion anisotropy components obtained from Eq. (4.6) and Eq. (4.9), when applied to a bulk $L1_0$ system, should yield a scaling exponent of K_1 in good agreement with the known value $\beta \approx 2.1$. In order to conduct this test, a bulk $L1_0$-FePt grain is created in form of a $8nm \times 8nm \times 8nm$ cube with periodic boundary conditions - see Fig. 4.5. The original expression of the Callen-Callen power law in Eq. (4.12) can be rewritten in a linear log-log fit as:

$$\begin{aligned} ln\left[K_1(T)\right] &= ln\left[K_1(0)\left[\frac{M_s(T)}{M_s(0)}\right]^{\beta}\right] = ln\left[K_1(0)\right] + \beta\frac{M_s(T)}{M_s(0)} \\ &= constant + \beta\frac{M_s(T)}{M_s(0)}, \end{aligned} \tag{4.13}$$

which when plotted against $M_s(T)/M_s(0)$ will yield the scaling exponent β as the gradient. The values of the second-order anisotropy constant K_1 extracted from the simulated bulk $L1_0$-FePt are fit against the log-magnetisation by Eq. (4.13). The result is shown in Fig. 4.6 with the obtained scaling exponent of $\beta = 2.050 \pm 0.002$ which is extremely close to the established value, thus validating the use of the truncated exchange energy and 2-ion anisotropy components presented earlier.

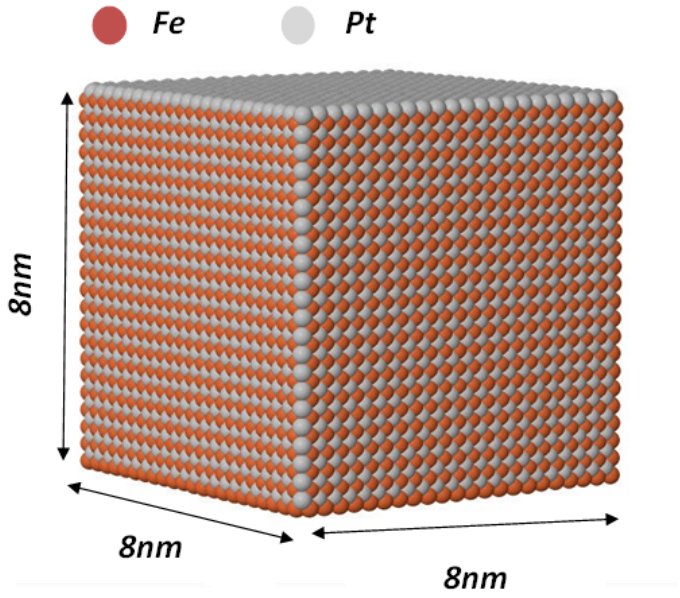

Fig. 4.5 Jmol-generated visualisation of the bulk $L1_0$ grain with a cubic shape of size 8nm. The Fe atoms are coloured brown and the Pt atoms white.

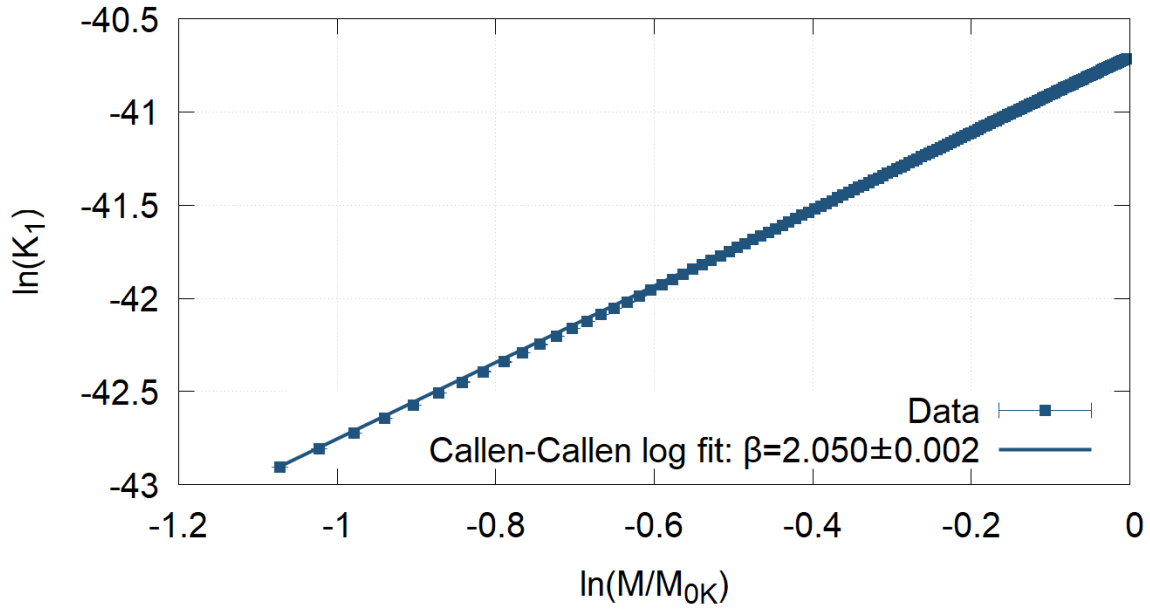

Fig. 4.6 The scaling of second-order anisotropy constant K_1 against M in a bulk $L1-0$-system yields a scaling exponent of $\beta = 2.050 \pm 0.002$ which is highly agreeable with the established value from literature.

4.3.2 The existence and magnitude of the fourth-order anisotropy

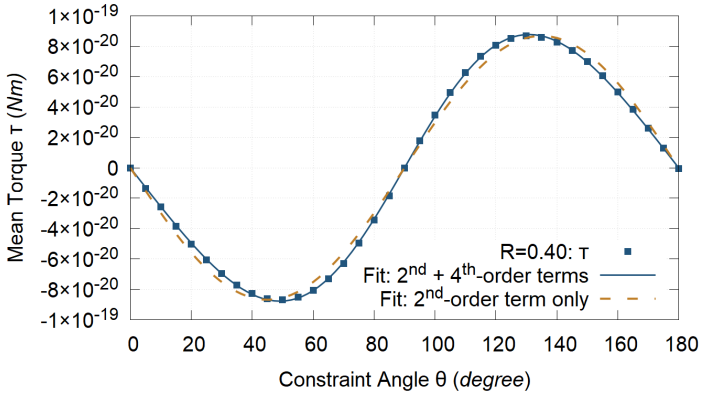

(a) $R = 0.40$

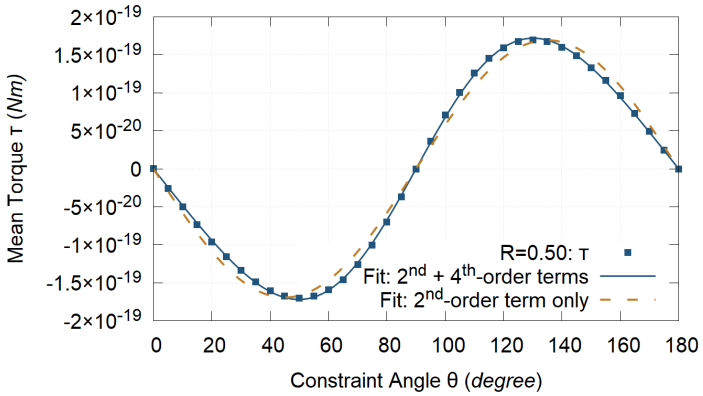

(b) $R = 0.50$

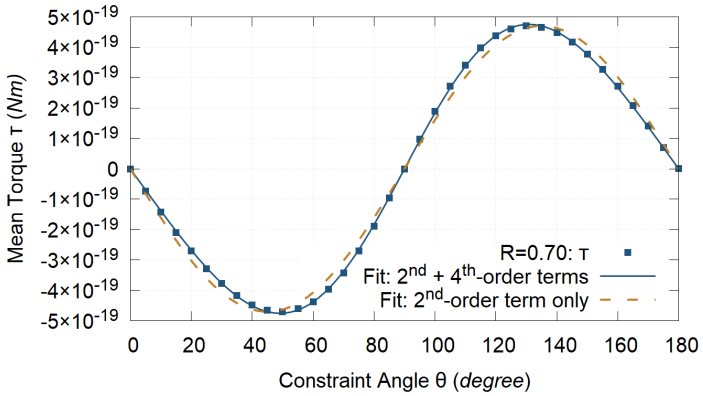

(c) $R = 0.70$

Fig. 4.7 Fitting to the torque τ for sampled core sizes (a) $R = 0.40$, (b) $R = 0.50$, and (c) $R = 0.70$ shows a discernible deviation from data if including only a second-order anisotropy term (dashed lines), whilst better matching if adding a fourth-order anisotropy term (solid lines).

The system magnetocrystalline anisotropy energy if assumed to include only the second-order anisotropy term $E = K\sin^2(\theta)$ would imply an exerting torque in form of $\tau = -dE/d\theta \propto \sin(2\theta)$. However, data obtained from simulations as shown in Fig. 4.7 demonstrates that in core-shell grains of certain core sizes R, a torque fit in such form - represented by the dashed line - is noticeably skewed from simulation data - represented in solid symbols. In contrast, when a fourth-order anisotropy term is added to the magnetocrystalline anisotropy energy expression i.e. $E = K_1\sin^2(\theta) + K_2\sin^4(\theta)$, the new torque fit - represented by the solid line in Fig. 4.7 and having the mathematical form expressed by:

$$\tau = -\frac{dE}{d\theta} = -K_1\sin(2\theta) - 2K_2\sin^3\theta\sin(2\theta), \tag{4.14}$$

now matches the simulated data extremely well. The discernible skewing of the torque curve in comparison to a simple $\sin(2\theta)$ profile has been observed in a previous experimental study on FePt granular films [120], although interestingly it should be noted that the authors of the cited paper themselves, whilst presenting multiple clearly skewed torque curves in their Figure 5 for films of various magnetic layer thickness d_{mag}, did not seem to recognise the very effect. For the core-shell simulations, however, the drawn conclusion is that the skewed torque curves seen in Fig. 4.7 are an indicator that the core-shell grains of certain core sizes R do exhibit a significant fourth-order anisotropy component which should not be neglected.

The temperature-dependent second and fourth-order anisotropy constants, K_1 and K_2, can then be extracted from the torque fit in Fig. 4.7 by using Eq. (4.14). The K_2/K_1 ratio is found to be dependent on the core size R with a non-monotonic variation that has not been reported elsewhere. Low-temperature data shown in Fig. 4.8, with sampled values of K_2/K_1 at 10 K tabulated in Table A.3 of Appendix A, indicate that the magnitude of K_2 can exceed 20% of K_1 which is a significant proportion.

4.3.3 The scaling law of the fourth-order anisotropy

In addition, the classical Callen-Callen power law predicts the scaling exponent of $\beta = 10$ for the fourth-order anisotropy constant K_2. However, simulation data appear to contradict this prediction. Fig. 4.9 illustrates an example of K_2 scaling obtained from simulation for core size $R = 0.70$ in which $\beta \approx 2.3$. Overall, the scaling exponent β across the simulated core size R range is found to be consistently lower than the Callen-Callen predicted theoretical value of 10 by significant amounts. The variation of the scaling exponent β as a function of the core size R for the fourth-order anisotropy K_2 as shown in Fig. 4.10, excluding the 2 extreme cases when $R = 0.05$ and $R \geq 0.90$ which will be revisited later, generally conforms to the range $2 \lessapprox \beta \lessapprox 3$.

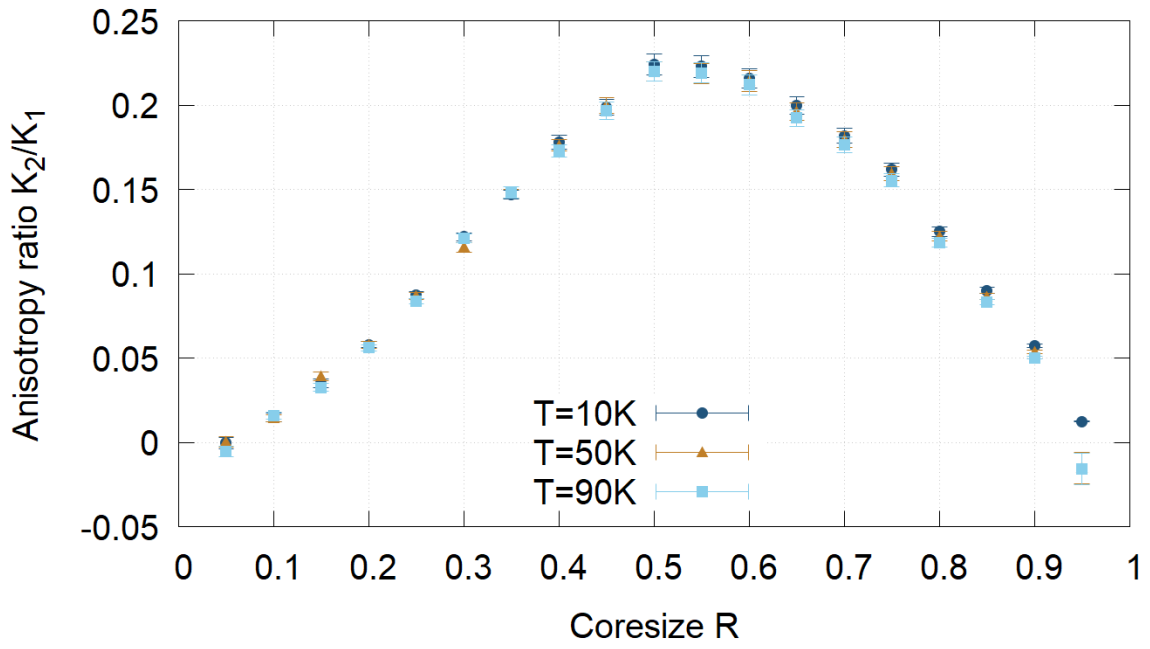

Fig. 4.8 The anisotropy K_2/K_1 ratio obtained from core-shell simulations exhibits a core size-dependent variation. The magnitude of K_2 can exceeded 20% of K_1. The variation of K_2/K_1 is later explained and quantified in an analytic model described in Section 4.4.

4.3.4 The temperature-dependent magnetisation

The temperature-dependent magnetisation $M(T)$ curves are plotted for simulated core-shell grains of varying core size R in Fig. 4.11 - (a) for the entire grain and (b) for the $L1_0$-core only. The total grain magnetisation curves are stable across different core sizes but the $L1_0$ core, shows significant finite-size effects. The behaviour of the $L1_0$-core is because of small number of spins exhibiting finite-size effects, and is consistent with previous results in Chapter 3.

The behaviour of the temperature-dependent magnetisation $M(T)$ of the entire core-shell grain as well as of each individual phase $L1_0$ and $A1$ is more closely examined in Fig. 4.12 for sampled core sizes. The magnetisation of the highly ordered $L1_0$-core is, expectedly, seen to be higher than that of the disordered $A1$-shell, and between the two phases there exists a clear exchange-coupling effect which results in the overall averaged-out magnetisation of the entire core-shell grain. This graded-phase exchange-coupling effect which occurs at the phase boundary has been seen before in experimental thin-film studies [72] and will be taken into account in the formulation of an analytic model later.

In summary, in this section the existence of a non-negligible fourth-order anisotropy term has been demonstrated which is also shown to exhibit two remarkable properties: first the non-monotonic core size-dependent variation of its magnitude, and second the non-Callen

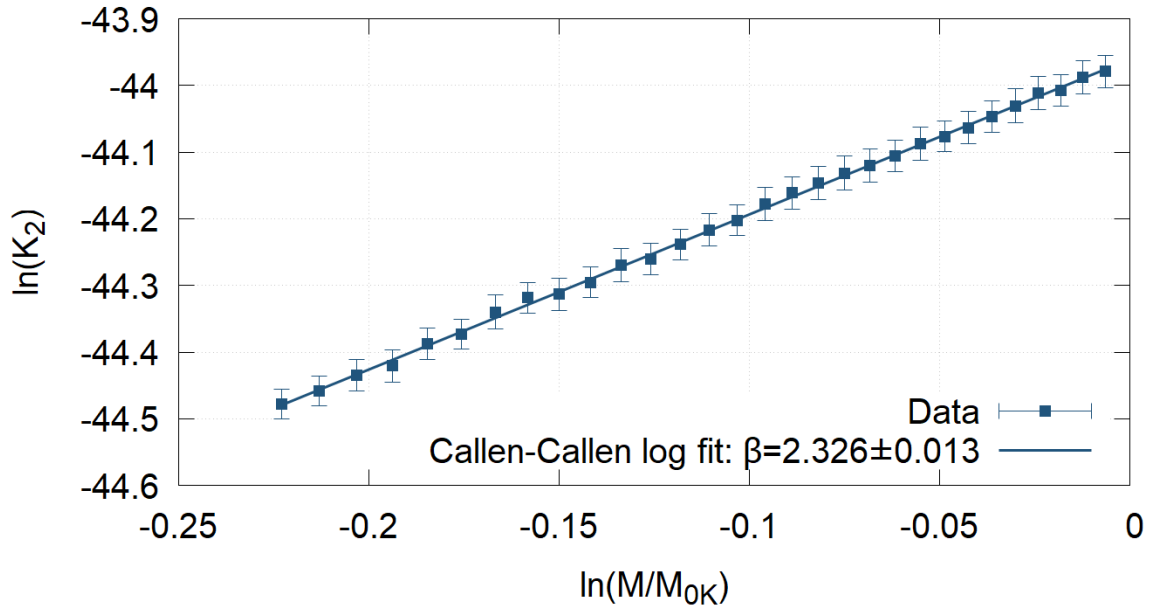

Fig. 4.9 Sampled scaling of the fourth-order anisotropy constant K_2 to the magnetisation for the core size $R = 0.70$ yields a scaling exponent $\beta \approx 2.3$ which remarkably disagrees with the Callen-Callen power law of $\beta = 10$.

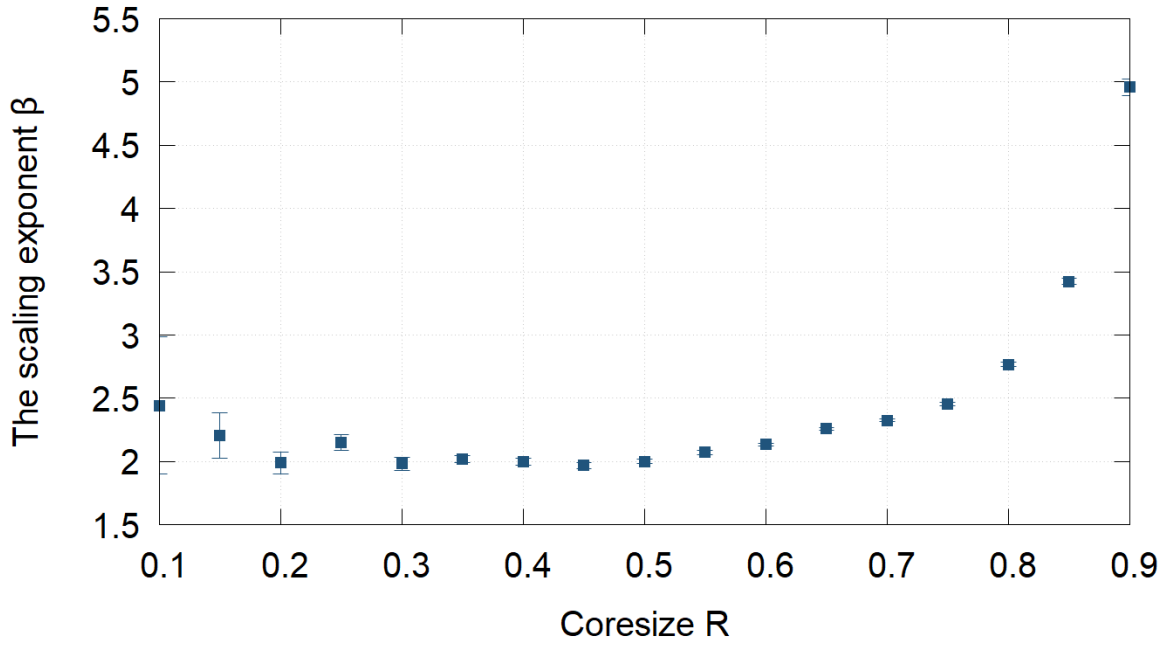

Fig. 4.10 Variation of the scaling exponent β of the fourth-order anisotropy constant K_2 as a function of the core size R.

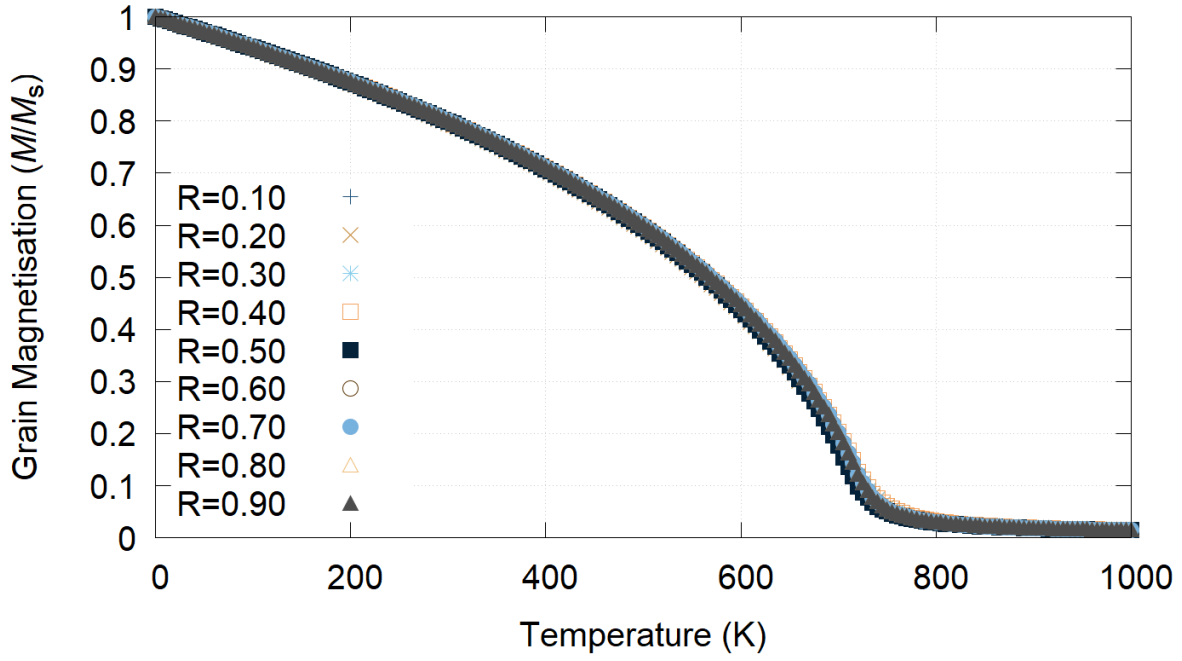

(a)

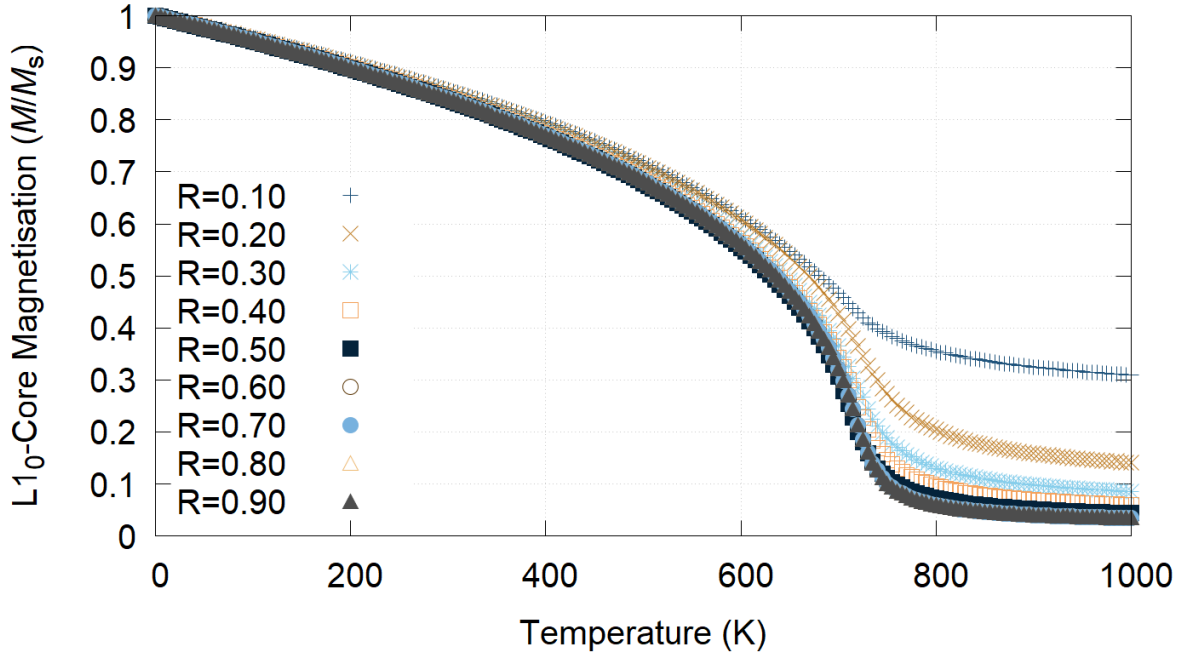

(b)

Fig. 4.11 The temperature-dependent magnetisation $M(T)$ for different core sizes R of (a) the entire grain, and (b) the $L1_0$-core only. Finite-size effects are clearly shown for the $L1_0$-core, which becomes extreme at low R.

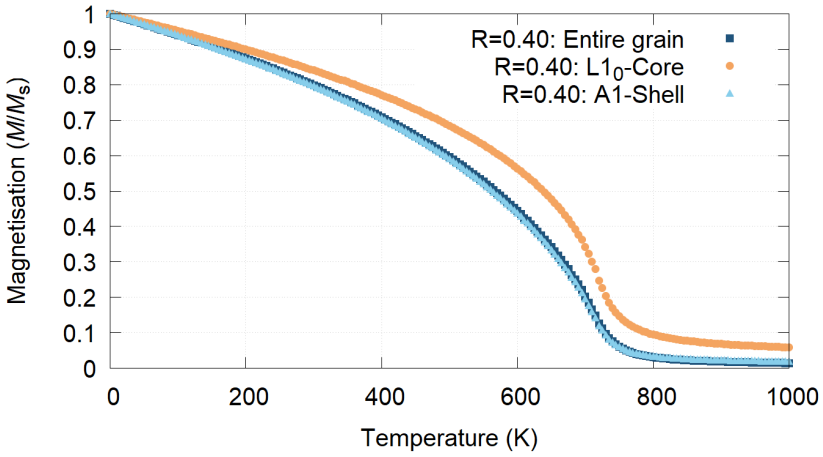

(a) $R = 0.40$

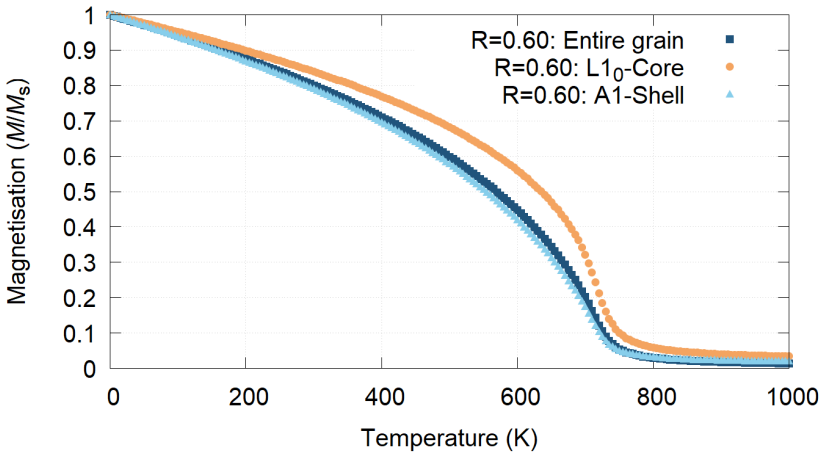

(b) $R = 0.60$

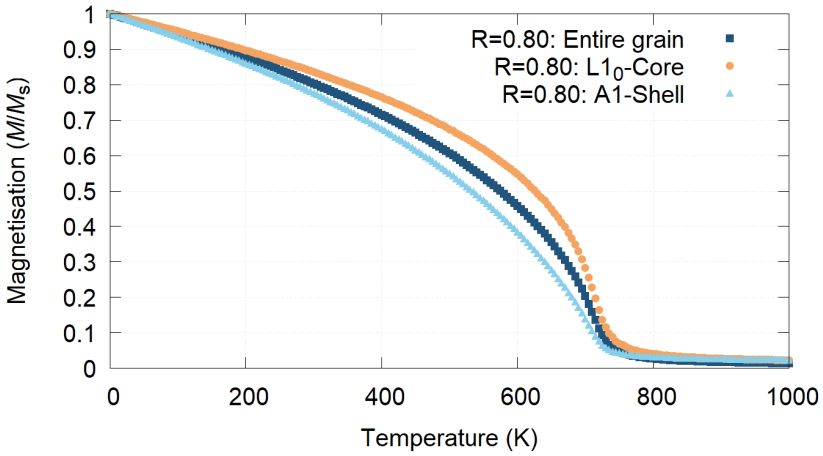

(c) $R = 0.80$

Fig. 4.12 The temperature-dependent magnetisation $M(T)$ of the entire core-shell grain and of each phase for core size (a) $R = 0.40$, (b) $R = 0.60$, and (c) $R = 0.80$ shows a coupling effect between the higher-magnetisation $L1_0$ core with the lower-magnetisation $A1$ shell. The resulting magnetisation of the entire core-shell is averaged out between the two.

scaling to the magnetisation. In order to discuss and explain the origin and behaviours of this novel fourth-order anisotropy term, a general analytic model will be proposed in the following section which will be shown to be applicable to not only the specific simulated core-shell FePt grains so far but also any generic material comprising of soft/hard magnetic interlayers.

4.4 An analytic model for the fourth-order anisotropy

In this section the derivation of an expression for the fourth-order anisotropy constant arising from an interface between two magnetic materials will be presented. This depends strongly on the system geometry and a derivation valid in the general case will be formalised. The starting point is to recall that the anisotropy is determined by calculating the torque on the system with the magnetisation constrained at an angle θ to the easy axis. Consider a general core-shell system in which the core is made of a hard-magnetic material and the shell a soft-magnetic one. First, a derivation which demonstrates the origin of the fourth-order anisotropy term to arise from the interface exchange energy and spin canting between the core and shell will be given. Next, the effect of an in-plane anisotropy term will be incorporated into the model. Finally, the analytic model will be applied, with considerations specific to the simulated core-shell structure, to re-examine the computational results presented earlier.

4.4.1 The derivation without an in-plane anisotropy

The model assumes that in order to minimise the energy the angles θ_h and θ_s in the hard and soft-magnetic phase can deviate from the system constrained angle θ by an amount of $\delta\theta_h$ and $\delta\theta_s$ respectively, thus $\theta_h = \theta + \delta\theta_h$ and $\theta_s = \theta + \delta\theta_s$. Because of the strength of the exchange coupling at the hard/soft interface it can reasonably be assumed that $\delta\theta_h$ and $\delta\theta_s$ are small and thus can be treated as perturbations. The energy of the 2-phase system, assuming for simplicity a scenario similar to the simulated FePt core-shell in which hard-magnetic material has a uniaxial anisotropy per volume K_u and the soft-magnetic one has a negligible uniaxial anisotropy, can then be written as:

$$E = K_u V_c \sin^2(\theta + \delta\theta_h) - \frac{JA_{cs}}{a^2}\cos(\delta\theta_h - \delta\theta_s), \tag{4.15}$$

where V_c is the volume of the hard-phase core, A_{cs} the area of the core/shell interface, a the lattice spacing, and J the exchange integral per link. The system energy E in Eq (4.15) consists of two components: the first a normal anisotropy term and the second an exchange energy term which represents the aforementioned exchange coupling between spins in the core and spins in

the shell. For simplicity, denote:

$$\begin{aligned} A &= K_u V_c, \\ B &= \frac{JA_{cs}}{a^2}. \end{aligned} \tag{4.16}$$

Eq. (4.15) must be minimised subject to the constraint function:

$$f\cos\theta_h + (1-f)\cos\theta_s - \cos\theta = 0, \tag{4.17}$$

with f being the fractional volume of the hard phase. This constraint function originates from the observation the constrained angle of the magnetisation of the hard and of soft phase is averaged from contributions of all spins in each respective phase. Therefore, the proportional sum of the hard and soft phase constrained angles - which is $f\cos\theta_h + (1-f)\cos\theta_s$ - must result in the overall system constrained angle - which is $\cos\theta$. Since $\theta_h = \theta + \delta\theta_h$ and $\theta_s = \theta + \delta\theta_s$, to first-order approximation it is straightforward to show that:

$$\delta\theta_s = -\frac{f}{1-f}\delta\theta_h = -F\delta\theta_h, \tag{4.18}$$

where $F = f/(1-f)$ and thus $\delta\theta_h - \delta\theta_s = \delta\theta_h + F\delta\theta_h = \delta\theta_h(1+F)$. To minimise the energy, derivative of E in Eq. (4.15) must be taken w.r.t. $\delta\theta_h$ which gives:

$$A\sin\left[2\left(\theta+\delta\theta_h\right)\right] + B(1+F)\sin\left[\delta\theta_h\left(1+F\right)\right] = 0. \tag{4.19}$$

The solution of Eq. (4.19), up to the first-order of $\delta\theta_h$, yields:

$$\delta\theta_h = -\frac{\sin\theta\cos\theta}{\frac{B}{2A}(1+F)^2}. \tag{4.20}$$

The energy E can then be calculated by substituting for $\delta\theta_h$ and $\delta\theta_s$ into Eq. (4.15), giving:

$$E = A\sin^2(\theta+\delta\theta_h) - B\cos\left(-\frac{\sin\theta\cos\theta}{\frac{B}{2A}(1+F)}\right). \tag{4.21}$$

Consider the expansion of the anisotropy term in Eq. (4.21) to first-order in small quantities:

$$\begin{aligned}
\sin^2(\theta+\delta\theta_h) &= (\sin\theta\cos\delta\theta_h+\cos\theta\sin\delta\theta_h)^2 \\
&= \sin^2\theta\cos^2\delta\theta_h+2\sin\theta\cos\delta\theta_h\cos\theta\sin\delta\theta_h+\cos^2\theta\sin^2\delta\theta_h \\
&\approx \sin^2\theta+(2\sin\theta\cos\theta)\,\delta\theta_h \\
&= \sin^2\theta-\frac{2\sin^2\theta\cos^2\theta}{\frac{B}{2A}(1+F)^2} \\
&= \sin^2\theta-\frac{\sin^2\theta}{\frac{B}{4A}(1+F)^2}+\frac{\sin^4\theta}{\frac{B}{4A}(1+F)^2}.
\end{aligned} \tag{4.22}$$

Next, expand the exchange term in Eq. (4.21) noting that the cosine argument is small:

$$\begin{aligned}
\cos(\delta\theta_h-\delta\theta_s) = \cos\left(\delta\theta_h(1+F)\right) &= \cos\left(\frac{-\sin\theta\cos\theta}{\frac{B}{2A}(1+F)}\right) \\
&\approx 1-\frac{\sin^2\theta\cos^2\theta}{2\left[\frac{B}{2A}(1+F)\right]^2} \\
&= 1-\frac{\sin^2\theta}{2\left[\frac{B}{2A}(1+F)\right]^2}+\frac{\sin^4\theta}{2\left[\frac{B}{A}(1+F)\right]^2},
\end{aligned} \tag{4.23}$$

from which the constant can be dropped to give:

$$\cos(\delta\theta_h-\delta\theta_s) = -\frac{\sin^2\theta}{\frac{B^2}{2A^2}(1+F)^2}+\frac{\sin^4\theta}{\frac{B^2}{2A^2}(1+F)^2}. \tag{4.24}$$

Substituting Eq. (4.22) and Eq. (4.24) into Eq. (4.21) gives:

$$\begin{aligned}
E &= A\left[\sin^2\theta-\frac{\sin^2\theta}{\frac{B}{4A}(1+F)^2}+\frac{\sin^4\theta}{\frac{B}{4A}(1+F)^2}\right]-B\left[-\frac{\sin^2\theta}{\frac{B^2}{2A^2}(1+F)^2}+\frac{\sin^4\theta}{\frac{B^2}{2A^2}(1+F)^2}\right] \\
&= \left[A-\frac{4A^2}{B(1+F)^2}+\frac{2A^2}{B(1+F)^2}\right]\sin^2\theta+\left[\frac{4A^2}{B(1+F)^2}-\frac{2A^2}{B(1+F)^2}\right]\sin^4\theta \\
&= \left[A-\frac{2A^2}{B(1+F)^2}\right]\sin^2\theta+\frac{2A^2}{B(1+F)^2}\sin^4\theta \\
&= \left[A-\frac{2A^2}{B}(1-f)^2\right]\sin^2\theta+\left[\frac{2A^2}{B}(1-f)^2\right]\sin^4\theta.
\end{aligned} \tag{4.25}$$

Evidently, it has been mathematically proven that the core/shell interaction has introduced a higher fourth-order anisotropy term with a coefficient:

$$K_2 = \frac{2A^2}{B}(1-f)^2. \tag{4.26}$$

Also, the coefficient of the second-order anisotropy term, instead of just $A = K_u V_c$, is subsequently modified to become:

$$K_1 = A - \frac{2A^2}{B}(1-f)^2. \tag{4.27}$$

The ratio of the fourth and second-order anisotropy constant, to a first-order approximation, is therefore given by:

$$\begin{aligned} \frac{K_2}{K_1} &= \frac{\frac{2A^2}{B}(1-f)^2}{A - \frac{2A^2}{B}(1-f)^2} = \frac{2A(1-f)^2}{B - 2A(1-f)^2} \\ &\approx \frac{2A}{B}(1-f)^2. \end{aligned} \tag{4.28}$$

The above expressions are perfectly general for a system with a uniaxial anisotropy constant K_1. However, as discussed before FePt also has a small in-plane anisotropy from the local single-site Fe anisotropy. This in-plane anisotropy will become dominant in small-sized systems because of the loss of 2-ion anisotropy at the surface, most notably such as in the extreme core-shell case $R = 0.05$, and therefore must be accounted for. In the following, these effects are treated in an approximate way which is appropriate for straightforward calculations for high-symmetry geometries.

4.4.2 Approximate introduction of the in-plane single-site anisotropy

Assume that the surface layer of the core loses the 2-ion anisotropy due to the loss of Pt neighbours from the next-immediate atomistic layer of the shell only. Then, introduce an in-plane single-site anisotropy K_{ip} into Eq. (4.15). The energy, which for simplicity still retains the unmodified K_u term, can be rewritten as:

$$E = [K_u(V_c - aA_{cs}) - K_{ip}V_c]\sin^2(\theta + \delta\theta_h) - \frac{JA_{cs}}{a^2}\cos(\delta\theta_h - \delta\theta_s). \tag{4.29}$$

It can be reasonably assumed that, to a first approximation, $\delta\theta_h$ and $\delta\theta_s$ are still given by Eq. (4.18). Following the same procedure for previous case without the in-plane anisotropy

results in the energy E of a mathematically similar form:

$$E = [K_u(V_c - aA_{cs}) - K_{ip}V_c]\sin^2\theta + \frac{2\left[K_u(V_c - aA_c) - K_{ip}V_c\right]^2}{B(1+F)^2}\sin^4\theta, \tag{4.30}$$

from which the ratio of the second and fourth-order anisotropy can be calculated as:

$$\begin{aligned}\frac{K_2}{K_1} &\approx \frac{2\left[K_u(V_c - aA_{cs}) - K_{ip}V_c\right]}{B(1+F)^2} \\ &= \frac{2A}{B(1+F)^2}\left[\left(1 - \frac{aA_{cs}}{V_c}\right) - \frac{K_{ip}}{K_u}\right] \\ &= \frac{2A(1-f)^2}{B}\left(1 - \frac{aA_{cs}}{V_c} - \frac{K_{ip}}{K_u}\right).\end{aligned} \tag{4.31}$$

A remark can be made that the addition of the in-plane anisotropy and the reduction of 2-ion anisotropy due to surface neighbour loss has therefore induced an extra "conversion" factor, in form of the second bracket in the final expression of Eq. (4.31), in comparison to the original Eq. (4.28). Note that the in-plane anisotropy component for simplicity has been introduced in an approximate form in order to allow a reasonable calculation of the modified second and fourth-order terms based on the geometry of the system. In the following, expressions for the main parameters for high symmetry cases will be presented. Furthermore, the general geometry-independent formulation will be finalised in which the system parameters transform to the number of spins in the core N_c, the number of interface spins N_{int}, and the total number of spins in the system N_{tot}. In the latter case the in-plane anisotropy term will be introduced in the exact form.

4.4.3 Analytic calculation of high-symmetry cases

Recall that the magnitude and properties of the fourth-order anisotropy constant are dependent on the system geometry and the analytic model investigated here is based on a realistic core-shell structure of FePt with a faceted structure and competing perpendicular and smaller in-plane anisotropies. The calculations of the values of the material-dependent constants for specific geometries are detailed as follows, with a summary tabulated in Table 4.2. Note that for each case, R remains to be the $L1_0$-phase core-size ratio which indicates the relative thickness of the $L1_0$-phase.

For the 1D Planar-bilayer case with L being the bilayer thickness:

$$\frac{A}{B} = \frac{K_u V_c}{JA_{cs}/a^2} = \frac{K_u(LRA_{cs})}{JA_{cs}/a^2} = \frac{K_u LR}{J/a^2}, \tag{4.32}$$

where the K_2/K_1 maximum occurs at maximum of the function $g(R) = R(1-R)^2$ i.e. at $R = 1/3 \approx 0.333$.

For the 2D Cylinder case with L being the cylindrical base radius:

$$\frac{A}{B} = \frac{K_u V_c}{J A_{cs}/a^2} = \frac{K_u(\pi(LR)^2 h)}{J(2\pi LRh)/a^2} = \frac{\frac{1}{2}K_u LR}{J/a^2}, \tag{4.33}$$

where the K_2/K_1 maximum occurs at maximum of the function $g(R) = R(1-R^2)^2$ i.e. at $R = 1/\sqrt{(5)} \approx 0.447$.

For the 3D Sphere case with L being the sphere radius:

$$\frac{A}{B} = \frac{K_u V_c}{J A_{cs}/a^2} = \frac{K_u(\frac{4}{3}\pi(LR)^3)}{J(4\pi(LR)^2)/a^2} = \frac{\frac{1}{3}K_u LR}{J/a^2}, \tag{4.34}$$

where the K_2/K_1 maximum occurs at maximum of the function $g(R) = R(1-R^3)^2$ i.e. at $R = 1/\sqrt[3]{(7)} \approx 0.523$ which is very close to the maximum location of the simulated core-shell grains at $R \approx 0.5$ seen before in Fig. 4.8.

Geometry	A/B	$(1-f)^2$	K_2/K_1 Maximum	L
Planar bilayer	$(K_u/J)La^2R$	$(1-R)^2$	$R = 1/3 \approx 0.333$	Bilayer thickness
Cylinder	$(K_u/2J)La^2R$	$(1-R^2)^2$	$R = 1/\sqrt{5} \approx 0.447$	Cylinder radius
Sphere	$(K_u/3J)La^2R$	$(1-R^3)^2$	$R = 1/\sqrt[3]{7} \approx 0.523$	Sphere radius
General	$(K_u/J)(N_c/N_{int})$	$(1-N_c/N_{tot})^2$	-	-

Table 4.2 Values of A/B and $(1-f)^2$ for various high-symmetry geometries with L the system size as defined by the geometry. The general case is characterised by N_c and N_{int} the number of core and interface spins respectively.

4.4.4 General geometry-independent formulation

Fig. 4.3 shows a cross-sectional view of the faceted, elongated core-shell grains investigated numerically. Clearly, this core-shell structure cannot be modelled as one of the high-symmetry cases given earlier. Without reference to a specific geometry, the problem can be reformulated in terms of the number of atoms in specific locations as follows. First, the energy given in Eq. (4.15) can be rewritten as:

$$E = k_u N_c \sin^2(\theta + \delta\theta_h) - J N_{int} \cos(\delta\theta_h - \delta\theta_s), \tag{4.35}$$

where the geometry-dependant variables V_c the core volume and $A_c s$ the core/shell interface area have been replaced by the corresponding geometry-independent variables N_c and N_{int} -

which are the number of spins in the core and core/shell interface respectively. The constants A and B now become:

$$\begin{aligned} A &= k_u N_c, \\ B &= J N_{int}, \end{aligned} \tag{4.36}$$

and similarly:

$$\begin{aligned} f &= \frac{N_c}{N_{tot}}, \\ F &= \frac{N_c/N_{tot}}{1 - N_c/N_{tot}}, \end{aligned} \tag{4.37}$$

where N_{tot} is the total number of spins. Substituting these variables into Eq. (4.27), Eq. (4.26), and Eq. (4.28) will result in a new expressions for the second-order anisotropy, the fourth-order anisotropy, and their ratio respectively:

$$K_1 = k_u N_c - \frac{2(k_u N_c)^2}{J N_{int}} \left(1 - \frac{N_c}{N_{tot}}\right)^2, \tag{4.38}$$

$$K_2 = \frac{2(k_u N_c)^2}{J N_{int}} \left(1 - \frac{N_c}{N_{tot}}\right)^2, \tag{4.39}$$

and:

$$\frac{K_2}{K_1} \approx \frac{2 k_u N_c}{J N_{int}} \left(1 - \frac{N_c}{N_{tot}}\right)^2. \tag{4.40}$$

To incorporate the in-plane anisotropy component again, note that $A_{cs} = a^2 N_{int}$ and $V_c = a^3 N_c$ and substitute into Eq. (4.31) to obtain:

$$\frac{K_2}{K_1} \approx \frac{2 k_u N_c}{J N_{int}} \left(1 - \frac{N_c}{N_{tot}}\right)^2 \left(1 - \frac{N_{int}}{N_c} - \frac{k_{ip}}{k_u}\right), \tag{4.41}$$

which completes the analytic model of the fourth-order anisotropy. In the next section, the analytic model recently described will be applied to revisit the simulation results of the FePt core-shell.

4.5 An analysis of simulation results of the FePt core-shell

4.5.1 The canting between the core and the shell magnetisation

The fundamental assumption of the analytic model of the fourth-order anisotropy is the proposition of a canting between the magnetisation of the hard-magnetic core and of the soft-magnetic shell. To verify the existence and magnitude of this canting, the dimensional components of the magnetisation vectors of the entire core-shell system, as well as of the core and of the shell individually are extracted directly from simulation output data. From this, the respective deviation angles between the core magnetisation to the system magnetisation - $\delta\theta_h$ - and between the shell magnetisation to the system magnetisation - $\delta\theta_s$ - can subsequently be calculated via simple trigonometry. The canting ratio $\delta\theta_s/\delta\theta_h$ is then plotted in Fig. 4.13 - in which the canting of the core and shell magnetisation is confirmed to occur. The plot includes analytic fits for both the geometry-dependent case following Eq. (4.18) and the geometry-independent case following Eq. (4.37). Given the faceted shape of the simulated core-shell system, it is unsurprising that the geometry-independent fit matches the data extremely well whilst geometry-dependent fit is seen to deviate from data from $R \geq 0.75$.

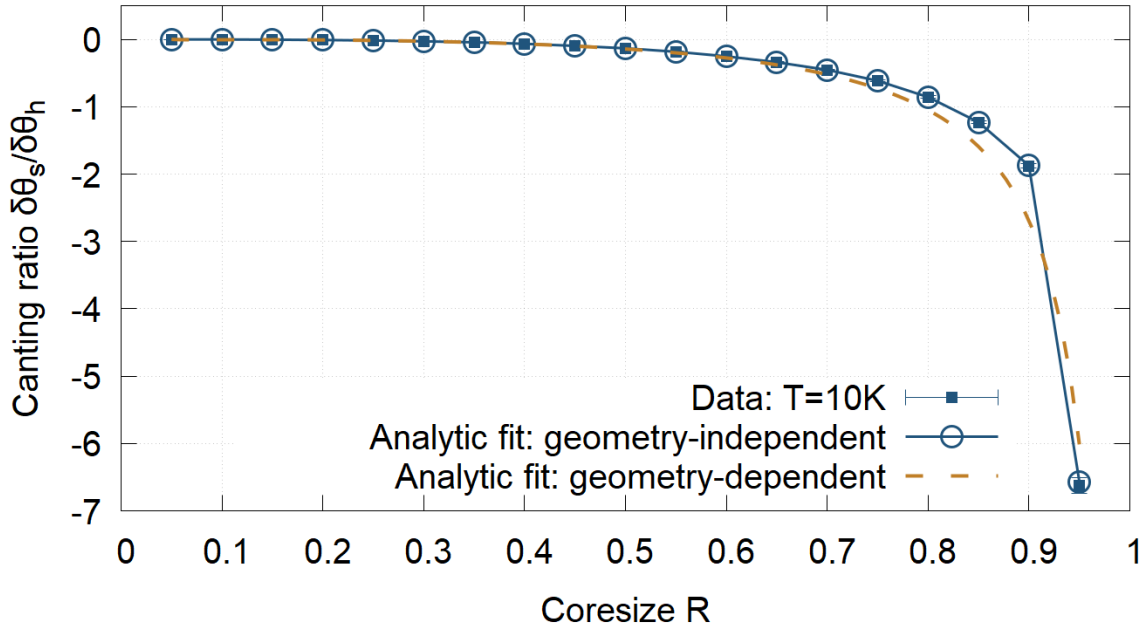

Fig. 4.13 The canting of the core and shell magnetisation with both geometry-dependent and geometry-independent analytic fits shown. It is seen that the geometry-independent fit matches the data extremely well whilst geometry-dependent fit is seen to deviate from data from $R \geq 0.75$.

4.5.2 Representation of the 2-ion anisotropy of FePt and calculation of the second-order anisotropy

FePt has a dominant 2-ion anisotropy mediated by the Pt ions [67] which in principle is quite long-ranged. A simplified representation of this 2-ion anisotropy can be made which involves up to the 3rd-level of nearest-neighbour Fe spins. Since in the simulated core-shell structure the highly disordered $A1$-phase shell has negligible anisotropy, the total anisotropy energy of the core-shell can be written as the sum of contributions over all spins of the highly ordered $L1_0$-phase core including both the 2-ion and the in-plane single-ion k_{ip} terms:

$$E_{anis} = \sum_{i=1}^{N_c} \sum_{j=1}^{3} n_{ij} k_{ij} - k_{ip} N_c, \tag{4.42}$$

where 2-ion anisotropy is described in the summation with the superscript j indicating the level of nearest-neighbours, and n_{ij} and k_{ij} the number of j^{th}-level nearest-neighbours and their corresponding anisotropy contribution respectively. Note that Eq. (4.43) has introduced the exact expression for the anisotropy energy rather than the single-surface-layer approximation as in Eq. (4.31). In the bulk material, for all i, $n_{ij} = 4, 6, 8$ for $j = 1, 2, 3$ respectively and the values k_{ij} are set such that $E_{anis} N_c^{-1}$ is equal to the net 2-ion anisotropy. However, for a finite-size system, because of the loss of coordination at the surface this is no longer the case for all i, and in the analytic model calculations a core size-dependent effective value of uniaxial anisotropy has to be used instead which takes into account the in-plane anisotropy component. This effective uniaxial anisotropy k_u^{eff} is given by:

$$k_u^{\text{eff}}(R) = N_c^{-1}(R) \sum_{i=1}^{N_c(R)} \sum_{j=1}^{3} n_{ij} k_j - k_{ip}. \tag{4.43}$$

where the number of j^{th}-level nearest-neighbours n_{ij} now has to be determined numerically for the specific core-shell system in investigation.

Fig. 4.14 illustrates the variation of the second-order anisotropy constant K_1 per atom against the core size R at low temperature. Two fits are also shown for comparison: first an fit from the analytic model using an effective uniaxial anisotropy k_u^{eff} which is described by Eq. (4.43), and second a fit that excludes the contribution of the $A1$-phase shell which is derived from Eq. (4.38) and Eq. (4.40). The form of the variation is seen to be a combination of both the 2-ion and in-plane single-ion anisotropies. For small core size R, the anisotropy is dominated by the in-plane anisotropy and increases from a small negative value as the larger 2-ion term begins to dominate. Rather than reaching an asymptotic value, the second-order anisotropy increases

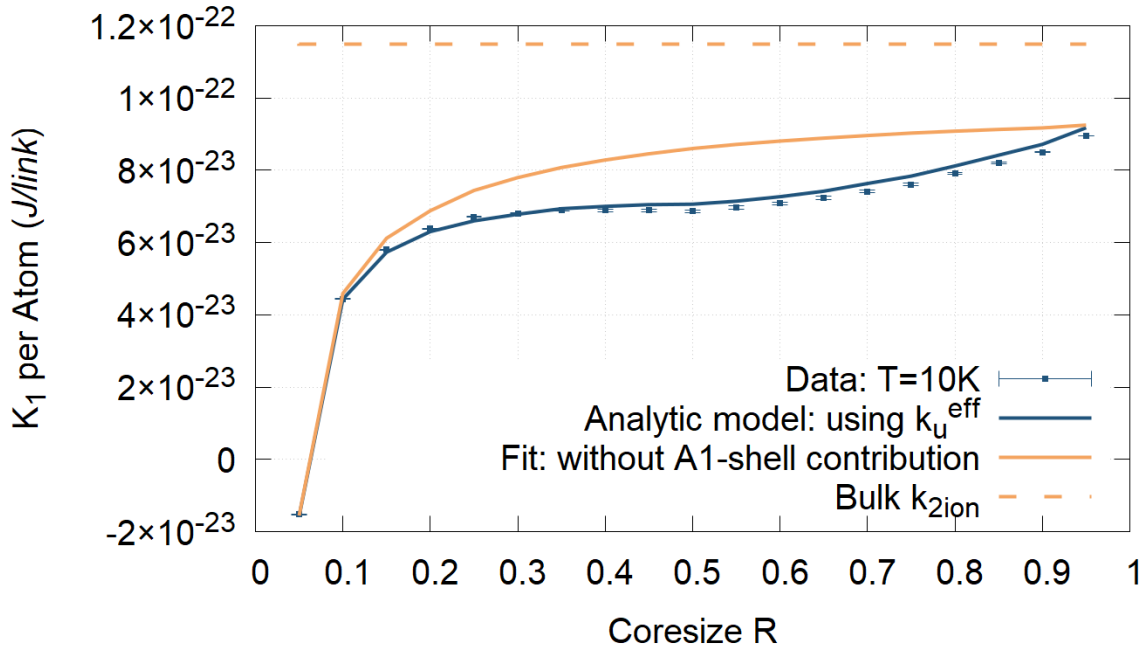

Fig. 4.14 The variation of the second-order anisotropy constant K_1 per atom with the core size R: symbols are the numerically determined data from the atomistic simulations; the solid blue line is the fit by the described analytic model using an effective uniaxial anisotropy k_u^{eff}; the solid brown line is the fit without the contribution of the $A1$-phase shell; and the dashed brown line is the known value for bulk k_{2ion} in literature.

monotonically as the loss of anisotropy at the surface decreases relatively in importance. A further remark can be made is that without the contribution of the $A1$-phase shell, which gives to the fourth-order anisotropy in the simulated core-shell system, the second-order anisotropy K_1 will increase asymptotically, converging to the well-known value of the bulk 2-ion anisotropy k_{ion} of $L1_0$-FePt. Overall, the agreement is excellent, thus validating the formulation of the effective uniaxial anisotropy k_u^{eff} term.

4.5.3 The fourth-order anisotropy and its behaviours

Using the aforementioned definition of the effective uniaxial anisotropy k_u^{eff}, the fourth-order anisotropy from Eq. (4.39) and incorporating the in-plane component can now be expressed as:

$$K_2 = \frac{(k_u^{\text{eff}} N_c)^2}{J N_{int}} \left(1 - \frac{N_c}{N_{tot}}\right)^2 \left(1 - \frac{N_{int}}{N_c} - \frac{k_{ip}}{k_u^{\text{eff}}}\right)^2, \tag{4.44}$$

and consequently, the ratio K_2/K_1 from Eq. (4.41) becomes:

$$\frac{K_2}{K_1} = \frac{(k_u^{\text{eff}} N_c)}{J N_{int}} \left(1 - \frac{N_c}{N_{tot}}\right)^2 \left(1 - \frac{N_{int}}{N_c} - \frac{k_{ip}}{k_u^{\text{eff}}}\right). \tag{4.45}$$

Calculations from the analytic model following Eq. (4.44) and Eq. (4.45) are compared with computational results in Fig. 4.15 and Fig. 4.16 respectively. Fig. 4.15 shows the variation of the the fourth-order anisotropy, per atom, with the core size R. Both analytic and numerical variations are of similar form: non-monotonic with a peak at $R \approx 0.55$. The agreement for $R > 0.5$ is extremely good, whilst for $R < 0.5$ the K_2 values appear to be slightly over-estimated by the analytic model. Nonetheless the overall agreement is highly satisfactory. Similar verdicts are clear by inspection of the data of Fig. 4.16 which shows the dependence of the ratio K_2/K_1 on the core size R. The overall good agreement between the numerical results supports the hypothesis that the fourth-order anisotropy arises from the core/shell spin canting and the exchange energy contribution at the core/shell interface.

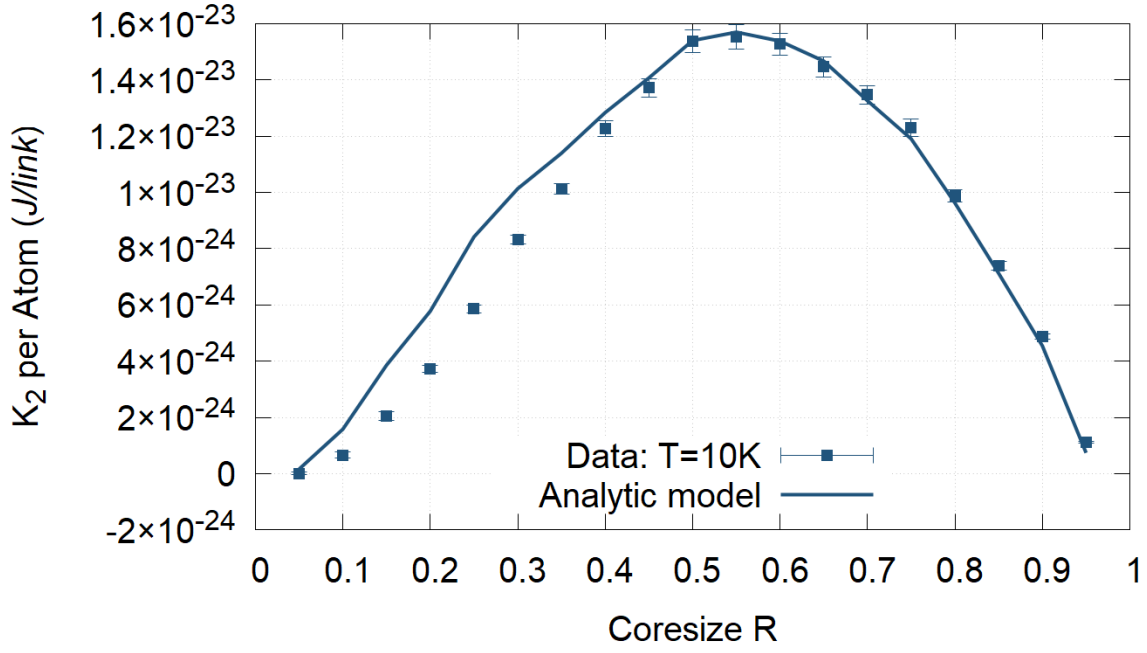

Fig. 4.15 The variation of the fourth-order anisotropy constant K_2 per atom with the core size R: symbols are the numerically determined values from atomistic simulations and the solid line is the predicted analytic fit.

Furthermore, the scaling exponent $2 \lessapprox \beta \lessapprox 3$ of the fourth-order anisotropy K_2 to magnetisation seen before can now be explained as follows. Eq. (4.44) essentially expresses the relation $K_2 \propto (k_u^{\text{eff}})^2/J$ in which it has been established that $k_u^{\text{eff}} \propto (M/M_s)^{2.1}$ - following the

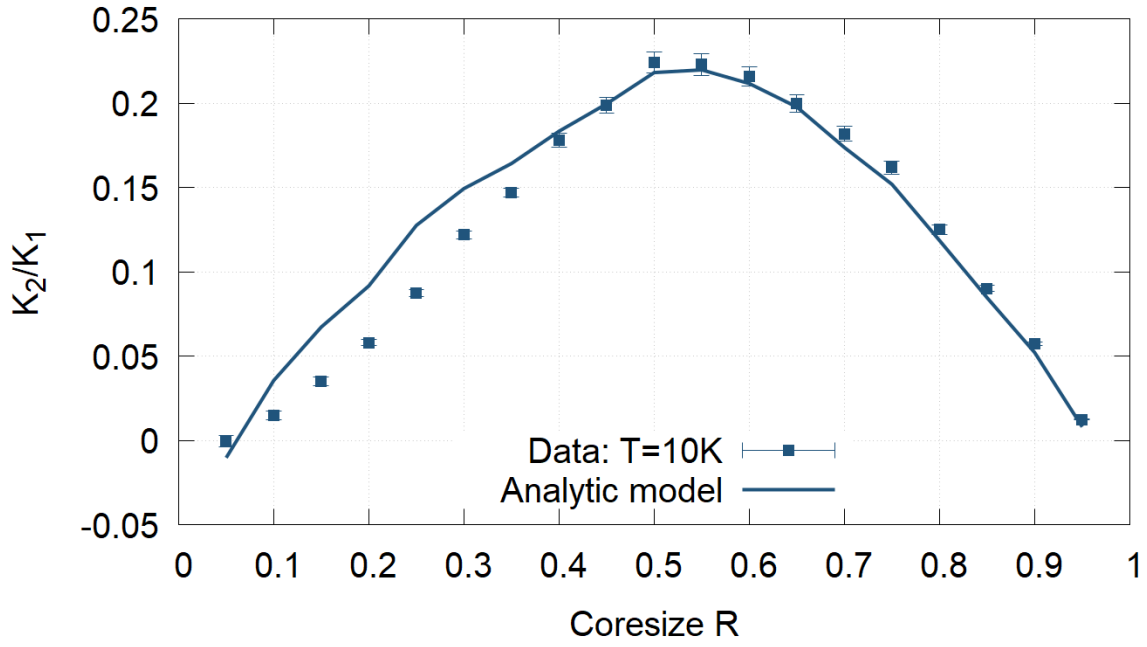

Fig. 4.16 The variation of the K_2/K_1 ratio with the core size R: symbols are the numerically determined values from atomistic simulations and the solid line is the predicted analytic fit.

same well-known scaling relation of the bulk 2-ion anisotropy k_{2ion} - and $J \propto (M/M_s)^2$ via mean-field calculations [64, 121]. The final scaling, therefore, results in $K_2 \propto (M/M_s)^{2.2}$ thus leading to a scaling exponent $\beta \approx 2.2$ in good agreement with computational results obtained from the core-shell simulation. Finally, extreme deviations from the analytic model seen in the two boundary values of core size $R = 0.05$ and $R \geqq 0.90$ can be explained from the inherent peculiarities of their respective grain structures. In the $R = 0.05$ case, the $L1_0$ core is so small that it consists of a single Fe atom which means the 2-ion anisotropy component of the $L1_0$ phase has been completely eliminated, leaving the core with just the negative in-plane single-site local anisotropy of Fe - thus explaining the negative value of K_1/K_1 at $R = 0.05$ seen in Table A.3 of Appendix A. Meanwhile, for the $R \geqq 0.90$ case, the $A1$ shell is so thin that has exactly one or two atomistic layers, hence invalidating the fundamental premise of the analytic calculations which assumes interactions up to the 3rd-level of nearest neighbours. Therefore, as seen in Fig. 4.10, the scaling exponent β of the $R \geqq 0.90$ case was seen to increase exponentially out of the normal $2 \lessapprox \beta \lessapprox 3$ range for other core sizes, albeit still significantly different from the Callen-Callen prediction of $\beta = 10$ for the fourth-order anisotropy.

4.6 Summary

In this Chapter, a comprehensive study of higher-order anisotropy of FePt has been presented via a thorough investigation of a $L1_0/A1$-FePt core-shell system. A non-negligible new fourth-order anisotropy term has been found to exist which exhibits a strong dependence on the system geometry. The origin of this fourth-order anisotropy is ascribed to a combination of the canting of the core and shell magnetisation and of the exchange coupling occurring at the core/shell interface. Additionally, the new fourth-order anisotropy constant is found to scales with $(M/M_s)^{2.2}$, thus conclusively does not conform with the Callen-Callen power law. An analytic model has been formulated to explain the behaviours of this new fourth-order anisotropy from which overall good agreements with simulation data have been achieved. Overall, the findings presented in this Chapter provide substantial insights into a topic that has otherwise been lacking attention. The significance of fourth-order anisotropy of $L1_0$-FePt can potentially translate to an issue of consideration for HAMR-related applications of the material because it is anisotropy that decides thermal stability of the writing medium. With such justification, the core-shell structure and its properties will be carried onto a further investigation of the switching probability of HAMR-applicable grains which will be presented in the next Chapter 5.

5

HAMR switching efficiency in core-shell $L1_0$/A1-FePt grain

Reducing the grain size still remains the main obstacle for the realisation of $L1_0$-FePt for potential applications in Heat-Assisted Magnetic Recording (HAMR) because of reducing thermal stability and, consequently, thermal writability. A specially constructed phase-coupled $L1_0/A1$ core-shell structure has previously been demonstrated to enhance further the already significantly strong magneto-crystalline uniaxial anisotropy of $L1_0$-FePt via the induction of an additional fourth-order anisotropy component. Therefore, in this research we aim to implement the said core-shell structure for a computational investigation of switching efficiency in a simulated HAMR-applicable writing medium. Elongated, faceted cylindrical FePt grains are created with three different configurations in order to account for the effect of finite-size and surface disorder due to the surface segregation of Pt atoms. An external cooling magnetic field and a laser pulse of varied duration replicating the intensive, highly localised heat-dot of a typical HAMR write-head are applied to switch the spins. Simulation results demonstrate that the switching efficiencies of FePt grains of all three tested configurations increase sharply around the Curie temperature and finally saturate at a maximum probability lower than the ideal 100%, which indicates the existence of a noticeable switching error rate. It is found that reducing the grain size and using a shorter laser pulse induce higher switching error rate, which are undesirable for HAMR functioning. However, these effects could be mitigated by surface engineering – in this case the addition of a disorder A1 shell around the ordered $L1_0$ core in order to stabilise the magnetisation of the $L1_0$-phase.

5.1 Motivation

A magnetic-recording writing medium generally consists of many grains of randomly distributed sizes, and the areal density of information bits that can be stored on it is ultimately limited by the grain size. Therefore, the first step to increase areal density is to try to reduce the mean and standard deviation of the grain size distribution [122]. Although $L1_0$-FePt has been attracting significant attention for potential applications in Heat-Assisted Magnetic Recording (HAMR), it still remains a challenging task to reduce grain size because of reducing thermal stability and, consequently, thermal writability. Reducing the grain size has to be compensated by enhancing magnetocrystalline uniaxial anisotropy in order to prevent information loss due to thermally activated magnetisation reversal. In Chapter 4, the phase-coupled $L1_0/A1$-FePt core-shell structure has been demonstrated to exhibit a very large uniaxial anisotropy which is further strengthened by an induced fourth-order anisotropy component. Therefore, it is a natural progression to implement the said core-shell structured FePt grain and examine computationally its switching efficiency in a simulated HAMR-applicable writing media.

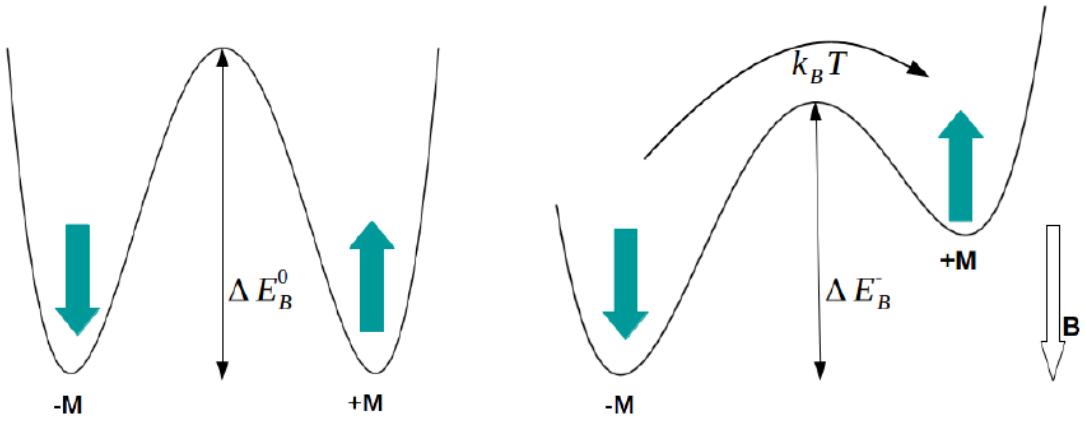

Fig. 5.1 An illustration of the energy barrier: (left) without the presence of an externally applied magnetic field **B**, and (right) with the presence of an externally applied magnetic field. Source: excerpt from [41].

The mechanism of thermally-induced spin switching at high temperatures is illustrated by the energy barrier sketch in Fig. 5.1 which can be briefly explained as follows. In the absence of an externally applied magnetic field and without the application of a heat pulse, a system with uniaxial anisotropy exhibits two energy minima of similar magnitudes, and thus the system can equally likely switch from one minimum state to another. Therefore, the system magnetisation **M** under sufficient thermal excitation can end up in either the negative or positive direction with equal probability. However, this balanced likelihood is lost when an external magnetic field **B** is applied along the negative direction. The presence of such negative

magnetic field reduces the energy barrier from the positively-orientated to the negatively-oriented magnetisation, hence making it easier for the system spins to be flipped over to the negative energy minimum. Consequently, the system magnetisation prefers to be aligned in the negative energy minimum state. The consideration changes again, however, with the addition of a heat pulse. If the peak temperature of the pulse is sufficiently high – which more than often the case in typical HAMR writing since it involves heating up the writing medium close to the Curie temperature of the material – the induced thermal energy can be sufficiently high for the system magnetisation to overcome the larger energy barrier and cross back to the positive energy minimum state. Then, if the subsequent cooling process occurs sufficiently fast – which is achievable in pulses with narrow temperature widths – the system has no time to relax back to the preferred negative energy minimum, thus remaining "blocked" in the positive energy minimum with its magnetisation being oriented in the positive direction as opposed to the negative direction of the externally applied magnetic field **B**. This effect, therefore, results in a reduction in switching probability.

Evans et al. [12] investigated the thermodynamics of HAMR using a simplified case of Heated-Dot Magnetic Recording. This is the limiting case of magnetic recording where HAMR is used to write information on a single magnetic island. In this case it is straightforward to calculate a Bit Error Rate (BER) and use this to investigate the limits of recording density. The formulation of BER for Heated-Dot Magnetic Recording has been proposed by Evans et al. [12] to be related to the thermal equilibrium magnetisation m_e of the system which is given by:

$$m_e = \tanh\left(\frac{\mu\mu_0 H_{wr}}{k_B T}\right), \tag{5.1}$$

where $\mu = M_s V$ is the magnetic moment of the grain with M_s the material saturation magnetisation and V the grain volume, H_{wr} the writing magnetic field from the write transducer, T the temperature, μ_0 the vacuum permeability, and k_B the Boltzmann constant. BER is then mathematically expressed as:

$$BER = \frac{1-m_e}{2} = \exp\left(-\frac{2\mu\mu_0 H_{wr}}{k_B T}\right). \tag{5.2}$$

The existence of the thermally-induced BER has extended the concept of writability, which previously referred to only the magnetic field needed to switch the magnetisation. The thermal writability of the medium can now be defined as the requirement to maintain sufficiently large value of $\left(\frac{\mu\mu_0 H_{wr}}{k_B T}\right)$ in order to avoid thermally driven switching failures and to achieve the desired BER. Since the strength of the externally applied writing field H_{wr} is technologically restricted, the more viable solution to reduce BER is by using material with large magnetic

moment μ; and since increasing the grain volume is undesirable, this requirement effectively translates to finding a material with high saturation magnetisation M_s. The introduction of thermal writability, therefore, has extended the original magnetic trilemma to a quadrilemma. In the case of current HAMR, where information is stored on many grains, the BER is not straightforward and beyond the scope of this Thesis. However, the thermal writability is nonetheless a limiting factor as being investigated here using the switching probability of isolated grains after the HAMR process. Previous studies have shown that magnetic switching in HAMR is constrained by many factors notably the duration of the applied pulse, the strength of the externally applied cooling field, grain size etc. [2, 12, 65, 122–125]. The investigation in this Chapter, therefore, focuses on the viability of core-shell structured sub-10 nm FePt grains for HAMR applications, taking into account not only these factors but also the impact of surface disorder via the effect of Pt surface segregation first introduced and discussed in Chapter 4.

5.2 Simulation methods and settings

5.2.1 Three configurations of FePt grains

The same method to create an elongated, faceted cylindrical core-shell structure which has been described in Chapter 4 is continued to be used for the construction of three different configurations of FePt grains in this Chapter. The height elongation factor of 1.5 as well as the fractional faceting radii of $1.00; 1.05; 1.00$ along the [100], [110] and [111] lattice direction respectively are still retained.

The investigation of switching efficiency is carried out with a deliberate intention to include the effects of grain size - which in Chapter 3 has been shown to amplify the magnetisation loss on the grain surface - as well as the effects of the presence of an $A1$-phase - which in Chapter 4 has been demonstrated to induce an exchange-coupling effect with the $L1_0$-phase. Therefore, three configurations of the simulated FePt grain - which are illustrated in Fig. 5.2 - are carefully chosen as follows. The first configuration is a core-shell grain of 5.0 nm diameter with a core size $R = 0.90$. This core-shell structure is two-phased, consisting of a 4.5 nm $L1_0$-core surrounded by an $A1$-shell of 0.5 nm total thickness - see Fig. 5.2(b). The second configuration is then created by removing the $A1$-shell of the first configuration, thus leaving only a standalone, single-phase $L1_0$ core of 4.5 nm diameter - see Fig. 5.2(a). Lastly, the third configuration is just a slightly enlarged version of the second configuration which again is a standalone, single-phase $L1_0$-core of 5.0 nm diameter - see Fig. 5.2(c). For a convenient reference, the three simulated configurations of FePt grain will henceforth be termed

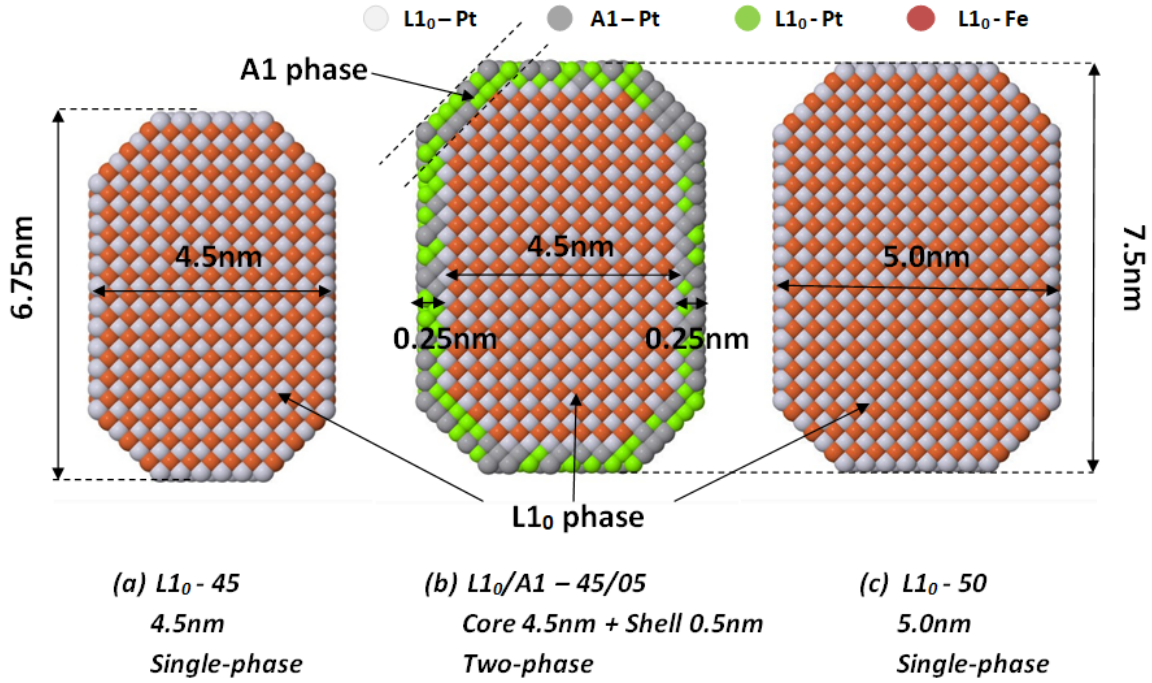

Fig. 5.2 Jmol-visualised cross-sectional sketch of the three simulated configurations of FePt grain: (a) $L1_0-45$; (b) $L1_0/A1-45/05$; and (c) $L1_0-50$. Pt atoms are coloured white ($L1_0$-phase) and light grey ($A1$-phase); Fe atoms green ($A1$-phase) or brown ($L1_0$-phase).

"$L1_0/A1-45/05$", "$L1_0-45$", and "$L1_0-50$" respectively. These three grain configurations allow for many useful cross-comparisons to be made: the effect of adding an $A1$-shell can be examined between the $L1_0/A1-45/05$ and $L1_0-45$, the effect of size between the $L1_0-45$ and $L1_0-50$, and the effect of two-phase versus single-phase between the $L1_0-50$ and $L1_0/A1-45/05$ both of which have the same grain volume but different phase-compositions. The temperature-dependent behaviours of magnetisation $M(T)$ of the three grain configurations are compared in Fig. 5.3. In case of the $L1_0/A1-45/05$ configuration, the magnetisation of the $L1_0$-core - $M_{core}(T)$ - is also plotted which, because of the induced exchange-coupling effect with the low-magnetisation $A1$-shell consistent with results in Chapter 4, is shown to exhibit higher magnetisation than that of the entire grain.

5.2.2 Application of a laser pulse and an external magnetic field

A VAMPIRE-generated laser pulse which imitates an intensive, highly localised heat-dot of a typical HAMR write-head is applied to switch the spins in the core-shell grains, which initially are set to align to the [001] lattice direction along the easy axis of the $L1_0$-phase, for very short duration of time. This very short duration of time is controlled by the cooling time parameter

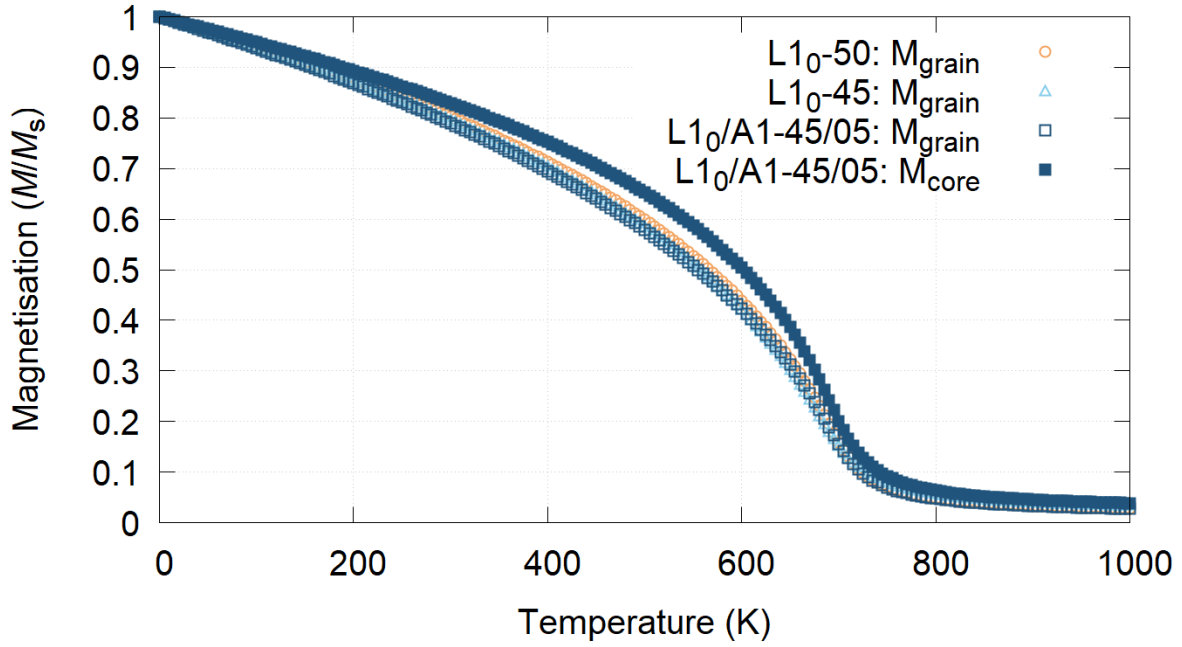

Fig. 5.3 The Magnetisation $M(T)$ of each FePt-grain configuration. Note that for the $L1_0/A1-45/05$ configuration the $M_{core}(T)$ is also plotted which because of the coupling effect with the $A1$ shell shows a higher magnetisation.

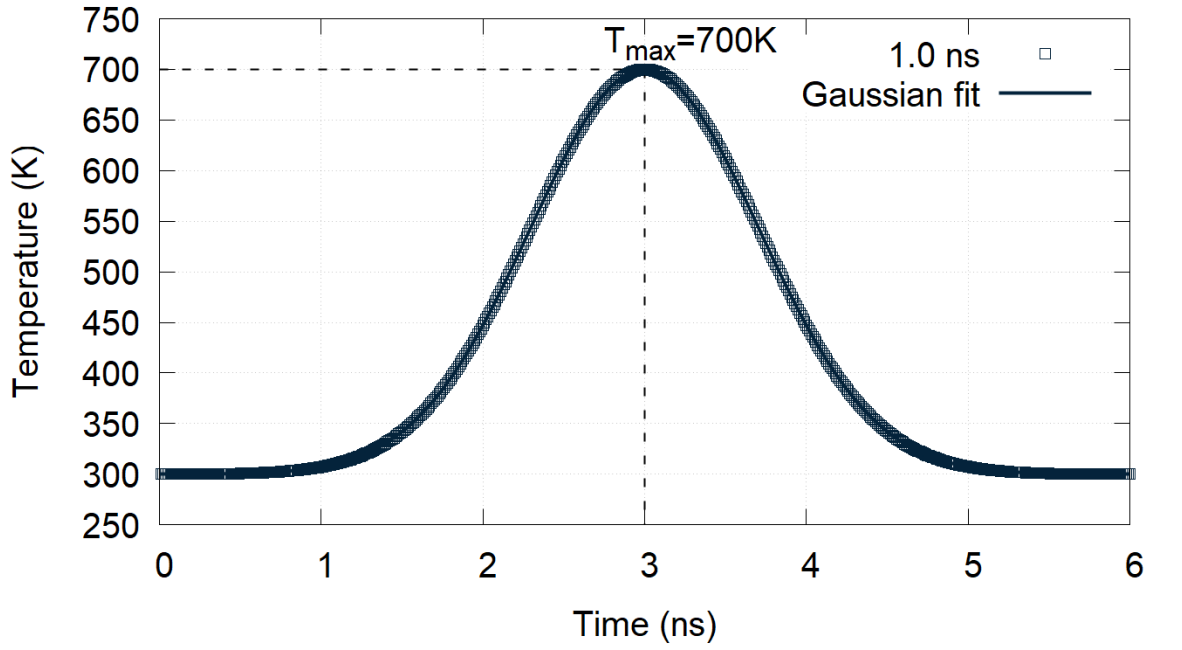

Fig. 5.4 A sampled temperature profile of a laser pulse of 1.0 ns cooling time and $T_{max} = 700$ K with Gaussian fit.

τ. The values of cooling time of the laser pulse in this investigation are initially set to 0.2 ns and 0.5 ns, and then later it is increased to 1.0 ns. The temperature profile of the laser pulse assumes a Gaussian distribution shape consistent with previous studies [123, 125–127] which can characterised by the equation:

$$T(t) = 300 + (T_{max} - 300)\exp\left[-\frac{(t-3\tau)^2}{\tau^2}\right], \tag{5.3}$$

where the constant 300 K refers to the initial ambient temperature when the laser pulse has not been applied, and T_{max} is the peak temperature of the laser pulse which in simulations is assigned to vary from 400 K to 800 K in 10 K steps. This Gaussian temperature profile reaches the peak temperature when $t = 3\tau$. During the application of the heating laser pulse, a field cooling process is implemented via an external magnetic field **B** of magnitude $|\mathbf{B}|$ = 0.8 Tesla which is applied along the $[00\bar{1}]$ lattice direction - i.e. against the initial magnetisation of the grain [125]. The laser pulse will last for a duration of 6 times the corresponding cooling time. A sampled temperature profile of a laser pulse having $\tau = 1.0ns$ and $T_{max} = 700K$ with Gaussian fit following Eq. (5.3) is illustrated in Fig. 5.4.

In order to determine whether after the application of the laser pulse the spins in a simulated grain have switched or not, it is required to perform a check if the orientation of the z-component of the grain magnetisation - M_z - has changed. Initially the spins are orientated along the [001] lattice direction thus M_z assumes positive values. At the very end of the duration of the laser pulse, if the final orientation of M_z turns negative then the spins are concluded to have been switched. Extra emphasis has to be given that for an accurate identification of switching, the check must be done at the exact end of the laser pulse. During the laser pulse, an effect called back-switching may occur in which M_z may flip multiple times, especially at temperatures close to the Curie temperature T_C of the grain, but only the final orientation of M_z at the very end of the laser pulse will be the deciding factor. Examples of switching and non-switching cases with and without instances of back-switching are illustrated in Fig. 5.5.

The laser pulse is applied with three different cooling times, τ = 0.2 ns; 0.5 ns; 1.0 ns. At each cooling time, the peak temperature is varied between 400 K and 800 K in 10 K steps. At each value of the peak temperature, the simulation is repeated for $N = 100$ trials with each time the outcome being recorded as "1" if the spins have switched or as "0" if the spins have not switched. The switching probability P, therefore, statistically takes form of a binomial distribution and can be calculated by dividing the number of switched spins by the number of

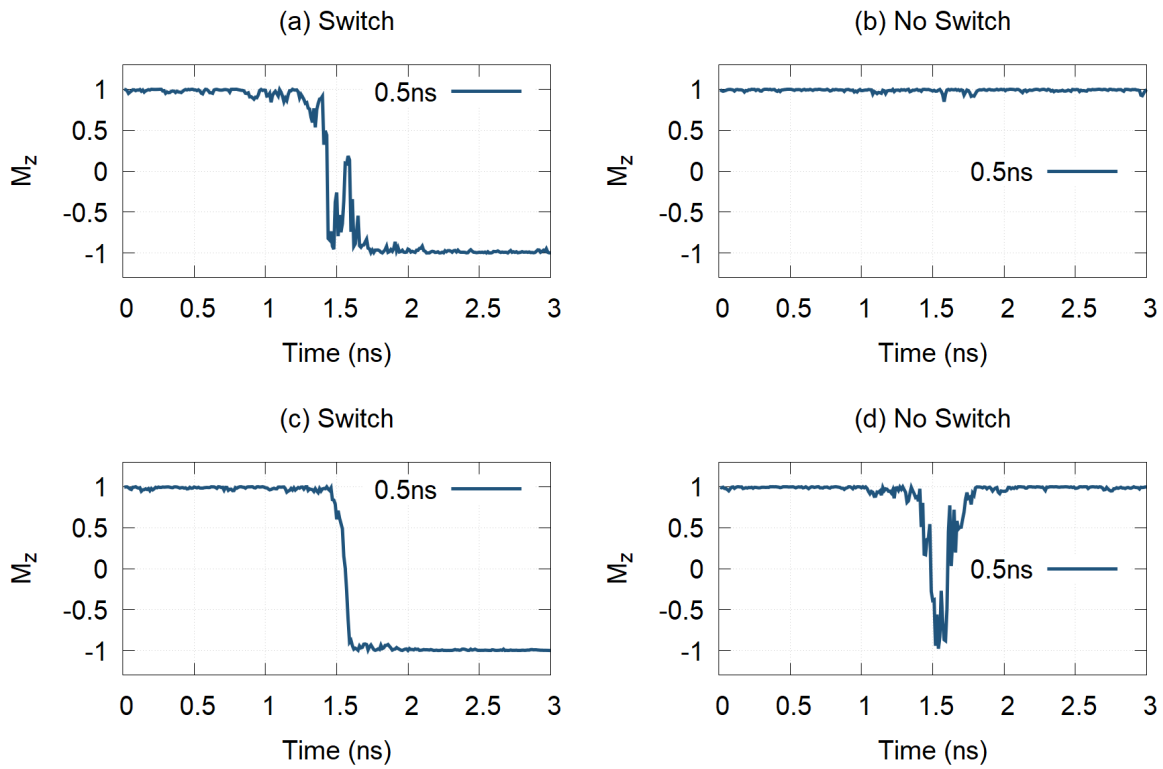

Fig. 5.5 Examples of switching and non-switching after the application of a laser pulse of 0.5 ns cooling time: in (a) and (c) the spins have switched; in (b) and (d) the spins have not switched. Note in (a) and (d) back-switching occurs multiple times during the duration of the laser pulse but it does not change the final state of the spins.

total trials $N = 100$ with an uncertainty ΔP given by:

$$\begin{aligned} P &= \frac{N_{\text{switched}}}{N} = \frac{N_{\text{switched}}}{100}, \\ \Delta P &= \frac{\sigma}{\sqrt{N}} = \frac{\sigma}{10}, \end{aligned} \tag{5.4}$$

where σ is the standard deviation of the switching probability distribution. Obviously, the achievable switching probability described by Eq. (5.4) takes numerical values from 0 to 1.

5.2.3 Temperature rescaling

The investigation in this Chapter aim to imitate the real conditions of a grain in a HAMR-applicable writing media. Therefore, it is necessary to modify the behaviour of the magnetisation curves $M(T)$ obtained from atomistic simulation to be closer to experimental data in order to enable more quantitative predictions of the temperature-dependent magnetisation. To

achieve this purpose, temperature rescaling - the method which has been discussed in Chapter 2 - is applied to the $L1_0$ phase of each simulated grain configuration - which means to the entire grain of the single-phase $L1_0-45$ and $L1_0-50$ but only to the $L1_0$-core of the two-phase $L1_0/A1-45/05$. It has to be noted that temperature rescaling cannot be applied to the $A1$ phase yet because of a lack of referable experiment data in literature which is prerequisite for the estimation of the scaling exponent of the $A1$ phase.

Temperature rescaling in VAMPIRE requires the input of two parameters: the Curie temperature T_C obtained from atomistic calculation and a scaling exponent α. The calculation of the Curie temperature follows the same susceptibility-peak method previously described in Chapter 3. The value of Curie temperature for each configuration of the simulated grain, averaged out after 10 trials, are given in Table 5.1. The other parameter, the scaling exponent α, has to be derived from fitting to experiment measurements of the magnetisation. Unfortunately, in the case of $L1_0$-FePt, the availability of reliable sources has been rather limited. In these simulations, α is chosen to be $\alpha = 1.75$ which is estimated from Thiele et al. [118] and Okamoto et al. [66] and consistent with previous computational studies [127]. The application of temperature rescaling modifies the gradient of the temperature-dependent magnetisation curve - an effect illustrated in Fig 5.6 in which the gradients of $M(T)$ in the vicinity of the Curie temperature have become discernibly steeper whilst significantly flatter at low temperatures. For reference, computational data obtained from atomistic simulations will have an indicator "rescaled" attached if temperature rescaling is applied, or "atomistic" if not.

Configuration	T_C(K) of the $L1_0$-phase
$L1_0/A1-45/05$	685
$L1_0-45$	696
$L1_0-50$	693

Table 5.1 The Curie temperature T_C of the $L1_0$-phase of each configuration of the simulated FePt grain.

5.2.4 The Spin Hamiltonian

The Spin Hamiltonian incorporates the same truncated exchange interaction and 2-ion anisotropy models, thus re-assuming the same forms as previously described in Chapter 4, with the only modification being that a non-vanishing field term $\mathcal{H}_{\text{field}}$ representing the contribution of the externally applied magnetic field **B** now has to be included which induces a torque proportional to M_x and M_y. The explicit expressions of the Spin Hamiltonian, which has now been fully

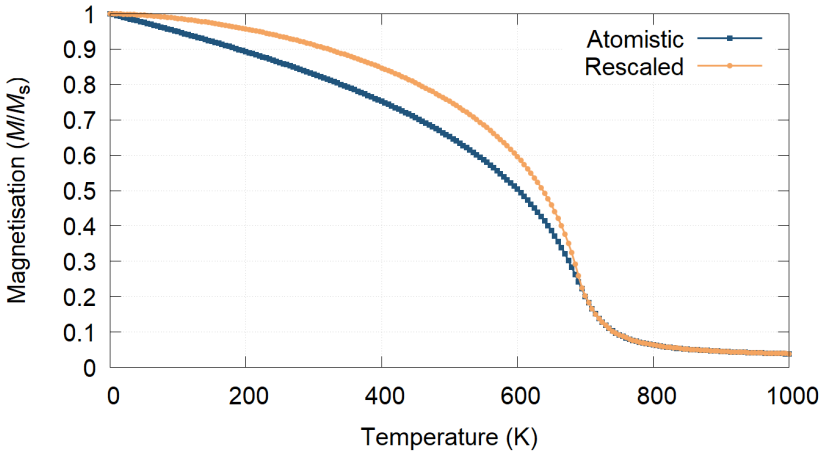

(a) $L1_0/A1-45/05$

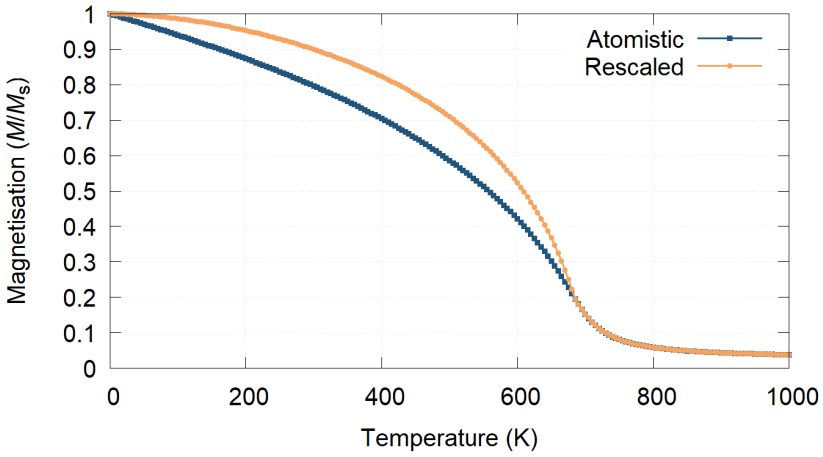

(b) $L1_0-45$

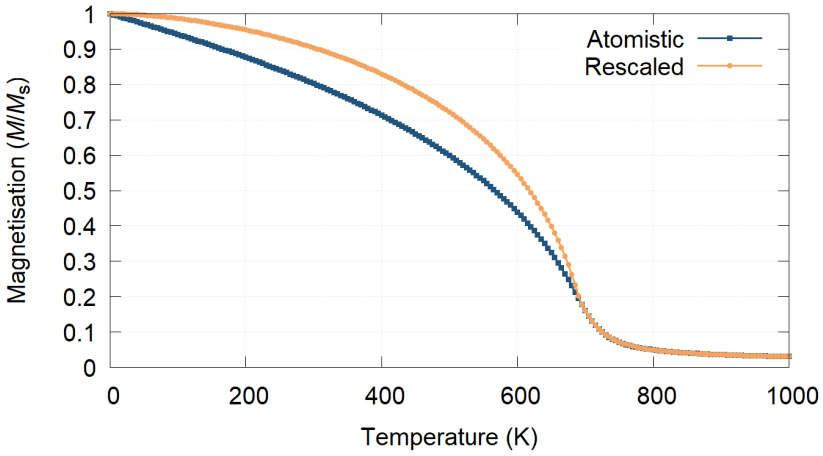

(c) $L1_0-50$

Fig. 5.6 The effect of temperature rescaling on the magnetisation of the $L1_0$-phase of the three FePt-grain configurations. The magnetisation gradient becomes steeper around the T_C region.

expanded to include all three major energy contributors, therefore can be written as follows:

$$\mathcal{H}_{\text{core}} = -\frac{1}{2}\sum_{i,j\in core^*}\left(\hat{\mathbf{S}}_i\right)^T \mathcal{J}_{ij}\hat{\mathbf{S}}_j - k_{loc}^{L1_0}\sum_{i\in core}(\hat{\mathbf{S}}_i^z)^2 - \frac{1}{2}\sum_{i,j\in core}\left(\hat{\mathbf{S}}_i^T\right)^z \mathcal{K}_{2ion}\hat{\mathbf{S}}_j^z, - \sum_{i\in core}\mu_i(\hat{\mathbf{S}}_i\cdot\mathbf{B}), \tag{5.5}$$

and where applicable:

$$\mathcal{H}_{\text{shell}} = -\frac{1}{2}\sum_{i,j\in shell}\left(\hat{\mathbf{S}}_i\right)^T \mathcal{J}_{ij}\hat{\mathbf{S}}_j - k_{loc}^{A1}\sum_{i\in shell}(\hat{\mathbf{S}}_i^z)^2 - \sum_{i\in shell}\mu_i(\hat{\mathbf{S}}_i\cdot\mathbf{B}). \tag{5.6}$$

Here, as before, $\hat{\mathbf{S}}_i$ and $\hat{\mathbf{S}}_J$ are spin unit vectors. The notation $i,j\in core^*$ of the first summation in Eq. (5.5) accounts for exchange interactions not only in the core but also across the core/shell interface as well. The superscript z, where applicable, denotes z-dimension part of the spins. The superscript T, where applicable, denotes the transpose of the spin matrix. The local, single-site anisotropies k_{loc} of the each phase, indicated by the respective superscript, are assigned numerical values of $k_{loc}^{A1} = 0$ [110] and $k_{loc}^{L1_0} = -0.097$ meV/link $= -1.552\times10^{-23}$ J/link [67]. The atomic spin moment μ_i takes value of $\mu_S = 3.23\mu_B$ - with $\mu_B = 9.274\times10^{-24}$ J/T being the Bohr magneton constant, and the externally applied magnetic field $\mathbf{B} = (0,0,-0.8)$ is fixed. $\mathcal{J}_{ij}$ and $\mathcal{K}_{ij}$ are respectively the exchange energy and the 2-ion anisotropy tensors between neighbouring spins (i,j) with components J_{ij}^{α} and K_{ij}^{α} where $\alpha = 1,2,3$ being the neighbouring shell to which the spin belongs. The calculations of J_{ij}^{α} and K_{ij}^{α} have been presented in detail in Chapter 5, and their values are recalled to be given by:

$$\begin{aligned} J_{xyz}^1 &= 2.1428571\times10^{-21}\ J/link \\ J_{xyz}^2 &= 3.0000000\times10^{-21}\ J/link \\ J_{xyz}^3 &= 1.1785714\times10^{-21}\ J/link, \end{aligned} \tag{5.7}$$

and

$$\begin{aligned} K_z^1 &= 1.9026667\times10^{-23}\ J/link \\ K_z^2 &= 1.3590476\times10^{-23}\ J/link \\ K_z^3 &= 7.4747611\times10^{-24}\ J/link. \end{aligned} \tag{5.8}$$

5.2.5 Other parameters

The simulations in this Chapter are performed by the VAMPIRE code using a Metropolis Monte-Carlo integrator which has been discussed in Chapter 2 and first applied in Chapter 3. Magnetic and Monte-Carlo parameters are imported from the core-shell simulations in Chapter 4 with one

Parameter	Notation	Unit	$L1_0$-phase	A1-phase
Damping Constant	ζ		0.05	0.05
Atomistic Spin Moment	μ_s	μ_B	3.23	3.23
Local anisotropy	k_{loc}	J/atom	-1.55×10^{-23}	0
2-ion anisotropy	k_{2ion}	J/atom	2.23×10^{-22}	0
Total Exchange Strength	J^0	J/link	3×10^{-21}	3×10^{-21}
MC Equilibration step			2×10^5	2×10^5
MC Total step			8×10^5	8×10^5

Table 5.2 VAMPIRE parameters for the switching efficiency investigation.

exception that the Gilbert damping constant ζ is now reduced to 0.05 closer to experiment [128]. For a summary, simulation parameters are tabulated in Table 5.2 and a sampled VAMPIRE input is given in Appendix B. The investigation of switching efficiency in this Chapter, therefore, can be viewed as a natural progression from previous Chapters which is built on already established results and combines previously discussed features.

5.3 Results and discussion

Simulations are carried out for three FePt-grain configurations - the $L1_0/A1-45/05$, $L1_0-45$, and $L1_0-50$. For each configuration, a laser pulse of three different cooling times τ of $0.2ns$, $0.5ns$, and $1.0ns$ is applied sequentially. First, the switching probability for each setting is presented both with and without temperature rescaling, from which the overall behaviours and the saturated switching probability in relation to the aforementioned BER can be discussed. It should be noted that since the faster switching cases already showed the effect of temperature rescaling, the $1.0ns$-cooling data were calculated only for the more realistic rescaled case. Next, the effect of varying cooling time of the applied laser pulse as well as of different grain configurations on the saturated switching probability and on the blocking temperature are quantitatively analysed, which will lay the groundwork for future tasks.

5.3.1 Effects of temperature-rescaling on switching behaviour

The switching probability of each setting calculated from computational simulation following Eq. (5.4) is presented in Fig. 5.7, Fig. 5.8, and Fig. 5.9 from which two major observations can be made. First, applying temperature-rescaling is clearly seen to have a significant impact on the switching probability. The temperature-rescaled gradient of the temperature-dependent magnetisation $M(T)$ at lower temperatures, especially around the Curie temperature T_C region, displays a significantly lower blocking temperature - where spin switching starts to happen -

and a much steeper transitional gradient at the T_C vicinity. The non-rescaled atomistic data, on the other hand, display a more jagged, gradual change over wider transitional temperature widths. An implication which follows from this comparison is that rescaled data indicates a requirement of higher peak temperature of the applied laser pulse to achieve comparably high switching probability - thus comparably low switching error rate. Since in literature, comprehensive studies of effect of applying temperature-rescaling in atomistic simulations have been rather lacking, this observation would necessitate further investigations to be validated. Nonetheless, since the rescaled temperature calculations reproduce the experimental $M(T)$ curves this is an important observation for HAMR simulations.

The second observation is that the saturated switching probabilities of all cases do not converge to the ideal 100% even at very high temperatures well above the Curie temperature. This is a direct evidence for the existence of a non-negligible switching error rate in atomistic simulations which has been observed in many previous studies [2, 12, 41, 123, 125, 126, 129]. The post-T_C behaviours of the probability curve are clearly shown to depend on the cooling time of the applied laser pulse and the specific grain configuration, both of which will be analysed in the forthcoming sections. Theoretically, the probability curves can be fit by a cumulative distribution function (CDF) [41, 123] defined as:

$$f(x) = \frac{P_{max}}{2}\left[1 + \text{erf}\left(\frac{x-\mu}{\sigma\sqrt{2}}\right)\right], \tag{5.9}$$

where P_{max} is the saturated switching probability, σ defines the width of the transition and μ the mean transition temperature. Additionally, the error function $\text{erf}(x)$ is given by evaluating the integral:

$$\text{erf}(x) = \frac{2}{\pi}\int_0^z \exp(-t^2)dt. \tag{5.10}$$

In the ideal case where back-switching is negligible, the saturated switching probability P_{max} should reach 100% with a narrow transition width. In fact, thermal and finite-size induced effects lead to a relatively wide transition of 15 K - 30 K and the switching probability saturating to less than the ideal 100% - both these properties have been fully reproduced in Fig. 5.7, Fig. 5.8, and Fig 5.9.

5.3.2 Effects of cooling time on switching behaviour

The effects of varying the cooling time t_{cool} of the applied laser pulse, for a convenient comparison, are demonstrated in Fig. 5.10, Fig. 5.11, and Fig. 5.12 for the $L1_0/A1-45/05$, $L1_0-45$, and $L1_0-50$ grain configuration respectively. In any setting, the same conclusion is reached that increasing cooling time improves switching probability by a significant amount.

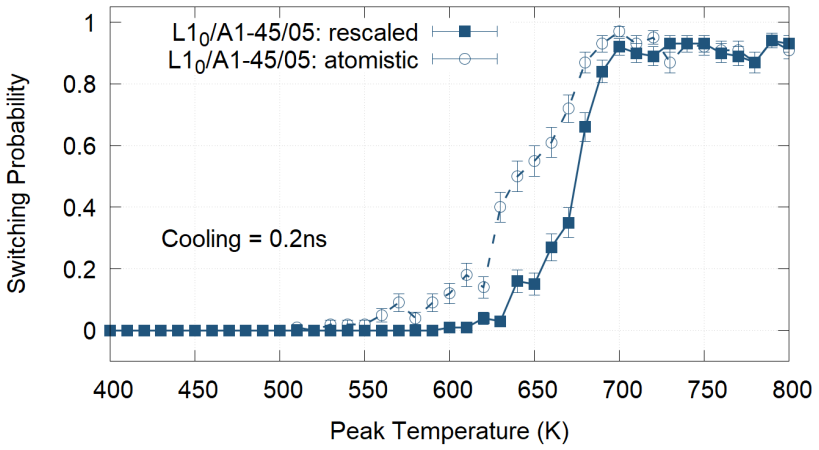

(a) $L1_0/A1-45/05$

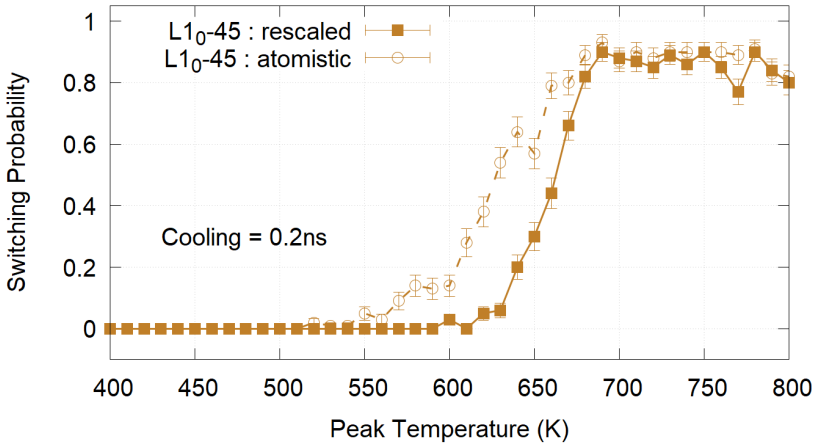

(b) $L1_0-45$

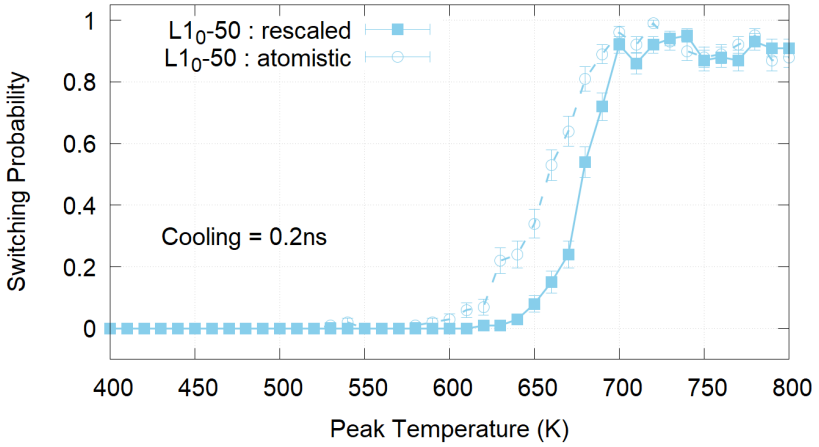

(c) $L1_0-50$

Fig. 5.7 Switching probabilities of three FePt-grain configurations when the laser pulse is applied with cooling time $\tau = 0.2$ ns: (a) $L1_0/A1-45/05$, (b) $L1_0-45$, and (c) $L1_0-50$. Completed "rescaled" and "atomistic" data-sets are shown for comparison.

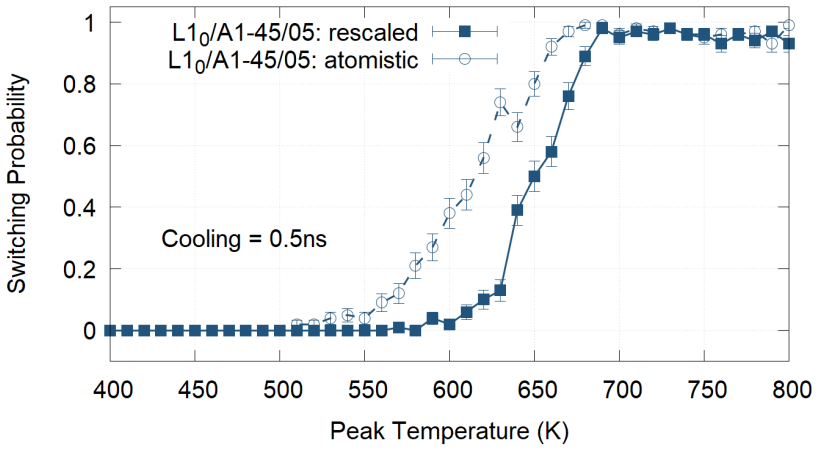

(a) $L1_0/A1-45/05$

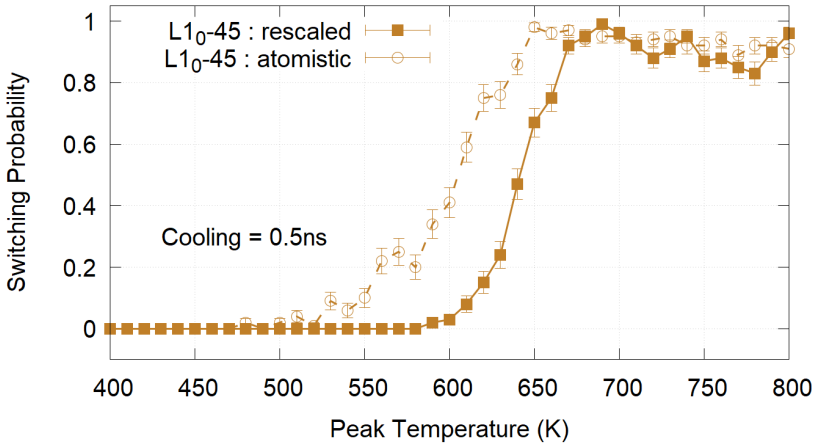

(b) $L1_0-45$

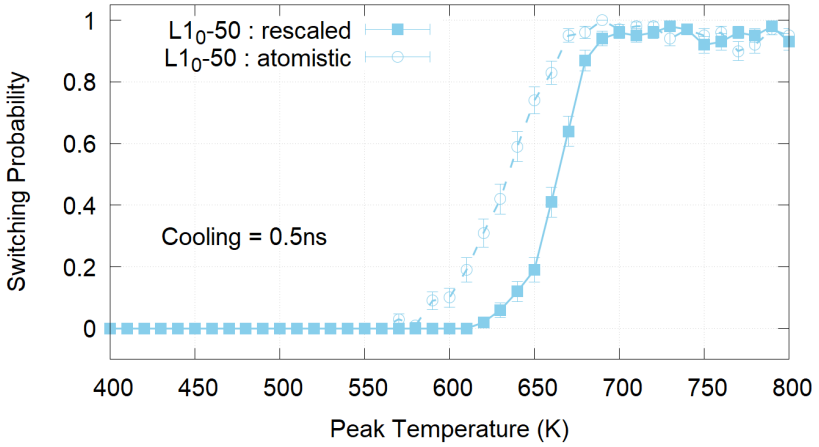

(c) $L1_0-50$

Fig. 5.8 Switching probabilities of three FePt-grain configurations when the laser pulse is applied with cooling time $\tau = 0.5$ ns: (a) $L1_0/A1-45/05$, (b) $L1_0-45$, and (c) $L1_0-50$. Completed "rescaled" and "atomistic" data-sets are shown for comparison.

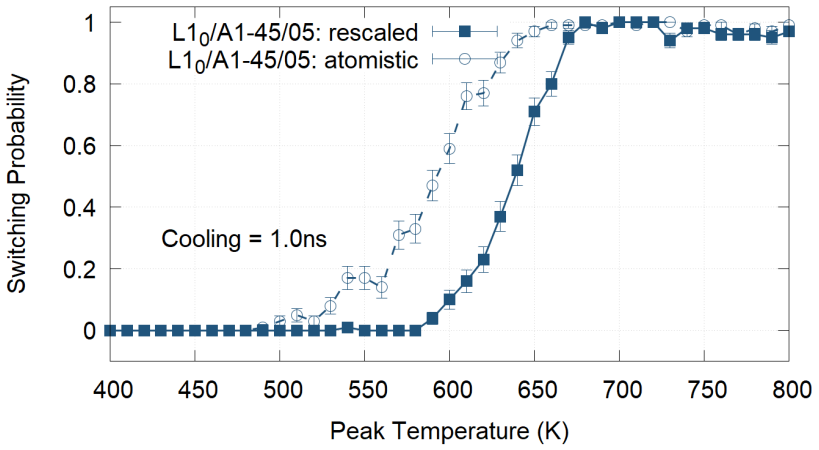

(a) $L1_0/A1-45/05$

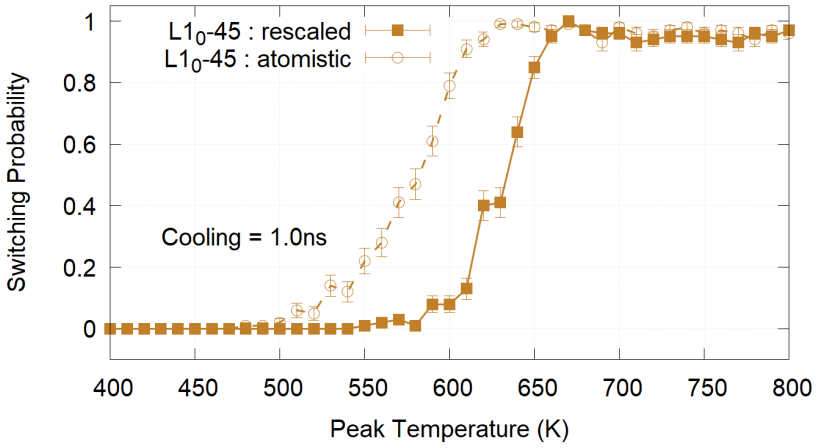

(b) $L1_0-45$

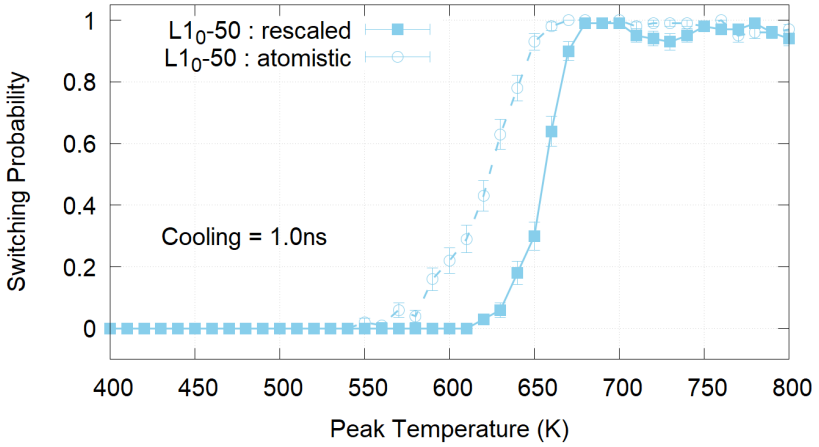

(c) $L1_0-50$

Fig. 5.9 Switching probabilities of three FePt-grain configurations when the laser pulse is applied with cooling time $\tau = 1.0$ ns: (a) $L1_0/A1-45/05$, (b) $L1_0-45$, and (c) $L1_0-50$. Completed "rescaled" and "atomistic" data-sets are shown for comparison.

Heating using laser pulse with longer cooling time is shown to not only push the achievable saturated probability closer to the ideal 100%, thus reducing switching error rate, but also to minimise post-transition fluctuations, hence stabilising the final switching error rate. This conclusion is consistent with previous studies [125, 41, 129]. Physically, longer cooling times leave more time for the spins to relax back to the correct state, thus lowering the chance of being blocked in the wrong state. However, unfortunately, the use of a longer-time laser pulses is against the progression of HAMR which naturally aims for achieving faster writing time. In order to find a solution to this dilemma, it is necessary to take into consideration the effects of grain configurations on switching behaviour.

5.3.3 Effects of grain configurations on switching behaviour

The effects of grain configurations on switching behaviours, for convenient comparison, are illustrated in Fig. 5.13 and 5.14 for rescaled and non-rescaled atomistic data respectively. It can be seen for all tested cooling times that out of all three simulated grain configurations, the $L1_0-45$ exhibits the worst switching behaviour in terms of both the saturated switching probability and post-T_C switching stability. Since this configuration is a bare $L1_0$-core of smallest size, finite-size effects are, as having been demonstrated previously in Chapter 3, the strongest. The most obvious remedy to finite-size effects, consistent with results in Chapter 3, is simply to increase the grain size. The effectiveness of this solution is confirmed by data of the $L1_0-50$ configuration which demonstrate discernibly improved switching behaviour. More remarkably, a still better alternative is observed in the remaining $L1_0/A1-45/05$ configuration which is found to exhibit the best switching behaviour of all three tested configurations. The implication, consequently, seems to be that adding a 0.5 nm-thick layer of $A1$-phase seems to be more effective than adding an equivalent 0.5 nm-thick layer of $L1_0$-phase. The presence of an $A1$-shell, therefore, seems to "protect" and stabilise the magnetisation order of the $L1_0$ core more effectively via the interface-induced exchange-coupling effect already discussed in Chapter 4, thus resulting in a more appreciable improvement of the overall switching behaviour.

5.3.4 Effects of grain configurations on the blocking temperature

Fig. 5.13 and Fig. 5.14 also present another interesting observation in regard to the blocking temperatures exhibited by the three grain configurations. The blocking temperature T_B derived from Néel-Arrhenius equation [27] is expressed as:

$$T_B = \frac{KV}{k_B \ln\left(\frac{\tau_m}{\tau_0}\right)}, \tag{5.11}$$

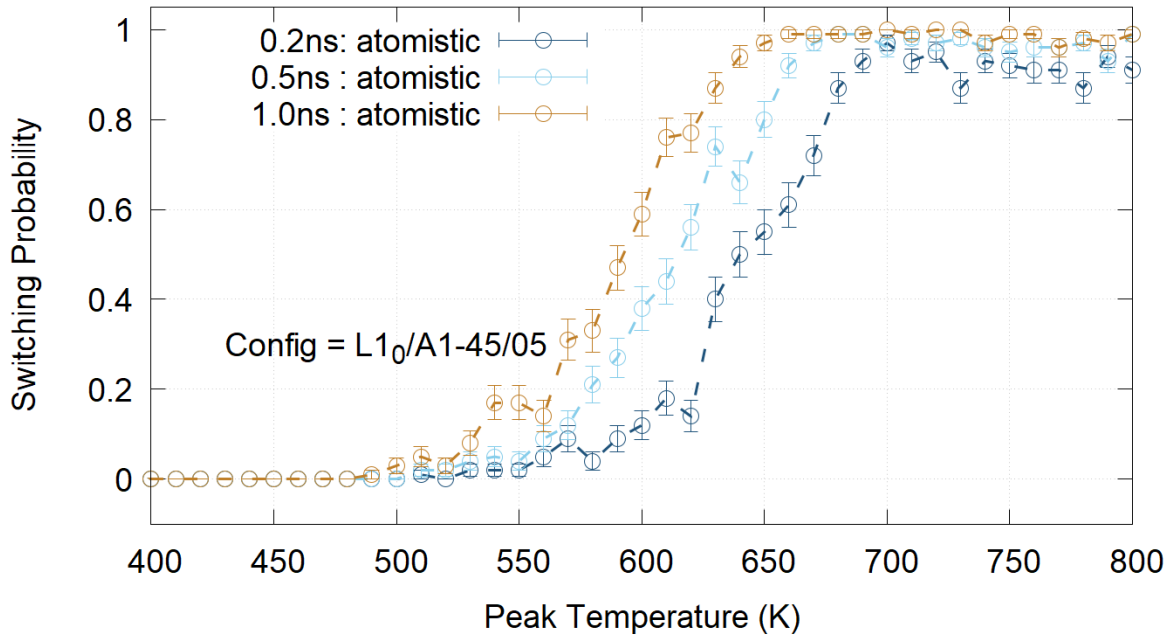

(a) Without temperature-rescaling

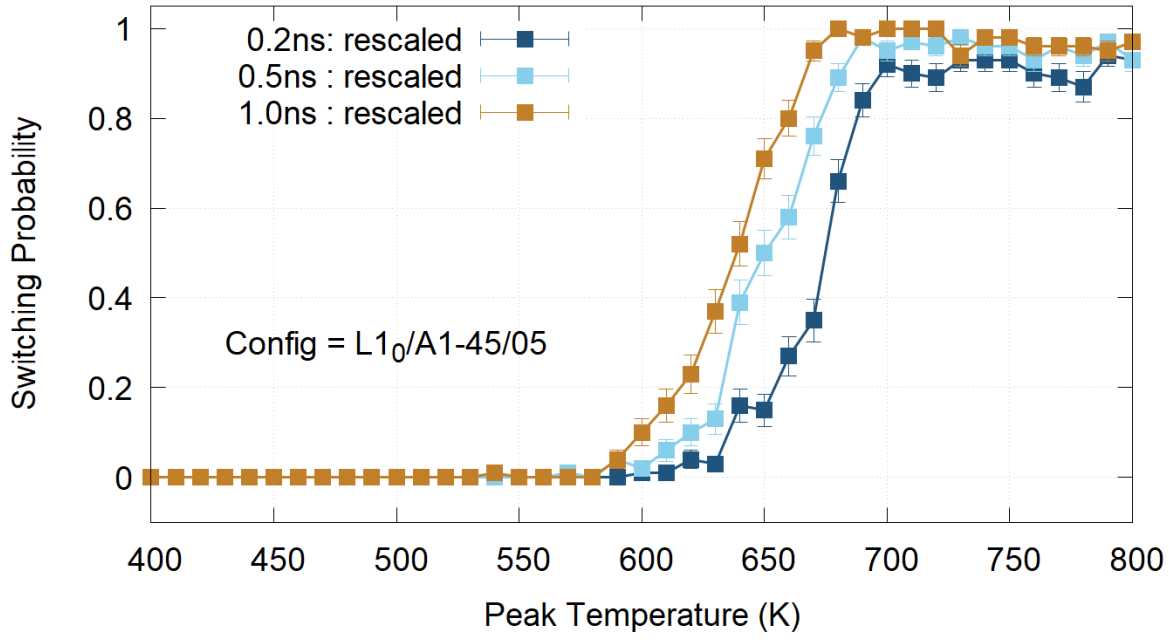

(b) With temperature-rescaling

Fig. 5.10 The impact of varying cooling time of the applied laser pulse in the $L1_0/A1-45/05$ grain configuration: (a) atomistic data; and (b) temperature-rescaled data.

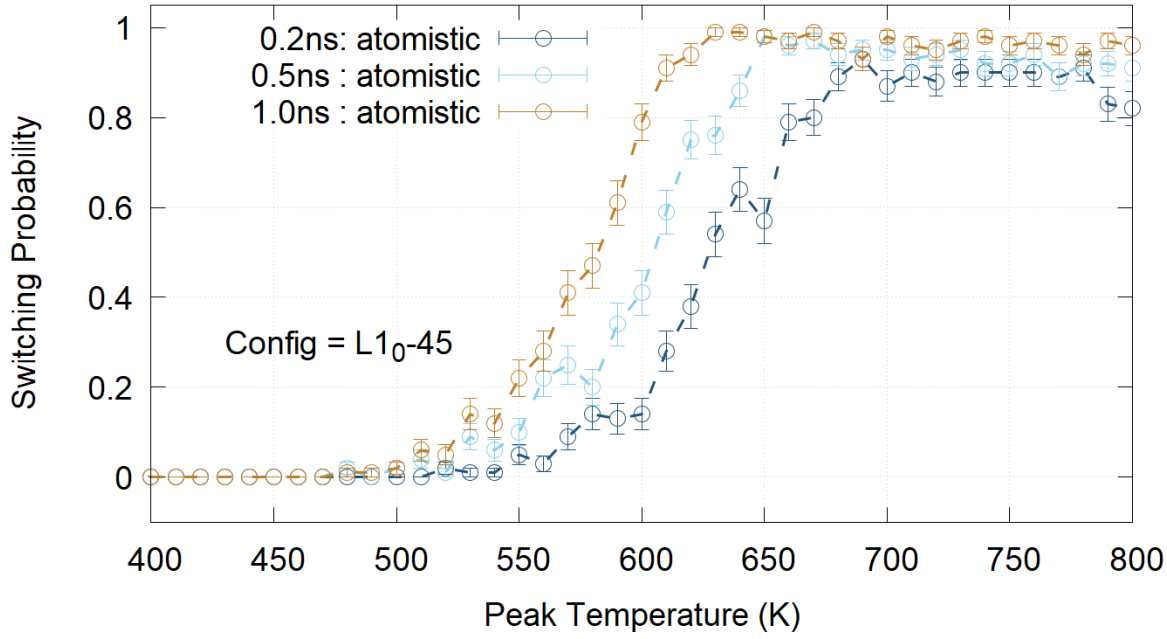

(a) Without temperature-rescaling

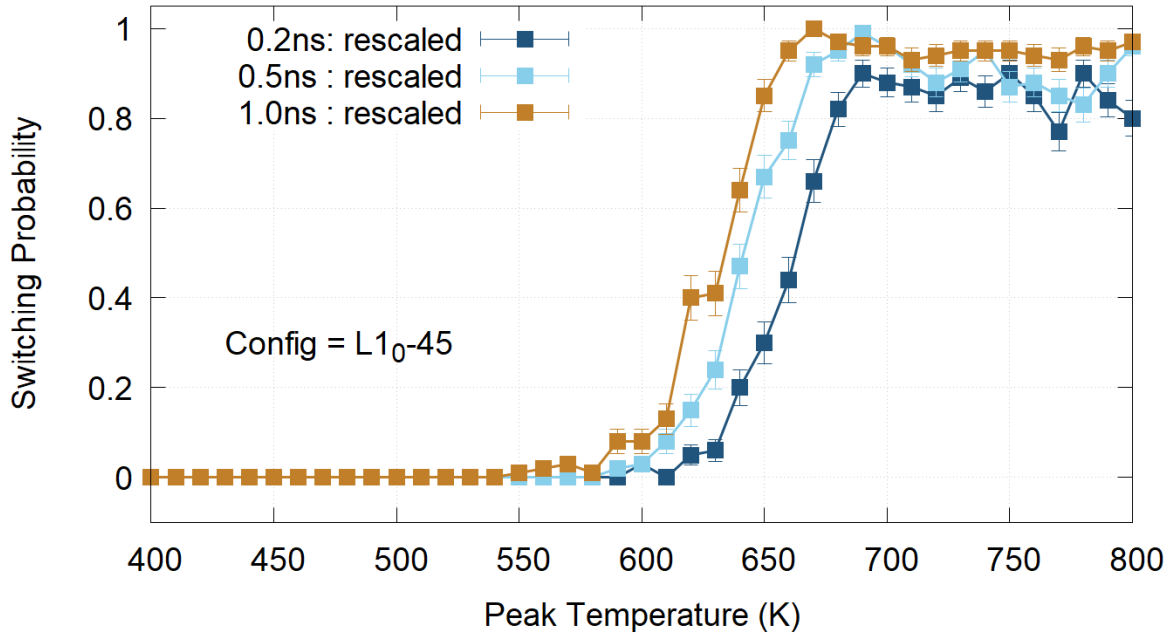

(b) With temperature-rescaling

Fig. 5.11 The impact of varying cooling time of the applied laser pulse in the $L1_0 - 45$ grain configuration: (a) atomistic data; and (b) temperature-rescaled data.

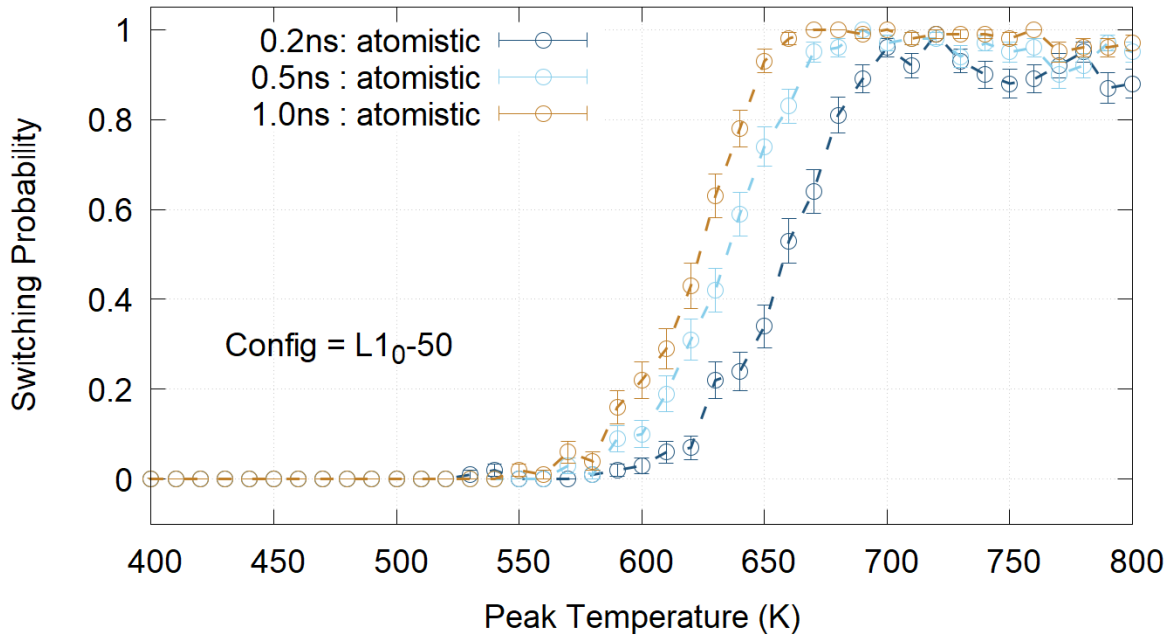

(a) Without temperature-rescaling

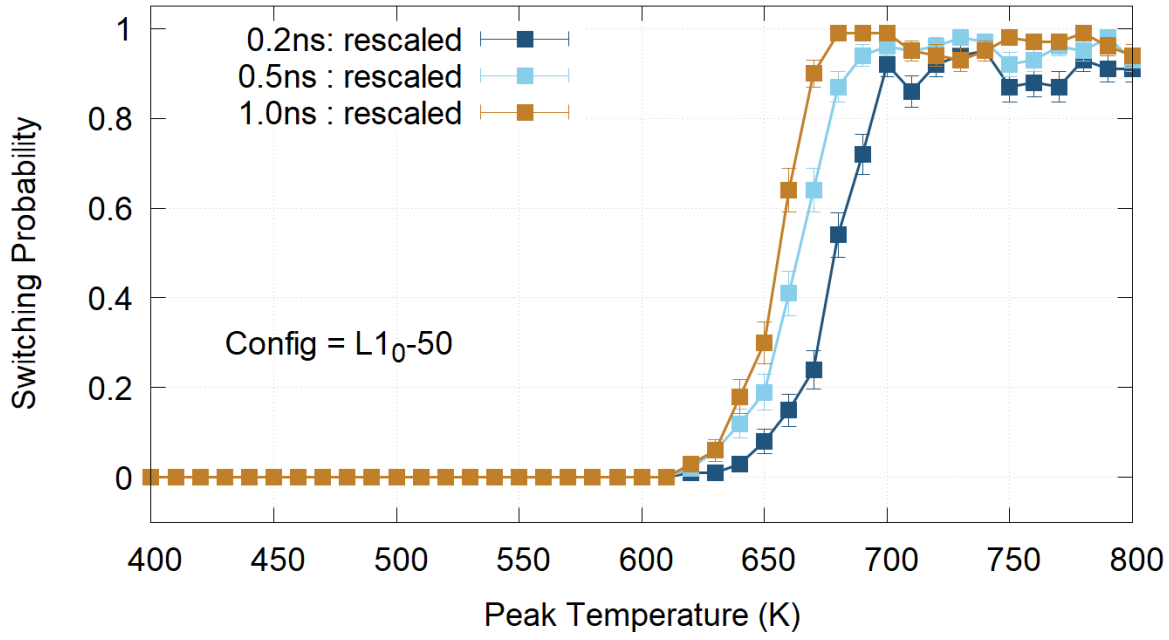

(b) With temperature-rescaling

Fig. 5.12 The impact of varying cooling time of the applied laser pulse in the $L1_0 - 50$ grain configuration: (a) atomistic data; and (b) temperature-rescaled data.

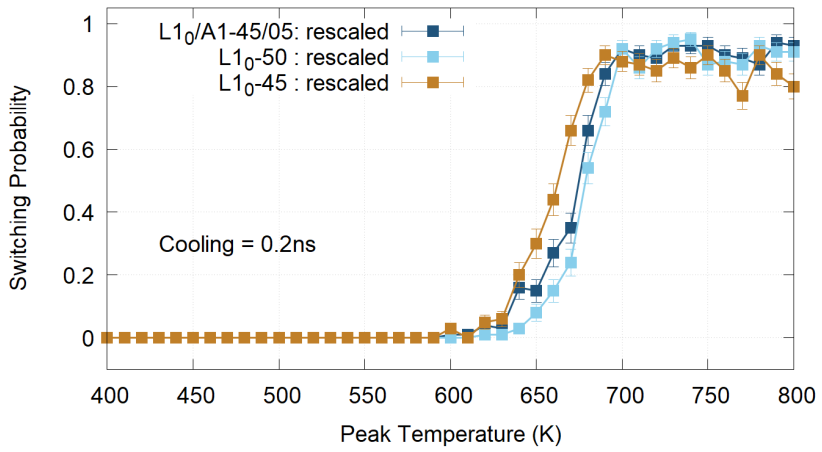

(a) $t_{cool} = 0.2ns$

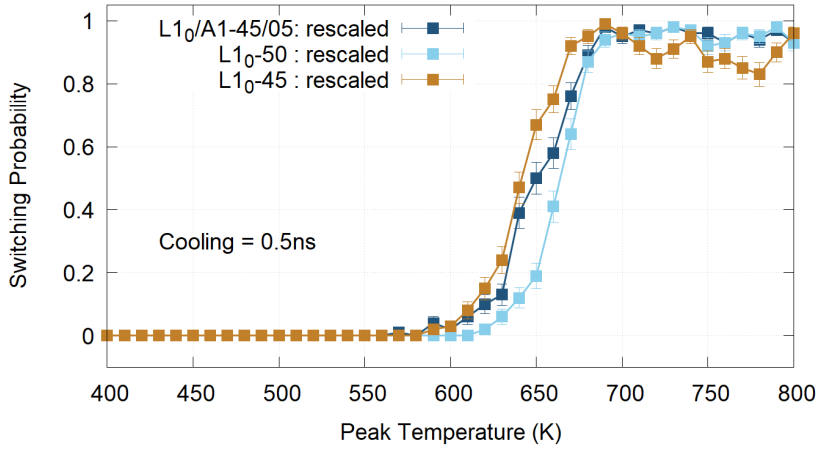

(b) $t_{cool} = 0.5ns$

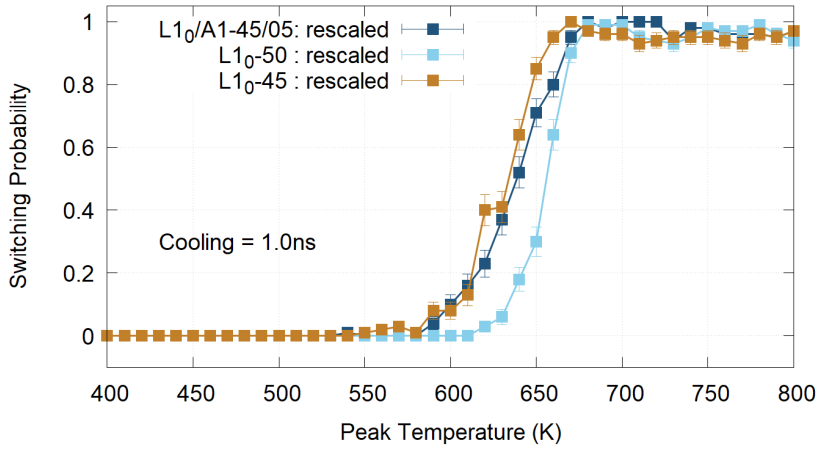

(c) $t_{cool} = 1.0ns$

Fig. 5.13 The effect of grain configurations on the switching probability for varying cooling time of (a) 0.2 ns, (b) 0.5 ns, and (c) 1.0 ns. Data are temperature-rescaled.

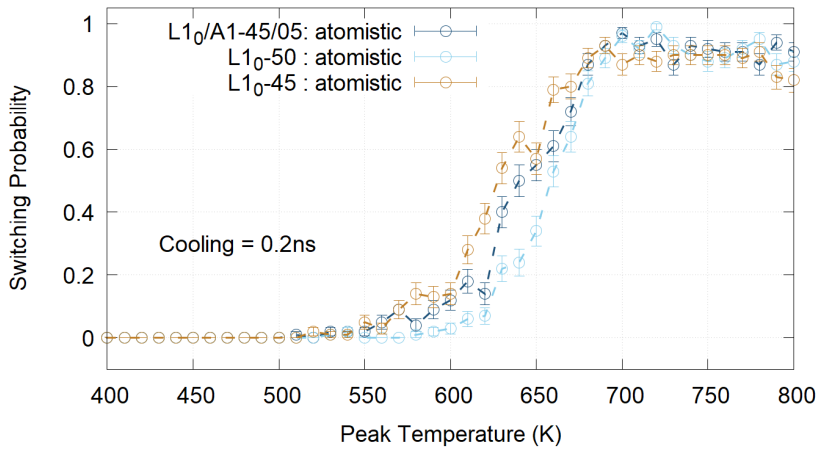

(a) $t_{cool} = 0.2ns$

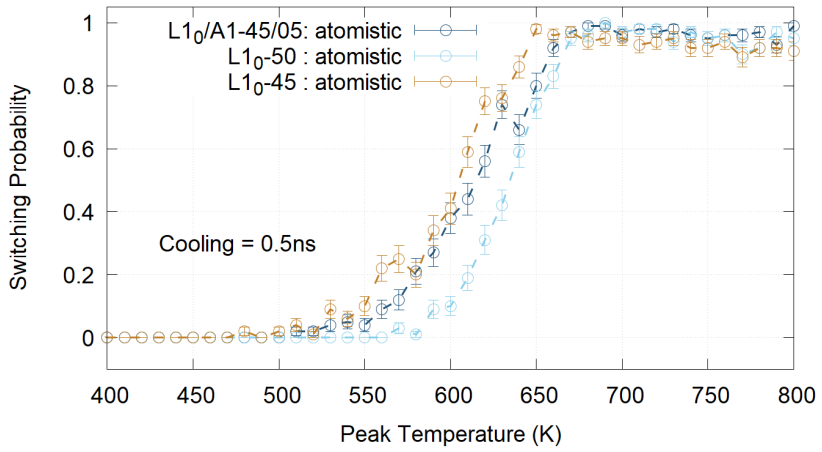

(b) $t_{cool} = 0.5ns$

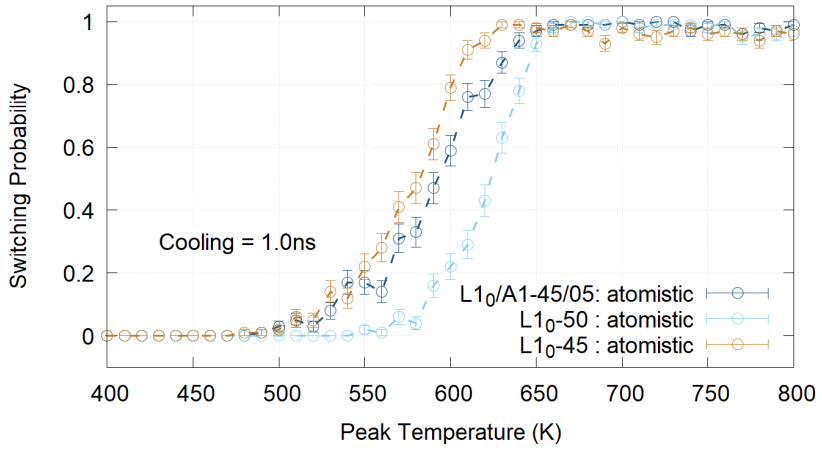

(c) $t_{cool} = 1.0ns$

Fig. 5.14 The effect of grain configurations on the switching probability for varying cooling time of (a) 0.2 ns, (b) 0.5 ns, and (c) 1.0 ns. Data are not temperature-rescaled.

where the product KV with K being the magneto-crytalline anisotropy density and V the grain volume is the volume anisotropy, k_B the Boltzmann constant, τ_m the measurement time which in this case is equal τ_N the Néel relaxation time, and τ_0 the characteristic attempt time of order $\tau_0 \approx 10^{-9} - 10^{-10}$ s. From this relation, the blocking temperature is decided by the volume anisotropy KV.

A comparison of switching probability between the $L1_0/A1-45/05$ and $L1_0-45$ configurations seems to conform to the prediction of Eq. (5.11). Previous results in Chapter 4 shows that in the $L1_0/A1-45/05$ configuration the exchange-coupling effect between the $L1_0$ with the $A1$-phase induces a fourth-order anisotropy component, although for the particular grain core size $R = 0.90$ this fourth-order anisotropy is of extremely small magnitude. Since the anisotropy in Chapter 4 is calculated from fitting to the system torque, it is the volume anisotropy KV of the entire system. Therefore the $L1_0/A1-45/05$ and $L1_0-45$ grains can be deemed to have similar KV. Simulation results confirms that the $L1_0/A1-45/05$ and $L1_0-45$ configurations exhibit almost the same blocking temperatures, an effect especially pronounced at the longest cooling time of 1.0 ns. At shorter cooling times, the blocking temperatures of the two configurations are observed to start to diverge slightly, although not yet conclusively. If this observation is to be validated, a possibility can be suggested that at smaller cooling times the magnetic spin moment M_sV might start to have a more significant impact which can slightly alter the blocking temperatures of the $L1_0/A1-45/05$ and $L1_0-45$ configuration.

Comparison between the $L1_0/A1-45/05$ and $L1_0-50$ configurations, on the other hand, is rather questionable. The volume anisotropy KV of the $L1_0-50$ grain is just slightly higher than that of the $L1_0/A1-45/05$ because of the replacement of the very thin low-anisotropy $A1$ phase in the former by the higher-anisotropy $L1_0$ phase. However, for the cooling time of 1.0 ns the blocking temperature of the $L1_0-50$ grain is shown to be significantly higher than that of the $L1_0/A1-45/05$, with the estimated difference to be approximately 50 K. This effect persists at shorter cooling times of 0.5 ns and 0.2 ns as well, albeit with reduced disparity. Again, the previously mentioned manifestation of M_sV at shorter cooling times might need to be taken into consideration here.

5.4 Further remarks and summary

An important conclusion that can be drawn is that for the implementation of a $L1_0$-FePt grain of a significantly reduced size, such as those tested in this Chapter, thermally-induced switching error rate is inevitable and non-negligible, especially with the application of a faster laser pulse as is desirable for HAMR. The hints to a solution, however, have been found in form of surface engineering via the addition of a disorder $A1$ shell around the ordered $L1_0$ core in order to

stabilise the magnetisation of the $L1_0$-phase. Remarkably, it appears that enclosing the $L1_0$ core by a layer of $A1$ phase seems to improve switching probability more effectively than increasing the size of the said $L1_0$ core by an equivalent amount. A possible explanation is that the additional $L1_0$ phase, whilst enhancing thermal writability via increasing the M_sVH factor, also increases the volume anisotropy KV which increases the blocking temperature - as seen for the $L1_0 - 50$ grain configuration. On the other hand, adding the $A1$ phase enhances thermal writability comparably without increasing the blocking temperature - as seen for the $L1_0/A1 - 45/05$ grain configuration. Overall, the interplay between the role of M_sV and KV has been seen to be a subtle effect which will necessitate further investigation in the future.

A very promising option for future consideration is to incorporate into the existing $L1_0/A1$-FePt core-shell structure, in addition to the soft-magnetic $A1$-FePt, an extra material of high Curie temperature which can further stabilise the $L1_0$-phase magnetisation order through the proximity effect [126, 127]. The combination of a high-anisotropy hard-magnetic material with a soft-magnetic material of higher Curie temperature but lower anisotropy has been demonstrated to trigger magnetisation reversal through a high-temperature exchange spring and such combination structures are known as exchange-coupled composite (ECC) media [130]. An optimised ECC-structured composition with 20% soft magnetic and 80% hard magnetic material has been reported to achieve a remarkable switching efficiency higher than 99.2% [131]. A notable candidate for such additional soft-magnetic material is Iron, which has been explored substantially in literature [127, 129, 131, 132]. An ECC medium consisting of a soft-magnetic Fe layer on top of the hard-magnetic $L1_0$-FePt layer has been reported to reduce thermally-induced switching error rate and to activate switching at lower temperatures [132–134]. All these considerations have been discussed and left open for implementation in the future.

6

Conclusions and further works

The Thesis has presented a comprehensive investigation of the two outstanding challenges which are still blocking the path toward the realisation of $L1_0$-FePt in HAMR recording media. These two challenges, interestingly, relate directly to the key magnetic qualities of $L1_0$-FePt which have made the material particularly promising for HAMR applications in the first place. The first challenge is the well-known size-dependent dispersion of the Curie temperature of the material, which because of the inevitable grain size distribution in any recording media presents a serious potential limitation of the thermal stability of HAMR. The second challenge is the existence and magnitude of higher anisotropies in the material due to phase-coupling effects, which has been shown in literature to be intrinsic to the fabrication of FePt grains. Any further enhancement to the already very strong uniaxial anisotropy of the material will have a direct impact on the switching chance of the grain magnetisation and consequently the switching error rate. In the following, the key findings of each result Chapter will be recapped from which an overall conclusion can be drawn.

Chapter 3 addresses the influence of finite-size effects on the Curie temperature dispersion of $L1_0$-FePt, the first of the two aforementioned challenges. Numerical simulations are able to reproduce the well-known size-dependence of the Curie temperature especially the rapid drop at smaller grain sizes. In order to explain this drop, besides the expected contribution from surface disorder due to the loss of exchange coordination at the grain surface, a deeper analysis of layer-resolved and cross-sectional magnetisation profiles in each grain reveals the propagation of surface disorder into the grain bulk which further amplifies the overall magnetisation loss. This propagation effect is found to become pronounced when the grain size is reduced to the sub-4 nm range. An analytic model is formulated to separate the two contributions from which a penetration depth characterising the propagation of surface disorder into the grain is defined. For small-sized grain, the decrease in magnetic order due to state energy renormalisation can no longer be compensated for by a fully-ordered central core. In this regime, therefore, the

state energy renormalisation becomes the dominant contributor leading to a rapid collapse of the grain magnetisation and consequent an increased dispersion of the Curie temperature as observed. The analytic model is strongly supported by comparable mean-field calculations and is subsequently shown to be valid for different lattice structure beyond the $L1_0$-FePt. The results presented in this Chapter, overall, affirm that finite size effects will become an increasingly important consideration for the aim of decreasing grain size in magnetic recording. Also, the results suggest that the Curie temperature dispersion in smaller-sized grains can be alleviated by an appropriate exchange-coupling composition in which the exchange-coupling between a low T_C hard material such as FePt with a high T_C material would help to reduce the loss of magnetic order through the proximity effect.

Chapter 4, in turn, explores the second challenge which is the pending question about the existence and behaviours of higher-order anistrotropies in $L1_0$-FePt. A previous study has found that in experimental $L1_0$-FePt grains the Pt atoms tend to segregate toward the grain surface, thus heavily compromising the atom composition and effectively converting the grain surface to the disordered $A1$-phase. To replicate this effect, a phase-coupled core-shell structured $L1_0/A1$-FePt system is computationally constructed and simulated from which a non-negligible fourth-order anisotropy is found to exist. This fourth-order anisotropy exhibits strong dependence on the system geometry and size of the $L1_0$ phase since its magnitude in relative to the second-order anisotropy is found to follow a non-monotonic pattern unseen in previous literature. Furthermore, a close examination shows that the scaling of the fourth-order anisotropy to magnetisation returns a scaling exponent of approximately 2.2 which is a remarkable departure from the classical Callen-Callen power law which instead predicts a scaling exponent of 10. An analytic model is then formulated to study the origin and behaviours of the new fourth-order term which achieves excellent agreement with numerical data. First, the origin of the fourth-order anisotropy is ascribed to a combination of the canting of the core/shell magnetisation and of the induced exchange coupling at the core/shell interface. Second, the derived expression of the fourth-order anisotropy from the analytic model relates it to the second-order anisotropy and the exchange interaction strength, which subsequently successfully explains the deviation of the obtained scaling exponent from the Callen-Callen power law. Overall, the results of this Chapter provide substantial insights into a topic that has otherwise been lacking attention, as well as solid justifications for further investigations of the core-shell structure in HAMR-applicable recording media.

Chapter 5 is built on the foundation laid by the previous two Chapters in which the knowledge gained from the impact of finite-size effects as well as the existence and behaviours of the fourth-order anisotropy in the phase-coupled core-shell structured $L1_0/A1$-FePt grains are combined for an investigation of the feasibility of such grains for a HAMR-applicable

recording medium. Although available data at this stage are yet sufficient to reach a conclusive verdict, which indicates the need for further work in the immediate future, two substantial observations can already been made. First, a thermally-induced switching exists which has been demonstrated to be inevitable and non-negligible. Reducing the grain size and using shorter heating pulses seem to worsen this switching error rate. Second, an interesting solution has been found in surface engineering of which evidences at this stage suggest would be able to yield an even better switching efficiency than increasing the grain size. This observation, if true, will potentially uncover many promising future directions for the research.

Overall, it is still a long way to go for the optimisation of $L1_0$-FePt for HAMR recording media. The material, whist still fascinating and exhibiting many key qualities necessary for an efficient HAMR functioning, is not yet ready for an economically and technologically feasible implementation. The Thesis, nevertheless, has contributed in several aspects to the understanding of not just $L1_0$-FePt as a material but also the underlying physics of the broader field. However, the studies do not end here; instead many questions are still left open as well as possibilities remained to be explored further, with many more promising discoveries awaiting to be made. A list of further developments stemmed from the research presented in this Thesis is discussed in the follows.

- *The investigation of finite-size effects in $L1_0$-FePt*: The investigation presented has been restricted to parallelepiped-shaped grains only because of the limitations of the VAMPIRE code version at that time. New features can be developed and implemented into the VAMPIRE code which enable the extraction of layer-resolved and cross-sectional magnetic properties for grains of different shapes - amongst which most notably the cylindrical and voronoi-structured grains. The randomly-generated voronoi shape is of particular interest since it offers the highest degree of surface irregularities which can set up a much stronger test for the correlation proposed between the Curie temperature dispersion and the surface magnetisation loss due to missing exchange coordination. However, it is also quite challenging to apply the same method to study the voronoi structure because of the lack of clear layers. Another interesting idea once discussed is to investigate the discovered propagation of surface disorder from a different dimension. In the ideal scenario if the necessary computational capabilities are all made available, a three-dimensional - instead of the presented one and two-dimensional - magnetisation profile can be hoped to be obtained which can provide a much more complete and accurate description of what really happens to the magnetisation inside the grain. This, if can be achieved, is essential for the derivation of a general mathematical expression which can quantify precisely the contribution of each individual part of the grain to the overall magnetisation.

- *The investigation of higher-order anisotropy in core-shell $L1_0/A1$-FePt*: Although the content of this Chapter is rather complete, a question still remains about the accuracy of the analytic model in the specific core size range $0.05 \leq R \leq 0.45$ where analytic predictions are seen to be slightly higher than numerical data. Furthermore, the validity of the analytic model in more complex systems is a very exciting aspect to be explored. Especially, since a possibility has been proposed in Chapter 5 to add an extra layer of Fe around the core-shell $L1_0/A1$-FePt to improve magnetisation order stability, an immediate idea would be extending the analytic model to a three-layer system incorporating the third exchange-coupling material with high Curie temperature but lower anisotropy.

- *The investigation of switching efficiency of core-shell $L1_0/A1$-FePt*: The previously discussed interplay between M_sV and KV, especially the role of M_sV, requires further examination, for example adding additional layer with zero-anisotropy which seems to help reduce the back-switching as is expected in terms of the model of Evans et al. [12]. Additionally, the aforementioned solution of grain surface engineering solution can be further explored. The current plan is to modify the existing core-shell structure to an exchange-coupled composite structure via the addition of an extra material with high Curie temperature, with a prominent choice being Fe because of the high availability of previous studies for this material in literature.

- *The investigation of temperature-rescaling effects in atomistic simulations*: Finally, it is time to address the pending question on the effects of temperature-rescaling in atomistic simulations. The main issue is that the temperature-rescaling exponent can only be derived from fitting to available experimental data, which in literature have been very lacking. Throughout the simulations in Chapter 5, a temperature-rescaling exponent of 1.75 has been applied. However, higher values have been suggested which would induce more drastic modifications to temperature-dependent magnetisation curve: a much flatter gradient below the Curie temperature and a much steeper drop close to the Curie temperature. Both of these effects, as already seen in available data presented, will alter the blocking temperature of each grain configuration and therefore might help to clarify the inconsistencies in their comparisons. Otherwise, the possibility mentioned in Chapter 5 about the role of the volume magnetisation MV to the blocking temperature at shorter cooling times might need to be seriously considered and investigated.

A

Simulation data tables

A.1 The grain size-dependent Curie temperature variation

D (nm)	modified-sc	fcc	bcc
1.088	463 ± 5	514 ± 5	449 ± 5
1.632	544 ± 5	584 ± 5	547 ± 5
1.904	570 ± 5	600 ± 5	573 ± 5
2.448	600 ± 5	625 ± 5	605 ± 5
2.992	615 ± 5	635 ± 5	622 ± 5
3.536	628 ± 5	640 ± 5	635 ± 5
4.080	635 ± 5	645 ± 5	640 ± 5
4.624	641 ± 5	650 ± 5	645 ± 5
4.896	645 ± 5	650 ± 5	645 ± 5
5.440	649 ± 5	655 ± 5	650 ± 5
5.984	651 ± 5	655 ± 5	652 ± 5
6.528	653 ± 5	655 ± 5	655 ± 5
7.072	655 ± 5	658 ± 5	655 ± 5
7.616	655 ± 5	660 ± 5	655 ± 5
7.888	657 ± 5	660 ± 5	655 ± 5
8.432	658 ± 5	660 ± 5	660 ± 5
8.976	660 ± 5	660 ± 5	660 ± 5
9.520	660 ± 5	660 ± 5	660 ± 5
10.064	660 ± 5	660 ± 5	660 ± 5

Table A.1 The Curie temperatures - in Kelvin, to 3 significant figures - of each grain size D for each simulated lattice structure. Note that since the temperature resolution in simulations is set at 5 K, the uncertainty is assigned whichever larger between statistical uncertainty and temperature resolution. Data are plotted in Fig. 3.7 of Chapter 3.

A.2 The correlation between the Curie temperature drop and atomistic bond loss

D (nm)	Δn_{bb}^{sc}	ΔT_C^{sc}	Δn_{bb}^{fcc}	ΔT_C^{fcc}	Δn_{bb}^{bcc}	ΔT_C^{bcc}
1.088	14.6	31.4	15.5	22.8	23.7	32.8
1.632	10.8	19.3	11.2	12.3	17.1	18.2
1.904	9.6	15.5	9.9	9.9	15.1	14.2
2.448	7.9	11.1	8.1	6.2	12.4	9.5
2.992	6.8	8.8	6.9	4.7	10.5	7.0
3.536	6.0	6.8	6.1	3.9	9.3	5.0
4.080	5.4	5.8	5.5	3.2	8.3	4.2
4.624	4.9	5.0	5.0	2.4	7.6	3.5
4.896	4.7	4.3	4.8	2.4	7.3	3.5
5.440	4.4	3.7	4.5	1.7	6.8	2.7
5.984	4.1	3.5	4.2	1.7	6.3	2.5
6.528	3.9	3.1	3.9	1.7	6.0	2.0
7.072	3.7	2.8	3.7	1.2	5.7	2.0
7.616	3.5	2.8	3.6	0.9	5.4	2.0
7.888	3.5	2.6	3.5	0.9	5.3	2.0
8.432	3.3	2.4	3.3	0.9	5.1	1.2
8.976	3.2	2.1	3.2	0.9	4.9	1.2
9.520	3.1	2.1	3.1	0.9	4.7	1.2
10.064	3.0	2.1	3.0	0.9	4.6	1.2

Table A.2 The percentage atomistic bond loss Δn_{bb} and Curie temperature reduction ΔT_C at each grain size D for each simulated lattice structure - rounded up to 1 decimal. The superscript indicates the lattice type. Data are plotted in Fig. 3.15 of Chapter 3.

A.3 The core size-dependent magnitude of the fourth-order anisotropy

This Section provides the tabulated core size-dependent percentage magnitude of the fourth-order anisotropy in relative to the second-order anisotropy, K_2/K_1, at $T = 10$ K. A negative K_2/K_1 is obtained at the extreme case $R = 0.05$ in which the $L1_0$ core consists of a single Fe

atom, thus the 2-ion anisotropy is completely eliminated leaving only the negative single-site local anisotropy.

R	K_2/K_1 (%)
0.05	-0.04
0.10	1.47
0.15	3.52
0.20	5.81
0.25	8.72
0.30	12.19
0.35	14.69
0.40	17.81
0.45	19.88
0.50	22.41
0.55	22.28
0.60	21.47
0.65	19.98
0.70	18.18
0.75	16.17
0.80	12.49
0.95	9.01
0.90	5.73
0.95	1.24

Table A.3 The percentage magnitude of the fourth-order anisotropy constant in relative to the second-order anisotropy constant, K_2/K_1, for each core size R at $T = 10$ K. Data are plotted in Fig. 4.8 of Chapter 4.

B

Sampled VAMPIRE simulation files

The Appendix provides the sampled VAMPIRE-compatible inputs and material files for the simulations presented in Chapter 3, 4, and 5 with explanatory comments in *italic*.

B.1 Chapter 3 - Investigation of finite-size effects

The parallelepiped FePt grains are constructed by stacking up atomistic layers along the grain height. This method allows the extraction of magnetic properties on each atomistic layer which is necessary for the computation of the layer-resolved and cross-sectional magnetisation profiles of the grains. The simulation is run at each temperature between 0 K and 1000 K in 5 K steps, and the outputs of each temperature point are combined to create a "master" output file. The sampled input and material file of a modified-sc FePt grain of 101.1 Å height and 11.88 Å base sizes which comprises of 4 sc-unitcells i.e. 5 atomistic layers at 100 K are shown below.

B.1.1 Input

Specify lattice structure, unitcell sizes, and grain sizes: "!A" = Å
create:crystal-structure=sc
dimensions:unit-cell-size-x = 2.72 !A
dimensions:unit-cell-size-y = 2.72 !A
dimensions:unit-cell-size-z = 3.85 !A
dimensions:system-size-x = 11.88 !A
dimensions:system-size-y = 11.88 !A
dimensions:system-size-z = 101.1 !A

Specify the name of material file to be used:

material:file=FePtsc6350.mat

Specify simulation integrators and parameters:
sim:program=time-series
sim:integrator=monte-carlo
sim:integrator-random-seed=22696
sim:equilibration-temperature=100
sim:temperature=100
sim:time-steps-increment=1
sim:time-step=1.0E-16
sim:equilibration-time-steps=50000000
sim:total-time-steps=250000000
sim:applied-field-strength=0 !T

B.1.2 Material file

Specify number of atomistic layers included in the grain: each layer = material
material:num-materials=5

Specify magnetic parameters for each atomistic layer:
material[1]:material-name="FePt-1"
material[1]:damping-constant=1.0
material[1]:atomic-spin-moment=3.23 !muB
material[1]:uniaxial-anisotropy-constant=2.63e-22
material[1]:minimum-height=0
material[1]:maximum-height=0.2
material[1]:exchange-matrix[1]=6.350e-21
material[1]:exchange-matrix[2]=6.350e-21
material[1]:exchange-matrix[3]=6.350e-21
material[1]:exchange-matrix[4]=6.350e-21
material[1]:exchange-matrix[5]=6.350e-21

material[2]:material-name="FePt-2"
material[2]:damping-constant=1.0
material[2]:atomic-spin-moment=3.23 !muB
material[2]:uniaxial-anisotropy-constant=2.63e-22
material[2]:minimum-height=0.2

material[2]:maximum-height=0.4
material[2]:exchange-matrix[1]=6.350e-21
material[2]:exchange-matrix[2]=6.350e-21
material[2]:exchange-matrix[3]=6.350e-21
material[2]:exchange-matrix[4]=6.350e-21
material[2]:exchange-matrix[5]=6.350e-21

material[3]:material-name="FePt-3"
material[3]:damping-constant=1.0
material[3]:atomic-spin-moment=3.23 !muB
material[3]:uniaxial-anisotropy-constant=2.63e-22
material[3]:minimum-height=0.4
material[3]:maximum-height=0.6
material[3]:exchange-matrix[1]=6.350e-21
material[3]:exchange-matrix[2]=6.350e-21
material[3]:exchange-matrix[3]=6.350e-21
material[3]:exchange-matrix[4]=6.350e-21
material[3]:exchange-matrix[5]=6.350e-21

material[4]:material-name="FePt-4"
material[4]:damping-constant=1.0
material[4]:atomic-spin-moment=3.23 !muB
material[4]:uniaxial-anisotropy-constant=2.63e-22
material[4]:minimum-height=0.6
material[4]:maximum-height=0.8
material[4]:exchange-matrix[1]=6.350e-21
material[4]:exchange-matrix[2]=6.350e-21
material[4]:exchange-matrix[3]=6.350e-21
material[4]:exchange-matrix[4]=6.350e-21
material[4]:exchange-matrix[5]=6.350e-21

material[5]:material-name="FePt-5"
material[5]:damping-constant=1.0
material[5]:atomic-spin-moment=3.23 !muB
material[5]:uniaxial-anisotropy-constant=2.63e-22
material[5]:minimum-height=0.8

material[5]:maximum-height=1
material[5]:exchange-matrix[1]=6.350e-21
material[5]:exchange-matrix[2]=6.350e-21
material[5]:exchange-matrix[3]=6.350e-21
material[5]:exchange-matrix[4]=6.350e-21
material[5]:exchange-matrix[5]=6.350e-21

B.2 Chapter 4 - Investigation of the core-shell structure

The phase-coupled $L1_0/A1$ core-shell structured FePt grains were created with variable fractional core size using the core-shell feature of VAMPIRE. The construction of the $L1_0/A1$ phases starts with first creating an all-Fe fcc lattice structure for both phases, then substituting the non-magnetic Pt atoms for Fe in appropriate positions and proportions for respective phase: for the $L1_0$ phase the Pt atoms occupy well-defined alternating-layer positions whilst for the $A1$ phase the Pt atoms are simply mixed-in randomly with a proportion ratio of 0.5. Furthermore, the exchange interactions for each constituent atom type are defined three-dimensional and extending to the third-level of nearest neighbours, with the 2-ion anisotropy being added to the z-dimension components of $L1_0$-phased Fe-Fe interactions. The sampled input and material file of the grain with fractional core size = 0.5 at 100 K being constrained by 45^{o} degree to the easy axis are shown below.

B.2.1 Input

Specify lattice structure, unitcell sizes, and grain sizes and shape with faceting fractional radii along the [001], [110], and [111] lattice direction: "!A" = Å
create:crystal-structure=fcc
create:crystal-sublattice-materials
create:faceted-particle = 1.00,1.15,1.00
dimensions:unit-cell-size = 3.795 !A
dimensions:system-size-x = 8.1 !nm
dimensions:system-size-y = 8.1 !nm
dimensions:system-size-z = 12.1 !nm
dimensions:particle-size= 8 !nm
dimensions:particle-shape-factor-z=1.5

Specify the range and type of truncated exchange interaction:

exchange:interaction-range = 1.8
exchange:function = shell

Specify the name of material file to be used:
material:file=FePtCS.mat

Specify simulation integrators and parameters:
sim:program=time-series
sim:integrator=constrained-monte-carlo
sim:integrator-random-seed=16214
sim:equilibration-temperature=100
sim:temperature=100
sim:time-steps-increment=1
sim:equilibration-time-steps=200000
sim:total-time-steps=800000
sim:time-step=1.0E-16
sim:applied-field-strength=0 !T
sim:constraint-angle-phi = 45
sim:constraint-angle-theta = 0

B.2.2 Material file

There are 10 materials in total. Materials of number (1,2,3,4) and (6,7,8,9) for the Fe-basis of each $L1_0$ and $A1$ phase respectively, and two non-magnetic Pt material 5 and 10 to be substituted into the $L1_0$ and $A1$ phase respectively.
material:num-materials=10

Specify magnetic parameters:
material[1]:material-name=L10-FePt1
material[1]:damping-constant=1.0
material[1]:atomic-spin-moment=3.23 !muB
material[1]:second-order-uniaxial-anisotropy-constant=-1.552e-23
material[1]:material-element=Fe
material[1]:minimum-height=0.0
material[1]:maximum-height=1.0
material[1]:core-shell-size = 0.500
material[1]:unit-cell-category=1

Specify the proportion to be substituted by Pt atoms: 0 or 1 if $L1_0$ phase, 0.5 if A1 phase
material[1]:host-alloy=homogeneous
material[1]:alloy-fraction[5]=0.0

$L1_0$-Fe and $L1_0$-Fe interaction: with 2-ion anisotropy added to the z-component
material[1]:exchange-matrix-1st-nn[1] = 2.1428571e-21,2.1428571e-21,2.1564476e-21
material[1]:exchange-matrix-2nd-nn[1] = 3.0000000e-21,3.0000000e-21,3.0190267e-21
material[1]:exchange-matrix-3rd-nn[1] = 1.1785714e-21,1.1785714e-21,1.1860462e-21

$L1_0$-Fe and $L1_0$-Fe interaction: with 2-ion anisotropy added to the z-component
material[1]:exchange-matrix-1st-nn[2] = 2.1428571e-21,2.1428571e-21,2.1564476e-21
material[1]:exchange-matrix-2nd-nn[2] = 3.0000000e-21,3.0000000e-21,3.0190267e-21
material[1]:exchange-matrix-3rd-nn[2] = 1.1785714e-21,1.1785714e-21,1.1860462e-21

$L1_0$-Fe and $L1_0$-Pt interaction: without 2-ion anisotropy added
material[1]:exchange-matrix-1st-nn[3] = 2.1428571e-21,2.1428571e-21,2.1428571e-21
material[1]:exchange-matrix-2nd-nn[3] = 3.0000000e-21,3.0000000e-21,3.0000000e-21
material[1]:exchange-matrix-3rd-nn[3] = 1.1785714e-21,1.1785714e-21,1.1785714e-21

$L1_0$-Fe and $L1_0$-Pt interaction: without 2-ion anisotropy added
material[1]:exchange-matrix-1st-nn[4] = 2.1428571e-21,2.1428571e-21,2.1428571e-21
material[1]:exchange-matrix-2nd-nn[4] = 3.0000000e-21,3.0000000e-21,3.0000000e-21
material[1]:exchange-matrix-3rd-nn[4] = 1.1785714e-21,1.1785714e-21,1.1785714e-21

$L1_0$-Fe and A1-Fe interaction: without 2-ion anisotropy added
material[1]:exchange-matrix-1st-nn[6] = 2.1428571e-21,2.1428571e-21,2.1428571e-21
material[1]:exchange-matrix-2nd-nn[6] = 3.0000000e-21,3.0000000e-21,3.0000000e-21
material[1]:exchange-matrix-3rd-nn[6] = 1.1785714e-21,1.1785714e-21,1.1785714e-21

$L1_0$-Fe and A1-Fe interaction: without 2-ion anisotropy added
material[1]:exchange-matrix-1st-nn[7] = 2.1428571e-21,2.1428571e-21,2.1428571e-21
material[1]:exchange-matrix-2nd-nn[7] = 3.0000000e-21,3.0000000e-21,3.0000000e-21
material[1]:exchange-matrix-3rd-nn[7] = 1.1785714e-21,1.1785714e-21,1.1785714e-21

$L1_0$-Fe and A1-Fe interaction: without 2-ion anisotropy added

material[1]:exchange-matrix-1st-nn[8] = 2.1428571e-21,2.1428571e-21,2.1428571e-21
material[1]:exchange-matrix-2nd-nn[8] = 3.0000000e-21,3.0000000e-21,3.0000000e-21
material[1]:exchange-matrix-3rd-nn[8] = 1.1785714e-21,1.1785714e-21,1.1785714e-21

$L1_0$-Fe and A1-Pt interaction: without 2-ion anisotropy added
material[1]:exchange-matrix-1st-nn[9] = 2.1428571e-21,2.1428571e-21,2.1428571e-21
material[1]:exchange-matrix-2nd-nn[9] = 3.0000000e-21,3.0000000e-21,3.0000000e-21
material[1]:exchange-matrix-3rd-nn[9] = 1.1785714e-21,1.1785714e-21,1.1785714e-21

And so on for material (2,3,4,6,7,8,9)...

Pt-substitution material 5 and 10 follow this form:
material[5]:material-name=L10-Pt
material[5]:damping-constant=1.0
material[5]:atomic-spin-moment=1.0 !muB
material[5]:material-element=Pt
material[5]:minimum-height=0.0
material[5]:maximum-height=0.0
material[5]:non-magnetic=remove

B.3 Chapter 5 - Investigation of the switching efficiency

The input and material files in this Chapter follow the same format as those in Chapter 4 with the only modification being to include the externally laser pulse and magnetic cooling field in the input. These command lines below are added to or modified the corresponding ones in the sampled input of Chapter 4.

Change the simulation integrators:
sim:program=field-cool
sim:cooling-function=double-gaussian
sim:integrator=llg-heun
sim:integrator-random-seed=25033
sim:simulation-cycles=1

Add the parameters of the laser pulse: ambient temperature 300K, peak temperature 700K, cooling time 0.5ns

sim:cooling-time=0.500 !ns
sim:minimum-temperature=300
sim:maximum-temperature=700
sim:equilibration-temperature=300

Add the parameters of the magnetic cooling field: magnitude 0.8 Tesla opposing the initial magnetisation
sim:applied-field-strength=-0.8 !T
sim:applied-field-unit-vector=0.0,0.0,1.0

Other parameters
sim:time-steps-increment=1
sim:time-step=1.0E-16
sim:preconditioning-steps=1000
sim:equilibration-time-steps=10000
sim:total-time-steps=30000000

References

[1] R. Wood, "Future hard disk drive systems," Journal of Magnetism and Magnetic Materials, vol. 321, pp. 555–561, 2009.

[2] H. J. Richter, A. Lyberatos, U. Nowak, R. Evans, and R. Chantrell, "The thermodynamic limits of magnetic recording," Journal of Applied Physics, vol. 111, pp. 033909–033909, 2012.

[3] T. Yogi, G. Gorman, C. Hwang, M. Kakalec, and S. Lambert, "Dependence of magnetics, microstructures and recording properties on underlayer thickness in CoNiCr/Cr media," IEEE Transactions on Magnetics, vol. 24, no. 6, pp. 2727–2729, 1988.

[4] S. H. Charap, P.-L. Lu, and Y. He, "Thermal stability of recorded information at high densities," IEEE Transactions on Magnetics, vol. 33, no. 1, pp. 978–983, 1997.

[5] S. Khizroev and D. Litvinov, "Perpendicular magnetic recording: Writing process," Journal of Applied Physics, vol. 95, no. 9, pp. 4521–4537, 2004.

[6] S. Iwasaki and Y. Nakamura, "The magnetic field distribution of a perpendicular recording head," IEEE Transactions on Magnetics, vol. 14, no. 5, pp. 436–438, 1978.

[7] S. N. Piramanayagam, "Perpendicular recording media for hard disk drives," Journal of Applied Physics, vol. 102, no. 1, p. 011301, 2007.

[8] K. Tham, Y. Sonobe, and K. Wago, "Magnetic and Read–Write properties of Coupled Granular/Continuous Perpendicular recording media and magnetization reversal process," Magnetics, IEEE Transactions on, vol. 43, pp. 671 – 675, 2007.

[9] B. Tudu and A. Tiwari, "Recent developments in perpendicular magnetic anisotropy thin films for data storage applications," Vacuum, vol. 146, pp. 329–341, 2017.

[10] H. J. Richter, "The transition from longitudinal to perpendicular recording," Journal of Physics D: Applied Physics, vol. 40, no. 9, pp. R149–R177, 2007.

[11] D. Suess, F. Dorfbauer, I. Kalcher, T. Schrefl, and J. Fidler, "Micromagnetic modelling of advanced recording structures," 2022.

[12] R. F. L. Evans, R. W. Chantrell, U. Nowak, A. Lyberatos, and H.-J. Richter, "Thermally induced error: Density limit for magnetic data storage," Applied Physics Letters, vol. 100, no. 10, p. 102402, 2012.

[13] R. White, R. Newt, and R. Pease, "Patterned media: a viable route to 50 Gbit/in2 and up for magnetic recording?," IEEE Transactions on Magnetics, vol. 33, no. 1, pp. 990–995, 1997.

[14] D. Weller, G. Parker, O. Mosendz, E. Champion, B. Stipe, X. Wang, T. Klemmer, G. Ju, and A. Ajan, "A HAMR media technology roadmap to an areal density of 4 Tb/in2," IEEE Transactions on Magnetics, vol. 50, no. 1, pp. 1–8, 2014.

[15] D. Weller, G. Parker, O. Mosendz, A. Lyberatos, D. Mitin, N. Schmidt, and M. Albrecht, "Review article: FePt heat assisted magnetic recording media," Journal of Vacuum Science and Technology B, Nanotechnology and Microelectronics: Materials, Processing, Measurement, and Phenomena, vol. 34, p. 060801, 2016.

[16] M. H. Kryder, E. C. Gage, T. W. McDaniel, W. A. Challener, R. E. Rottmayer, G. Ju, Y. Hsia, and M. F. Erden, "Heat assisted magnetic recording," Proceedings of the IEEE, vol. 96, no. 11, pp. 1810–1835, 2008.

[17] G. Ju, Y. Peng, E. K. C. Chang, Y. Ding, A. Q. Wu, X. Zhu, Y. Kubota, T. J. Klemmer, H. Amini, L. Gao, Z. Fan, T. Rausch, P. Subedi, M. Ma, S. Kalarickal, C. J. Rea, D. V. Dimitrov, P.-W. Huang, K. Wang, X. Chen, C. Peng, W. Chen, J. W. Dykes, M. A. Seigler, E. C. Gage, R. Chantrell, and J.-U. Thiele, "High density Heat-Assisted Magnetic Recording media and advanced characterization—progress and challenges," IEEE Transactions on Magnetics, vol. 51, no. 11, pp. 1–9, 2015.

[18] C. Vogler, C. Abert, F. Bruckner, D. Suess, and D. Praetorius, "Heat-assisted magnetic recording of bit-patterned media beyond 10Tb/in2," Applied Physics Letters, vol. 108, no. 10, p. 102406, 2016.

[19] K. Şendur and W. Challener, "Patterned medium for heat assisted magnetic recording," Applied Physics Letters, vol. 94, no. 3, p. 032503, 2009.

[20] http://idema.org/?page_id=416. Accessed: 2022-10-03.

[21] W. Heisenberg, "On the theory of ferromagnetism," Z. Physik, vol. 49, pp. 619–636, 1928.

[22] A. H. Morrish, The Physical Principles of Magnetism. Wiley-IEEE Press, 1st ed., 2001.

[23] D. Jiles, Solid State Physics. CRC Press, 3rd ed., 2016.

[24] N. D. M. Neil W Ashcroft, Introduction to Magnetism and Magnetic Materials. New York, Holt, Rinehart and Winston, 1976.

[25] W. Pauli, "Über den zusammenhang des abschlusses der elektronengruppen im atom mit der komplexstruktur der spektren," Z. Physik, vol. 31, p. 765–783, 1925.

[26] W. Heitler and F. London, "Wechselwirkung neutraler atome und homöopolare bindung nach der quantenmechanik," Z. Physik, vol. 44, p. 455–472, 1927.

[27] R. Skomski, Simple Models of Magnetism. Oxford University Press, 2008.

[28] X. Li, H. Yu, L. Feng, F. J.S., M.-H. Whangbo, and H. Xiang, "Spin Hamiltonians in magnets: Theories and Computations," Molecules, vol. 26, p. 803, 2021.

[29] M. Uhl and B. Siberchicot, "A first-principles study of exchange integrals in magnetite," Journal of Physics: Condensed Matter, vol. 7, no. 22, pp. 4227–4237, 1995.

[30] C. M. Srivastava, G. Srinivasan, and N. G. Nanadikar, "Exchange constants in spinel ferrites," Phys. Rev. B, vol. 19, pp. 499–508, 1979.

[31] R. F. L. Evans, "Atomistic modelling of nanogranular magnetic materials," Doctoral Dissertation to the University of York, 2008.

[32] P. Gruszecki, C. Banerjee, M. Mruczkiewicz, O. Hellwig, A. Barman, and M. Krawczyk, "Chapter two - the influence of the internal domain wall structure on spin wave band structure in periodic magnetic stripe domain patterns," in Solid State Physics (R. E. Camley and R. L. Stamps, eds.), vol. 72 of Solid State Physics, pp. 29–82, Academic Press, 2021.

[33] J. Fidler, R. Chantrell, T. Schrefl, and M. Wongsam, "Micromagnetics: Basic principles," Encyclopedia of Materials: Science and Technology, 2001.

[34] S. Majumdar, H. Majumdar, and R. Österbacka, "1.05 - organic spintronics," in Comprehensive Nanoscience and Technology (D. L. Andrews, G. D. Scholes, and G. P. Wiederrecht, eds.), pp. 109–142, Amsterdam: Academic Press, 2011.

[35] F. Luborsky, J. Livingston, and G. Chin, "Chapter 29 - magnetic properties of metals and alloys," in Physical Metallurgy (Fourth Edition) (R. W. Cahn and P. Haasen, eds.), pp. 2501–2565, Oxford: North-Holland, fourth edition ed., 1996.

[36] D. P. Zeeman, "Vii. doublets and triplets in the spectrum produced by external magnetic forces," The London, Edinburgh, and Dublin Philosophical Magazine and Journal of Science, vol. 44, no. 266, pp. 55–60, 1897.

[37] L. Landau and E. Lifshitz, "18 - On the theory of the dispersion of magnetic permeability in ferromagnetic bodies," in Collected Papers of L.D. Landau (D. Ter Haar, ed.), pp. 101–114, Pergamon, 1965.

[38] T. L. Gilbert, Formulation, Foundations and Applications of the Phenomenological Theory of Ferromagnetism. PhD thesis, Illinois Institute of Technology, 1956.

[39] R. F. L. Evans, W. J. Fan, P. Chureemart, T. A. Ostler, M. O. A. Ellis, and R. W. Chantrell, "Atomistic spin model simulations of magnetic nanomaterials," Journal of Physics: Condensed Matter, vol. 26, no. 10, p. 103202, 2014.

[40] M. O. A. Ellis, R. F. L. Evans, T. A. Ostler, J. Barker, U. Atxitia, O. Chubykalo-Fesenko, and R. W. Chantrell, "The Landau–Lifshitz equation in atomistic models," Low Temperature Physics, vol. 41, no. 9, pp. 705–712, 2015.

[41] M. S. Strungaru, "Advanced atomistic models for magnetisation dynamics," Doctoral Dissertation to the University of York, 2020. https://etheses.whiterose.ac.uk/28970/.

[42] W. Brown, Micromagnetics. Interscience Tracts of Physics and Astronomy 18, Interscience Publishers (Wiley & Sons), 1963.

[43] A. Aharoni, An Introduction to the Theory of Ferromagnetism. Clarendon Press, Oxford University Press, 2000.

[44] J. Leliaert, M. Dvornik, J. Mulkers, J. De Clercq, M. V. Milošević, and B. Van Waeyenberge, "Fast micromagnetic simulations on GPU - Recent advances made with mumax3," Journal of Physics D: Applied Physics, vol. 51, no. 12, p. 123002, 2018.

[45] https://math.nist.gov/oommf/. Accessed: 2022-22-02.

[46] A. Vansteenkiste, J. Leliaert, M. Dvornik, M. Helsen, F. Garcia-Sanchez, and B. Van Waeyenberge, "The design and verification of mumax3," AIP Advances, vol. 4, no. 10, p. 107133, 2014.

[47] http://micromagnetics.org/magnum.fe/. Accessed: 2022-02-22.

[48] https://nmag-project.github.io/. Accessed: 2022-22-02.

[49] http://magnetism.eu/43-software.html. Accessed: 2022-22-02.

[50] D. A. Garanin, "Fokker-Planck and Landau-Lifshitz-Bloch equations for classical ferromagnets," Phys. Rev. B, vol. 55, pp. 3050–3057, 1997.

[51] V. Blum, R. Gehrke, F. Hanke, P. Havu, V. Havu, X. Ren, K. Reuter, and M. Scheffler, "Ab initio molecular simulations with numeric atom-centered orbitals," Computer Physics Communications, vol. 180, no. 11, pp. 2175–2196, 2009.

[52] "https://vampire.york.ac.uk/."

[53] N. Metropolis, A. W. Rosenbluth, M. N. Rosenbluth, A. H. Teller, and E. Teller, "Equation of state calculations by fast computing machines," The Journal of Chemical Physics, vol. 21, no. 6, pp. 1087–1092, 1953.

[54] D. Hinzke and U. Nowak, "Monte Carlo simulation of magnetization switching in a Heisenberg model for small ferromagnetic particles," Computer Physics Communications, vol. 121-122, pp. 334–337, 1999. Proceedings of the Europhysics Conference on Computational Physics CCP 1998.

[55] K. Binder, "Applications of Monte Carlo methods to statistical physics," Reports on Progress in Physics, vol. 60, no. 5, pp. 487–559, 1997.

[56] P. Asselin, R. F. L. Evans, J. Barker, R. W. Chantrell, R. Yanes, O. Chubykalo-Fesenko, D. Hinzke, and U. Nowak, "Constrained Monte Carlo method and calculation of the temperature dependence of magnetic anisotropy," Phys. Rev. B, vol. 82, p. 054415, 2010.

[57] H. Callen and E. Callen, "The present status of the temperature dependence of magnetocrystalline anisotropy, and the l(l+1)/2 power law," J. Phys. Chem. Solids, vol. 27, no. 8, pp. 1271 – 1285, 1966.

[58] R. F. L. Evans, U. Atxitia, and R. W. Chantrell, "Quantitative simulation of temperature-dependent magnetization dynamics and equilibrium properties of elemental ferromagnets," Phys. Rev. B, vol. 91, p. 144425, 2015.

[59] M. Campostrini, M. Hasenbusch, A. Pelissetto, P. Rossi, and E. Vicari, "Critical exponents and equation of state of the three-dimensional Heisenberg universality class," Phys. Rev. B, vol. 65, p. 144520, 2002.

[60] M. Strungaru, S. Ruta, R. F. Evans, and R. W. Chantrell, "Model of magnetic damping and anisotropy at elevated temperatures: Application to granular FePt films," Phys. Rev. Applied, vol. 14, p. 014077, 2020.

[61] D. A. Garanin, "Self-consistent Gaussian approximation for classical spin systems: Thermodynamics," Phys. Rev. B, vol. 53, pp. 11593–11605, 1996.

[62] C. Penny, A. R. Muxworthy, and K. Fabian, "Mean-field modelling of magnetic nanoparticles: The effect of particle size and shape on the curie temperature," Phys. Rev. B, vol. 99, p. 174414, 2019.

[63] O. Hovorka and T. Sluckin, "A computational mean-field model of interacting non-collinear classical spins," arXiv:submit/3292751 [cond-mat], 2020.

[64] U. Atxitia, D. Hinzke, O. Chubykalo-Fesenko, U. Nowak, H. Kachkachi, O. N. Mryasov, R. F. Evans, and R. W. Chantrell, "Multiscale modeling of magnetic materials: Temperature dependence of the exchange stiffness," Physical Review B, vol. 82, no. 13, p. 134440, 2010.

[65] S. Okamoto, O. Kitakami, N. Kikuchi, T. Miyazaki, Y. Shimada, and Y. K. Takahashi, "Size dependences of magnetic properties and switching behavior in FePt $L1_0$ nanoparticles," Phys. Rev. B, vol. 67, p. 094422, 2003.

[66] S. Okamoto, N. Kikuchi, O. Kitakami, T. Miyazaki, Y. Shimada, and K. Fukamichi, "Chemical-order-dependent magnetic anisotropy and exchange stiffness constant of FePt (001) epitaxial films," Phys. Rev. B, vol. 66, p. 024413, 2002.

[67] O. N. Mryasov, U. Nowak, K. Y. Guslienko, and R. W. Chantrell, "Temperature-dependent magnetic properties of FePt: Effective spin hamiltonian model," EPL (Europhysics Letters), vol. 69, no. 5, pp. 805–811, 2005.

[68] R. Rottmayer, S. Batra, D. Buechel, W. Challener, J. Hohlfeld, Y. Kubota, L. Li, B. Lu, C. Mihalcea, K. Mountfield, K. Pelhos, C. Peng, T. Rausch, M. Seigler, D. Weller, and X.-M. Yang, "Heat-assisted magnetic recording," IEEE Transactions on Magnetics, vol. 42, no. 10, pp. 2417–2421, 2006.

[69] T. W. McDaniel, "Ultimate limits to thermally assisted magnetic recording," Journal of Physics: Condensed Matter, vol. 17, no. 7, pp. R315–R332, 2005.

[70] H. Loc Nguyen, L. E. M. Howard, G. W. Stinton, S. R. Giblin, B. Tanner, I. Terry, A. K. Hughes, I. M. Ross, A. Serres, and J. S. O. Evans, "Synthesis of size-controlled fcc and fct FePt nanoparticles," Chemistry of Materials, vol. 18, p. 6414–6424, 2006.

[71] J.-U. Thiele, S. Maat, J. Robertson, and E. Fullerton, "Magnetic and structural properties of FePt-FeRh exchange spring films for thermally assisted magnetic recording media," IEEE Transactions on Magnetics, vol. 40, no. 4, pp. 2537–2542, 2004.

[72] G. Barucca, T. Speliotis, G. Giannopoulos, D. Niarchos, B. Rutkowski, A. Czyrska-Filemonowicz, E. Agostinelli, S. Laureti, A. Testa, and G. Varvaro, "Magnetic anisotropy phase-graded A1/L10-FePt films on amorphous glass substrates," Materials and Design, vol. 123, pp. 147 – 153, 2017.

[73] T. J. Zhou, K. Cher, J. F. Hu, Z. M. Yuan, and B. Liu, "The concept and fabrication of exchange switchable trilayer of FePt/FeRh/FeCo with reduced switching field," Journal of Applied Physics, vol. 111, no. 7, p. 07C116, 2012.

[74] F. Wang, H. Xing, and X. Xu, "Overcoming the trilemma issues of ultrahigh density perpendicular magnetic recording media by L1 0 - Fe (Co) Pt materials," SPIN, vol. 05, p. 150407184639006, 2015.

[75] M. Nakaya, M. Kanehara, M. Yamauchi, H. Kitagawa, and T. Teranishi, "Hydrogen-induced crystal structural transformation of FePt nanoparticles at low temperature," The Journal of Physical Chemistry C, vol. 111, no. 20, pp. 7231–7234, 2007.

[76] H. Li and J. Zhu, "The role of media property distribution in HAMR SNR," IEEE Transactions on Magnetics, vol. 49, no. 7, pp. 3568–3571, 2013.

[77] J.-G. J. Zhu and H. Li, "Signal-to-noise ratio impact of grain-to-grain heating variation in heat assisted magnetic recording," Journal of Applied Physics, vol. 115, no. 17, p. 17B747, 2014.

[78] J. Waters, D. Kramer, T. Sluckin, and O. Hovorka, "Resolving anomalies in the critical exponents of FePt using finite-size scaling in magnetic fields," Phys. Rev. Applied, vol. 11, p. 024028, 2019.

[79] A. Lyberatos, D. Weller, and G. J. Parker, "Finite size effects in L1o-FePt nanoparticles," Journal of Applied Physics, vol. 114, no. 23, p. 233904, 2013.

[80] O. Hovorka, S. Devos, Q. Coopman, W. J. Fan, C. J. Aas, R. F. L. Evans, X. Chen, G. Ju, and R. W. Chantrell, "The Curie temperature distribution of FePt granular magnetic recording media," Applied Physics Letters, vol. 101, no. 5, p. 052406, 2012.

[81] N. Goldenfeld, Lectures on phase transitions and the renormalization group. CRC Press, 2018.

[82] A. Kabir, J. Hu, V. Turkowski, R. Wu, R. Camley, and T. S. Rahman, "Effect of structure on the magnetic anisotropy of L10-FePt nanoparticles," Physical Review B, vol. 92, no. 5, 2015.

[83] J. Lyubina, O. Isnard, O. Gutfleisch, K.-H. Müller, and L. Schultz, "Ordering of nanocrystalline Fe–Pt alloys studied by in situ neutron powder diffraction," Journal of Applied Physics, vol. 100, no. 9, p. 094308, 2006.

[84] F. G. Sanchez, "Modeling of field and thermal magnetization reversal in nanostructured magnetic materials," Doctoral Dissertation to Universidad Autonoma de Madrid, 2007. http://www.fgarciasanchez.es/thesisfelipe/.

[85] http://www.jmol.org/. Jmol: an open-source Java viewer for chemical structures in 3D.

[86] N. Kazantseva, D. Hinzke, U. Nowak, R. W. Chantrell, U. Atxitia, and O. Chubykalo-Fesenko, "Towards multiscale modeling of magnetic materials: Simulations of FePt," Phys. Rev. B, vol. 77, p. 184428, 2008.

[87] T. Bublat and D. Goll, "Temperature dependence of the magnetic properties of L10-FePt nanostructures and films," Journal of Applied Physics, vol. 108, no. 11, p. 113910, 2010.

[88] J. Waters, A. Berger, D. Kramer, H. Fangohr, and O. Hovorka, "Identification of Curie temperature distributions in magnetic particulate systems," Journal of Physics D: Applied Physics, vol. 50, no. 35, p. 35LT01, 2017.

[89] R. Zhang and R. F. Willis, "Thickness-dependent curie temperatures of ultrathin magnetic films: Effect of the range of spin-spin interactions," Phys. Rev. Lett., vol. 86, pp. 2665–2668, 2001.

[90] M. E. Fisher and A. E. Ferdinand, "Interfacial, boundary, and size effects at critical points," Phys. Rev. Lett., vol. 19, pp. 169–172, 1967.

[91] J. M. Yeomans, Statistical Mechanics of Phase Transitions. Oxford University Press, 1992.

[92] O. Iglesias and A. Labarta, "Finite-size and surface effects in maghemite nanoparticles: Monte Carlo simulations," Phys. Rev. B, vol. 63, p. 184416, 2001.

[93] H. Kachkachi and D. Garanin, "Boundary and finite-size effects in small magnetic systems," Physica A: Statistical Mechanics and its Applications, vol. 300, no. 3, pp. 487–504, 2001.

[94] D. Weller, A. Moser, L. Folks, M. Best, W. Lee, M. Toney, M. Schwickert, J.-U. Thiele, and M. Doerner, "High Ku materials approach to 100 Gbits/in2," Magnetics, IEEE Transactions on, vol. 36, pp. 10 – 15, 2000.

[95] G. H. O. Daalderop, P. J. Kelly, and M. F. H. Schuurmans, "Magnetocrystalline anisotropy and orbital moments in transition-metal compounds," Phys. Rev. B, vol. 44, pp. 12054–12057, 1991.

[96] A. Sakuma, "First principle calculation of the magnetocrystalline anisotropy energy of FePt and CoPt ordered alloys," Journal of the Physical Society of Japan, vol. 63, no. 8, pp. 3053–3058, 1994.

[97] P. Oppeneer, "Magneto-optical spectroscopy in the valence-band energy regime: Relationship to the magnetocrystalline anisotropy," Journal of Magnetism and Magnetic Materials, vol. 188, pp. 275–285, 1998.

[98] P. Ravindran, A. Kjekshus, H. Fjellvåg, P. James, L. Nordström, B. Johansson, and O. Eriksson, "Large magnetocrystalline anisotropy in bilayer transition metal phases from first-principles full-potential calculations," Phys. Rev. B, vol. 63, p. 144409, 2001.

[99] A. B. Shick and O. N. Mryasov, "Coulomb correlations and magnetic anisotropy in ordered $L1_0$ CoPt and FePt alloys," Phys. Rev. B, vol. 67, p. 172407, 2003.

[100] I. V. Solovyev, P. H. Dederichs, and I. Mertig, "Origin of orbital magnetization and magnetocrystalline anisotropy in TX ordered alloys (where T=Fe,Co and X=Pd,Pt)," Phys. Rev. B, vol. 52, pp. 13419–13428, 1995.

[101] T. Shima, K. Takanashi, Y. K. Takahashi, and K. Hono, "Coercivity exceeding 100koe in epitaxially grown FePt sputtered films," Applied Physics Letters, vol. 85, no. 13, pp. 2571–2573, 2004.

[102] K. Inoue, H. Shima, A. Fujita, K. Ishida, K. Oikawa, and K. Fukamichi, "Temperature dependence of magnetocrystalline anisotropy constants in the single variant state of L10-type FePt bulk single crystal," Applied Physics Letters, vol. 88, no. 10, p. 102503, 2006.

[103] H. J. Richter, O. Hellwig, S. Florez, C. Brombacher, and M. Albrecht, "Anisotropy measurements of FePt thin films," Journal of Applied Physics, vol. 109, no. 7, p. 07B713, 2011.

[104] B. K. Chatterjee, C. K. Ghosh, and K. K. Chattopadhyay, "Temperature dependence of magnetization and anisotropy in uniaxial NiFe2O4 nanomagnets: Deviation from the Callen-Callen power law," Journal of Applied Physics, vol. 116, no. 15, p. 153904, 2014.

[105] D. Miura and A. Sakuma, "Power law analysis for temperature dependence of magnetocrystalline anisotropy constants of Nd2Fe14B magnets," AIP Advances, vol. 8, no. 7, p. 075114, 2018.

[106] H. Sepehri-Amin, H. Iwama, G. Hrkac, K. Butler, T. Shima, and K. Hono, "Pt surface segregation in L10-FePt nano-grains," Scripta Materialia, vol. 135, pp. 88–91, 2017.

[107] R. Moreno, S. Poyser, D. Meilak, A. Meo, S. Jenkins, V. Lazarov, G. Vallejo-Fernandez, S. Majetich, and R. Evans, "The role of faceting and elongation on the magnetic anisotropy of magnetite Fe3O4 nanocrystals," Scientific Reports, vol. 10, 2020.

[108] T. J. Klemmer, N. Shukla, C. Liu, X. W. Wu, E. B. Svedberg, O. Mryasov, R. W. Chantrell, D. Weller, M. Tanase, and D. E. Laughlin, "Structural studies of L10 FePt nanoparticles," Applied Physics Letters, vol. 81, no. 12, pp. 2220–2222, 2002.

[109] S. Aksornniem, R. Evans, R. Chantrell, and R. Silapunt, "Magnetic switching in BPM, TEAMR, and modified TEAMR by using dielectric underlayer media," IEEE Transactions on Magnetics, vol. 52, pp. 1–1, 2015.

[110] P. Schaaf, K. Zhang, C. Lange, A. Holz, M. Weisheit, and S. Faehler, "Structure and anisotropy of epitaxial fcc FePt films," Applied Surface Science, vol. 253, pp. 8107 – 8110, 2007.

[111] D. Hinzke, N. Kazantseva, U. Nowak, O. N. Mryasov, P. Asselin, and R. W. Chantrell, "Domain wall properties of FePt: From Bloch to linear walls," Phys. Rev. B, vol. 77, p. 094407, 2008.

[112] X. Wang, R. Wu, D.-s. Wang, and A. J. Freeman, "Torque method for the theoretical determination of magnetocrystalline anisotropy," Phys. Rev. B, vol. 54, pp. 61–64, 1996.

[113] R. Wu and A. Freeman, "Spin–orbit induced magnetic phenomena in bulk metals and their surfaces and interfaces," Journal of Magnetism and Magnetic Materials, vol. 200, no. 1, pp. 498–514, 1999.

[114] R. Skomski, O. N. Mryasov, J. Zhou, and D. J. Sellmyer, "Finite-temperature anisotropy of magnetic alloys," Journal of Applied Physics, vol. 99, no. 8, p. 08E916, 2006.

[115] R. Skomski, A. Kashyap, and J. Zhou, "Atomic and micromagnetic aspects of L10 magnetism," Scripta Materialia, vol. 53, no. 4, pp. 389–394, 2005. Viewpoint set no. 36 on: L10 phases for permanent magnet and recording applications.

[116] R. Skomski, A. Kashyap, and D. Sellmyer, "Finite-temperature anisotropy of PtCo magnets," Magnetics, IEEE Transactions on, vol. 39, pp. 2917 – 2919, 2003.

[117] J. B. Staunton, S. Ostanin, S. S. A. Razee, B. L. Gyorffy, L. Szunyogh, B. Ginatempo, and E. Bruno, "Temperature dependent magnetic anisotropy in metallic magnets from an ab initio electronic structure theory: $L1_0$-Ordered FePt," Phys. Rev. Lett., vol. 93, p. 257204, 2004.

[118] J.-U. Thiele, K. R. Coffey, M. F. Toney, J. A. Hedstrom, and A. J. Kellock, "Temperature dependent magnetic properties of highly chemically ordered Fe$(55-x)$Ni(x)Pt(45)$L1_0$ films," Journal of Applied Physics, vol. 91, no. 10, pp. 6595–6600, 2002.

[119] R. F. L. Evans, L. Rózsa, S. Jenkins, and U. Atxitia, "Temperature scaling of two-ion anisotropy in pure and mixed anisotropy systems," Phys. Rev. B, vol. 102, p. 020412, 2020.

[120] T. Saito, K. K. Tham, R. Kushibiki, T. Ogawa, and S. Saito, "Separate quantitative evaluation of degree of order and perpendicular magnetic anisotropy for disorder and order portion in FePt granular films," AIP Advances, vol. 11, no. 1, p. 015310, 2021.

[121] U. Atxitia, O. Chubykalo-Fesenko, N. Kazantseva, D. Hinzke, U. Nowak, and R. W. Chantrell, "Micromagnetic modeling of laser-induced magnetization dynamics using the Landau-Lifshitz-Bloch equation," Applied Physics Letters, vol. 91, no. 23, p. 232507, 2007.

[122] J. Hohlfeld, X. Zheng, and M. Benakli, "Measuring temperature and field profiles in heat assisted magnetic recording," Journal of Applied Physics, vol. 118, no. 6, p. 064501, 2015.

[123] A. Meo, W. Pantasri, W. Daeng-am, S. E. Rannala, S. I. Ruta, R. W. Chantrell, P. Chureemart, and J. Chureemart, "Magnetization dynamics of granular heat-assisted magnetic recording media by means of a multiscale model," Phys. Rev. B, vol. 102, p. 174419, 2020.

[124] A. Lyberatos, D. Weller, and G. J. Parker, "Switching time in laser pulse heat-assisted magnetic recording using L10-FePt nanoparticles," Journal of Applied Physics, vol. 117, no. 13, p. 133905, 2015.

[125] R. F. L. Evans and W. J. Fan, "Atomistic simulation of sub-nanosecond non-equilibrium field cooling processes for magnetic data storage applications," Applied Physics Letters, vol. 105, no. 19, p. 192405, 2014.

[126] C. Vogler, C. Abert, F. Bruckner, and D. Suess, "Landau-Lifshitz-Bloch equation for exchange-coupled grains," Phys. Rev. B, vol. 90, p. 214431, 2014.

[127] R.-V. Ababei, M. O. A. Ellis, R. F. L. Evans, and R. W. Chantrell, "Anomalous damping dependence of the switching time in Fe/FePt bilayer recording media," Phys. Rev. B, vol. 99, p. 024427, 2019.

[128] J. Becker, O. Mosendz, D. Weller, A. Kirilyuk, J. C. Maan, P. C. M. Christianen, T. Rasing, and A. Kimel, "Laser induced spin precession in highly anisotropic granular l10 fept," Applied Physics Letters, vol. 104, no. 15, p. 152412, 2014.

[129] W. Fan, "Atomistic modelling of magnetisation reversal processes in recording media," Doctoral Dissertation to the University of York, 2013. https://etheses.whiterose.ac.uk/5182/.

[130] P. Esquinazi, J. Barzola-Quiquia, D. Spemann, M. Rothermel, H. Ohldag, N. García, A. Setzer, and T. Butz, "Magnetic order in graphite: Experimental evidence, intrinsic and extrinsic difficulties," Journal of Magnetism and Magnetic Materials, vol. 322, no. 9, pp. 1156–1161, 2010. Proceedings of the Joint European Magnetic Symposia.

[131] O. Muthsam, C. Vogler, and D. Suess, "Noise reduction in heat-assisted magnetic recording of bit-patterned media by optimizing a high/low Tc bilayer structure," Journal of Applied Physics, vol. 122, no. 21, p. 213903, 2017.

[132] D. Suess and T. Schrefl, "Breaking the thermally induced write error in heat assisted recording by using low and high Tc materials," Applied Physics Letters, vol. 102, no. 16, p. 162405, 2013.

[133] O. Hellwig, J. B. Kortright, K. Takano, and E. E. Fullerton, "Switching behavior of Fe-Pt/Ni-Fe exchange-spring films studied by resonant soft-x-ray magneto-optical Kerr effect," Phys. Rev. B, vol. 62, pp. 11694–11698, 2000.

[134] T. Dutta, S. N. Piramanayagam, M. S. M. Saifullah, and C. S. Bhatia, "High switching efficiency in fept exchange coupled composite media mediated by MgO exchange control layers," Applied Physics Letters, vol. 111, no. 4, p. 042405, 2017.